Dissertation
submitted to the
Combined Faculties for the Natural Sciences and for Mathematics
of the Ruperto-Carola University of Heidelberg, Germany
for the degree of
Doctor of Natural Sciences

Put forward by
Dipl.-Phys. Hanna Schempp
Born in Bonn, Germany
Oral examination: July 23rd, 2014

Formation of Aggregates and Energy Transport in Ultracold Rydberg Interacting Gases

Referees: **Prof. Dr. Matthias Weidemüller**
Prof. Dr. Selim Jochim

Zusammenfassung:
Diese Arbeit untersucht verschiedene Aspekte stark wechselwirkender ultrakalter Rydberggase, die durch Licht gekoppelt sind, darunter die Anregung von korrelierten Strukturen, sogenannten Rydbergaggregaten, sowie dipolaren Energietransport. Hierfür wurde eine experimentelle Apparatur konstruiert. Coherent population trapping (CPT) und elektromagnetisch induzierte Transparenz (EIT) mit Rydbergzuständen werden untersucht. Um die Entstehung von Rydbergaggregaten zu untersuchen wird die Methode der vollständigen Zählstatistik (FCS) angewendet, die es ermöglicht die Größe der Rydbergaggregate zu bestimmen. Dephasierung während der Anregung hat dramatische Konsequenzen für den Anregungsprozess und führt zu sequentieller Anregung um einen anfänglichen Keim herum. EIT mit Rydbergzuständen wird verwendet um ein neues optisches Abbildungsverfahren von Rydbergatomen zu realisieren, das eine ausgezeichnete Sensitivität mit hoher räumlicher und zeitlicher Auflösung kombiniert. Mit diesem Schema werden dipolare Transportprozesse in Rydbergsystemen untersucht. Klassischer Transport wird untersucht unter dem Einfluss von Dekohärenz, die durch die Messung selbst verursacht wird. Die starken Wechselwirkungen beeinflussen den Transport und führen zu einem charakteristischen "hopping"-Abstand deutlich über nächste Nachbarn hinaus. Erste Anzeichen für kohärenten Transport in unserem System werden gezeigt. Diese Experimente beleuchten die Rolle von Korrelationen in der Anregung und Entwicklung von stark wechselwirkenden Quantensystemen und können möglicherweise dazu dienen Energietransport in biologischen Systemen zu modellieren.

Abstract:
This thesis investigates different aspects of strongly interacting ultracold Rydberg gases coupled by light, including the excitation of correlated structures called Rydberg aggregates and dipolar energy transport. For this purpose an experimental apparatus has been constructed. We study coherent population trapping (CPT) and electromagnetically induced transparency (EIT) involving Rydberg states. To study the formation of Rydberg aggregates we use full counting statistics (FCS) which makes it possible to infer the size of Rydberg aggregates. Dephasing during the excitation is found to have a dramatic effect on the formation process, leading to sequential growth around an initial grain. Rydberg state EIT is used to realize a new direct optical imaging scheme for Rydberg atoms which combines highly sensitive detection with high spatial and temporal resolution. Applying this technique we observe dipole-mediated energy transport processes between Rydberg atoms. We study classical transport in the presence of strong measurement induced decoherence. The strong interactions are seen to mediate long-range hopping significantly beyond nearest neighbors. We present first indications for coherent transport in this system. These experiments shed light on the role of correlations in the excitation and evolution of strongly interacting quantum systems and e.g. could possibly be used to model energy transport in biological systems.

This thesis is based on the following manuscripts and publications:

- **Quantum and classical spin transport in Rydberg dressed atomic gases**
  H. Schempp, G. Günter, S. Wüster, M. Weidemüller, S. Whitlock
  in preparation

- **Full counting statistics of laser excited Rydberg aggregates in a one-dimensional geometry**
  H. Schempp, G. Günter, M. Robert-de-Saint-Vincent, C. S. Hofmann, D. Breyel, A. Komnik, D. Schönleber, M. Gärttner, J. Evers, S. Whitlock, M. Weidemüller
  Physical Review Letters **112**, 013002 (2014)

- **Observing the dynamics of dipole-mediated energy transport by interaction enhanced imaging**
  G. Günter, H. Schempp, M. Robert-de-Saint-Vincent, V. Gavryusev, S. Helmrich, C. S. Hofmann, S. Whitlock, M. Weidemüller
  Science **342** 953-956 (2013)

- **An experimental approach for investigating many-body phenomena in Rydberg-interacting quantum systems**
  C. S. Hofmann, G. Günter, H. Schempp, N. L. M. Müller, A. Faber, H. Busche, M. Robert-de-Saint-Vincent, S. Whitlock, M. Weidemüller
  Frontiers of Physics (2013)

- **Sub-Poissonian statistics of Rydberg-interacting dark-state polaritons**
  C. S. Hofmann, G. Günter, H. Schempp, M. Robert-de-Saint-Vincent, M. Gärttner, J. Evers, S. Whitlock, M. Weidemüller
  Physical Review Letters **110**, 203601 (2013)

- **Interaction enhanced imaging of individual Rydberg atoms in dense gases**
  G. Günter, M. Robert-de-Saint-Vincent, H. Schempp, C. S. Hofmann, S. Whitlock, M. Weidemüller
  Physical Review Letters **108**, 013002 (2012)

- **Coherent population trapping with controlled interparticle interactions**
  H. Schempp, G. Günter, C. S. Hofmann, C. Giese, S. D. Saliba, B. D. DePaola, T. Amthor, M. Weidemüller, S. Sevinçli, T. Pohl
  Physical Review Letters **104**, 173602 (2010)

The author furthermore contributed to the following publications:

- **Spontaneous avalanche ionization of a strongly blockaded Rydberg gas**
  M. Robert-de-Saint-Vincent, C. S. Hofmann, H. Schempp, G. Günter, S. Whitlock, M. Weidemüller
  Physical Review Letters **110**, 045004 (2013)

- **Quantum interference in interacting three-level Rydberg gases: coherent population trapping and electromagnetically induced transparency**
  S. Sevinçli, C. Ates, T. Pohl, H. Schempp, C. S. Hofmann, G. Günter, T. Amthor, M. Weidemüller, J. D. Pritchard, D. Maxwell, A. Gauguet, K. J. Weatherill, M. P. A. Jones, C. S. Adams
  Journal of Physics B **44**, 184018 (2011)

- **Combined ion and optical detection of Rydberg atoms in dense ultracold atomic gases**
  C. S. Hofmann, G. Günter, H. Schempp, M. Robert-de-Saint-Vincent, S. Whitlock, M. Weidemüller
  in preparation

Contents

Chapter 1

Introduction

Understanding how correlations between particles emerge in a many-body system and how they influence the properties of real materials and natural processes is a driving force in modern physics. Prominent examples include the transition from water to ice, or the way current flows through a wire, both of which strongly depend on how the constituent particles interact with one another. In this thesis I explore the question of how correlations arise when an ultracold atomic gas is excited to strongly-interacting states (Rydberg states) and what role these interactions have on its subsequent dynamical evolution.

In the last years the field of ultracold Rydberg gases has experienced explosive growth, impacting diverse areas of research, e.g. quantum information science (see [Saffman *et al.*, 2010] and references therein), few-body physics and the study of exotic molecules [Greene *et al.*, 2000; Bendkowsky *et al.*, 2009; Boisseau *et al.*, 2002; Overstreet *et al.*, 2009; Gaj *et al.*, 2014], many-body physics [Löw *et al.*, 2012; Hofmann *et al.*, 2013a; Viteau *et al.*, 2012], quantum optics [Pritchard *et al.*, 2012b; Peyronel *et al.*, 2012; Firstenberg *et al.*, 2013; Dudin and Kuzmich, 2012; Maxwell *et al.*, 2013], transport [Günter *et al.*, 2013] and ultracold plasmas [Killian, 2007], all of which exploit the strong interactions between Rydberg atoms.

The most prominent effect of the Rydberg interactions is the so-called dipole blockade of excitation [Comparat and Pillet, 2010]. This effect arises from the competition between laser excitation and the strong interactions which leads to many-body correlations and to the emergence of a new length scale in the system (the blockade radius), within which the excitation of more than one Rydberg atom is strongly suppressed. The Rydberg blockade was first proposed in the context of quantum information processing [Jaksch *et al.*, 2000; Lukin *et al.*, 2001], and its effects have been observed in various experiments [Tong *et al.*, 2004; Singer *et al.*,

2004; Vogt *et al.*, 2006; Urban *et al.*, 2009; Gaëtan *et al.*, 2009]. In contrast to the relatively simple correlations induced by the Rydberg blockade, the ground state of a many-body system comprised of repulsively interacting particles is usually a crystalline state and thus exhibits true long-range order. Theoretical work has explored the phase diagram of the laser driven Rydberg system [Weimer *et al.*, 2008] as well as the possible approach to prepare the crystalline ground state [Pohl *et al.*, 2010]. Signs of crystalline correlation functions have been seen experimentally [Schwarzkopf *et al.*, 2011; Schauß *et al.*, 2012]. However, the deterministic preparation of a Rydberg crystal requires chirped excitation pulses to adiabatically follow the ground state of the many-body system [Pohl *et al.*, 2010] which has only recently been experimentally demonstrated [Schauß *et al.*, 2014]. In between the regimes of a Rydberg blockaded gas and the crystalline state, one expects the formation of correlated structures comprised a few Rydberg excitations, which do not feature true long-range order, but exhibit correlations which can extend beyond pairs of atoms. The processes behind the formation of these Rydberg aggregates [Gärttner *et al.*, 2013; Schwarzkopf *et al.*, 2013], and in particular the effects of decoherence, have recently been investigated both theoretically and experimentally [Lee *et al.*, 2011; Lee *et al.*, 2012; Petrosyan *et al.*, 2013; Höning *et al.*, 2013; Malossi *et al.*, 2013; Schönleber *et al.*, 2014; Lesanovsky and Garrahan, 2014], including our own studies [Schempp *et al.*, 2014].

Correlations also play an important role in the interaction-mediated hopping of Rydberg excitations through an atomic gas after initial excitation. This is closely related to e.g. energy transport processes in biological systems such as photosynthetic light-harvesting complexes [Mülken *et al.*, 2007] where the same basic mechanism called Förster resonance energy transfer (FRET) plays a crucial role. On the one hand the disorder due to random hopping sites can lead to a slow down of the transport dynamics [Robicheaux and Gill, 2014]. On the other hand, as we show in this thesis, the Rydberg blockade can introduce dephasing and a new length scale to the hopping resulting in rapid diffusive transport. First evidence for dipolar exchange interactions was observed in some of the first experiments on ultracold Rydberg atoms [Anderson *et al.*, 1998; Mourachko *et al.*, 1998], and the dynamics have been investigated in [Westermann *et al.*, 2006; van Ditzhuijzen *et al.*, 2008]. However, to study energy transport dynamics in detail requires a high-resolution and state-selective imaging technique for Rydberg excitations. Imaging Rydberg atoms is a non-trivial task, and only in the last years a few different approaches have been realized, which are either based on ionization [Schwarzkopf *et al.*, 2011; Lochead *et al.*, 2013], on fluorescence imaging of atoms after depumping to the ground state

[Schauß *et al.*, 2012], or on direct fluorescence imaging using the second valence electron of earth alkali atoms [McQuillen *et al.*, 2013]. We have developed our own approach based on electromagnetically induced transparency (EIT) which is ideally suited for the study of Rydberg dynamics.

Electromagnetically induced transparency (EIT) where one of the long-lived atomic states is a Rydberg state gives rise to many surprising effects. EIT provides the possibility to map Rydberg state properties onto a strong optical transition [Mohapatra *et al.*, 2007; Tauschinsky *et al.*, 2010], and in particular Rydberg-Rydberg interactions can give rise to extreme optical non-linearities [Pritchard *et al.*, 2010; Sevinçli *et al.*, 2011a; Gorshkov *et al.*, 2011; Gorshkov *et al.*, 2013]. This can allow for the realization of effective photon-photon interactions and non-classical light fields [Dudin and Kuzmich, 2012; Peyronel *et al.*, 2012; Pritchard *et al.*, 2012a; Firstenberg *et al.*, 2013; Maxwell *et al.*, 2013; Otterbach *et al.*, 2013], as well as possible technological developments such as single-photon transistors or all-optical quantum gates [Paredes-Barato and Adams, 2014; Baur *et al.*, 2014; Gorniaczyk *et al.*, 2014; Tiarks *et al.*, 2014]. In addition Rydberg state EIT can also be used as a sensor, e.g. to measure the electric field distribution in an atom chip [Tauschinsky *et al.*, 2010] or to precisely characterize the Rabi frequency distribution of the Rydberg excitation laser in a spatially resolved manner [Hofmann *et al.*, 2014].

An even more interesting application, however, is our new scheme to optically and minimally destructively image the distribution of Rydberg atoms within a gas, which was developed during this thesis [Günter *et al.*, 2012; Olmos *et al.*, 2011]. With this imaging scheme at hand we could study Rydberg energy transport in detail for the first time. Interestingly, the diffusive nature of the observed energy transport and its rate are intimately linked to the imaging process itself.

This thesis is structured as follows: Ch. 2 starts with a short review of Rydberg atoms and their interactions, followed by a description of the experimental apparatus constructed during this thesis. Ch. 3 focuses on the excitation of Rydberg atoms using coherent laser fields. The basic mechanisms of electromagnetically induced transparency (EIT) will be introduced, followed by a general discussion of EIT in the presence of interparticle interactions (Ch. 3.2). I will discuss the concept of dark-state polaritons as a framework to understand the interaction effects in these systems and I will discuss our own early work on coherent population trapping (CPT) and EIT in interacting Rydberg gases. In particular we investigate the influence of Rydberg-Rydberg interactions on the absorption of a gas under EIT conditions and on the statistical fluctuations of the number of Rydberg excitations. In Ch. 4 we extend this to the analysis of full counting statistics applied to the study

of Rydberg aggregates, i.e. correlated systems comprised of a few Rydberg excitations. The counting statistics provides a way to reveal the nature of the underlying few-body correlations. In addition we study in how far the aggregate formation is influenced by decoherence. Our EIT based imaging scheme for Rydberg atoms is introduced and experimentally demonstrated in Ch. 5. We use this imaging scheme to study dipolar energy transport (Ch. 6) and investigate the effect of decoherence on the transport process. We show first evidence for the case of purely coherent evolution which strongly contrasts with the decoherence dominated transport studied previously. In Ch. 7 we discuss microwave driven Rydberg systems featuring dipolar population exchange between S and P states. These last experiments provide a way to independently measure the dipolar interaction strength and constitute the basis for future transport experiments, including the crossover from quantum to classical transport.

Chapter 2

Ultracold Rydberg gases: properties and experimental approach

This chapter is partially based on the following publication:

An experimental approach for investigating many-body phenomena in Rydberg-interacting quantum systems
C. S. Hofmann, G. Günter, H. Schempp, N. L. M. Müller, A. Faber, H. Busche, M. Robert-de-Saint-Vincent, S. Whitlock, M. Weidemüller
Frontiers of Physics (2013)

Rydberg atoms with their extreme properties [Gallagher, 1994] and strong interactions are an ideal playground to study interesting aspects of few- and many-body physics [Comparat and Pillet, 2010; Löw *et al.*, 2012; Hofmann *et al.*, 2013a], including phase transitions [Weimer *et al.*, 2008], energy transport [Mülken *et al.*, 2007] as well as quantum gates [Wilk *et al.*, 2010; Isenhower *et al.*, 2010], and new quantum optical schemes [Pritchard *et al.*, 2012b]. To explore these phenomena experimentally particular care in the experimental approach is required to account for the special properties of Rydberg atoms as e.g. their sensitivity to electric fields. In this Chapter we will first review some important properties of Rydberg atoms and in particular the different types of interactions which are at the heart of the so-called excitation blockade (Ch. 2.1). The experimental apparatus constructed during this thesis is introduced in Ch. 2.3 with particular emphasis on the aspects which are crucial for Rydberg atom experiments.

2.1 Rydberg atoms and their interactions

2.1.1 Alkali Rydberg atoms

Rydberg atoms are atoms with an electron excited to a high-lying atomic state with large principal quantum number n. As a consequence of the large spatial extent and the weak binding energy of the electron, Rydberg atoms feature extreme properties as compared to ground state atoms. In the case of alkali atoms the electron experiences a potential resulting from N positive charges in the nucleus, which are shielded by $N-1$ core electrons. The Nth electron, which is excited to a Rydberg state and thus on average situated far away from the core, therefore experiences a potential which can be well approximated by a single positive charge. For this reason the wave functions of alkali Rydberg atoms resemble those of the hydrogen atom. The deviations of the real core potential from that of a single positive charge result mainly in a phase shift of the wave functions, which goes along with a correction of the energy eigenvalues as compared to those of the hydrogen atom. This correction can be quantified using the so-called quantum defect δ^{nl}, which depends on n as well as the quantum number of the angular momentum, l, and translates the principal quantum number n into an effective principal quantum number $n^* = n - \delta^{nl}$, for which the hydrogenic scalings hold. Table 2.1 shows the scaling of some important Rydberg atom properties with the effective principal quantum number n^*.

energy	n^{*-2}
orbital radius	n^{*2}
lifetime	n^{*3}
level spacing	n^{*-3}
ionization field	n^{*-4}
polarizability	n^{*7}
dipole matrix element	n^{*2}
resonant dipolar interaction strength	n^{*4}
vdW interaction strength	n^{*11}

Table 2.1: Selected properties of Rydberg atoms and their scalings with the effective principal quantum number n^* (see e.g. [Gallagher, 1994]).

The quantum defect for nS, nP and nD states of Rubidium has been measured using microwave spectroscopy [Li *et al.*, 2003]. It can be expressed as $\delta^{nl} = \delta_0 +$

$\delta_2/(n-\delta_0)^2$ with $\delta_0 = 3.1311804$ and $\delta_2 = 0.1784$ for Rydberg S states ($l = 0$). The correction is most significant for low angular momentum states since in this case the electron has a larger probability of being close to the nucleus and thus experiences imperfect shielding of the nuclear charges.

Another important property of Rydberg atoms is their huge polarizability. Due to the weak binding energy of the electron the charge distribution of the Rydberg atom can be deformed already by weak electric fields, thereby inducing an electric dipole moment to the Rydberg atom. These huge polarizabilities, which scale as n^{*7}, require excellent experimental control of electric stray fields. On the other hand the loose binding allows to ionize Rydberg atoms by moderate electric fields thus making field ionization and subsequent ion detection a valuable tool.

2.1.2 Rydberg interactions

Dipolar interactions

Since neutral atoms do not have a net charge, the most important contribution in the multi-pole expansion are electrical dipole interactions. Rydberg atoms with their huge dipole moments therefore feature interactions which are many orders of magnitude stronger than those between ground state atoms. The classical interaction energy of two dipoles separated by a distance $\vec{R}$ is given by

$$E_{dip} = \frac{\vec{\mu_1} \cdot \vec{\mu_2}}{|\vec{R}|^3} - 3\frac{(\vec{\mu_1} \cdot \vec{R})(\vec{\mu_2} \cdot \vec{R})}{|\vec{R}|^5} \tag{2.1}$$

In a quantum mechanical description and neglecting the spatial orientation of the dipoles this translates to

$$V_{dd} \propto \frac{1}{R^3} \sum_{|\Phi_1'\rangle, |\Phi_2'\rangle} \langle \Phi_1 | \hat{\mu}_1 | \Phi_1' \rangle \langle \Phi_2 | \hat{\mu}_2 | \Phi_2' \rangle = \frac{1}{R^3} \sum_{|\Phi_1' \Phi_2'\rangle} \langle \Phi_1 \Phi_2 | \hat{\mu}_1 \hat{\mu}_2 | \Phi_1' \Phi_2' \rangle \tag{2.2}$$

for the interaction energy between two Rydberg atoms in the states Φ_1 and Φ_2, which are coupled to an infinite number of states Φ_1' and Φ_2' via the dipole operators $\hat{\mu}_1$ and $\hat{\mu}_2$ (see e.g. [Amthor *et al.*, 2009]). The infinite sum over all possible pair states in eq. 2.2 can usually be reduced to a few pair states with the strongest contribution. In the simplest case where only one pair state $|\Phi_1' \Phi_2'\rangle$ contributes significantly to the interaction energy the Hamiltonian in the basis $|\Phi_1 \Phi_2\rangle$, $|\Phi_1' \Phi_2'\rangle$ is given by

$$H = \begin{pmatrix} 0 & \frac{\mu_1 \mu_2}{R^3} \\ \frac{\mu_1 \mu_2}{R^3} & \Delta \end{pmatrix} . \tag{2.3}$$

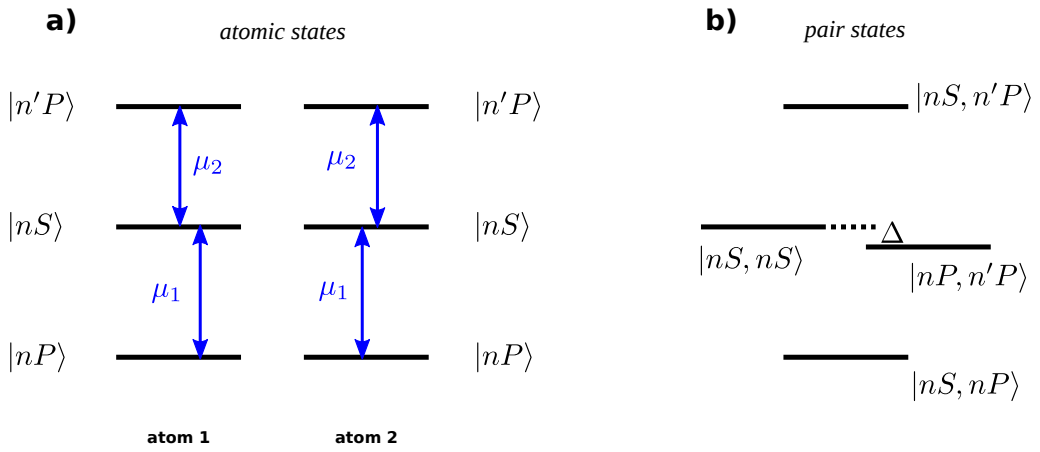

Figure 2.1: Illustration of the interaction between two atoms in state $|nS\rangle$. a) shows the relevant part of the atomic structure with the states $|nS\rangle$, $|nP\rangle$ and $|n'P\rangle$. b) shows the pair state energies. The pair states $|nS, nS\rangle$ and $|nP, n'P\rangle$ experience an energy shift depending on the Förster defect Δ as given in eq. 2.4 due to their coupling.

where the Förster defect Δ quantifies the energy difference between the two pair states. Solving for the eigenvalues of this matrix yields

$$E_{\pm} = \frac{\Delta}{2} \pm \sqrt{\left(\frac{\Delta}{2}\right)^2 + \left(\frac{\mu_1 \mu_2}{R^3}\right)^2}. \tag{2.4}$$

This situation is illustrated in fig. 2.1 for the interaction between two atoms both in the Rydberg state nS, i.e. $|\Phi_1\rangle = |\Phi_2\rangle = |nS\rangle$. $|nS\rangle$ is coupled to the states $|\Phi_1'\rangle = |nP\rangle$ and $|\Phi_2'\rangle = |n'P\rangle$ via the dipole operators $\hat{\mu}_1$ and $\hat{\mu}_2$. Fig. 2.1 b shows the same situation in a pair state picture. Depending on the Förster defect Δ the pair states $|nS, nS\rangle$ and $|nP, n'P\rangle$ experience an energy shift as given in eq. 2.4.

Depending on the energy of the pair states $|\Phi_1, \Phi_2\rangle$ and $|\Phi_1', \Phi_2'\rangle$ the Förster defect can be either positive or negative, thereby determining the sign of the interaction. In particular, it can be tuned via an electric field since the involved states have slightly different polarizabilities and therefore experience different energy shifts in an electric field. As can be seen from eq. 2.4 the Förster defect not only determines the sign of the interaction but also its character. E.g., in the case where $\Delta \gg \frac{\mu_1 \mu_2}{R^3}$, a Taylor expansion of eq. 2.4 yields an energy shift of

$$\Delta E = \frac{C_6}{R^6}, \tag{2.5}$$

i.e. a van der Waals type R^{-6} scaling with the strength of the interaction potential being $C_6 = (\mu_1 \mu_2)^2 / \Delta$. Considering the scalings with the principal quantum number of $\mu_{1,2} \sim n^{*2}$ and $\Delta \sim n^{*-3}$ one finds $C_6 \sim n^{*11}$ as listed in tab. 2.1.

As mentioned above the sign of the Förster defect and thus the sign of the interactions can be positive or negative. We will mostly present experiments performed with repulsively interacting S state atoms. The reason for this is their better stability against ionizing collisions as compared to attractively interacting states [Amthor *et al.*, 2007b; Amthor *et al.*, 2007a].

In contrast, for vanishing Förster defect Δ, in the vicinity of a so-called Förster resonance, the energy shift given in eq. 2.4 reduces to

$$\Delta E = \frac{C_3}{R^3}. \tag{2.6}$$

with $C_3 = \mu_1\mu_2$. This hold in particular for the interaction between two states which feature a strong direct coupling, as e.g. $|nS, n'P\rangle$, where the exchange symmetric state $|n'P, nS\rangle$ is the most dominant pair state. In this case the Förster defect vanishes independent of the electric field and the interaction energy is

$$E_{\pm} = \pm\frac{\mu^2}{R^3} \tag{2.7}$$

with $\mu = \langle nS|\hat{\mu}|n'P\rangle = \langle n'P|\hat{\mu}|nS\rangle$ being the relevant dipole matrix element and $C_3 = \mu^2 \sim n^{*4}$ the strength of the resonant dipole interaction.

Dipole blockade of excitation

The most prominent consequence of the interactions discussed above is the dipole blockade of excitation from a ground state to a Rydberg state [Jaksch *et al.*, 2000; Lukin *et al.*, 2001; Tong *et al.*, 2004; Singer *et al.*, 2004; Comparat and Pillet, 2010]. It can be understood from a pair state picture as depicted in fig. 2.2, where a laser field resonant with the excitation frequency of a single Rydberg atom cannot excite a second Rydberg atom in the vicinity of the first due to the energy shift of the doubly excited state. As a consequence the strength of the interaction $V(R)$ together with the excitation bandwidth $\mathcal{W}$, which depends on the Rabi frequency and the dephasing associated with the laser excitation, determines a characteristic length scale. The so-called blockade radius reads

$$R_{bl} = \left(\frac{C_6}{\mathcal{W}}\right)^{1/6} \tag{2.8}$$

in the case of van der Waals interactions and

$$R_{bl} = \left(\frac{C_3}{\mathcal{W}}\right)^{1/3} \tag{2.9}$$

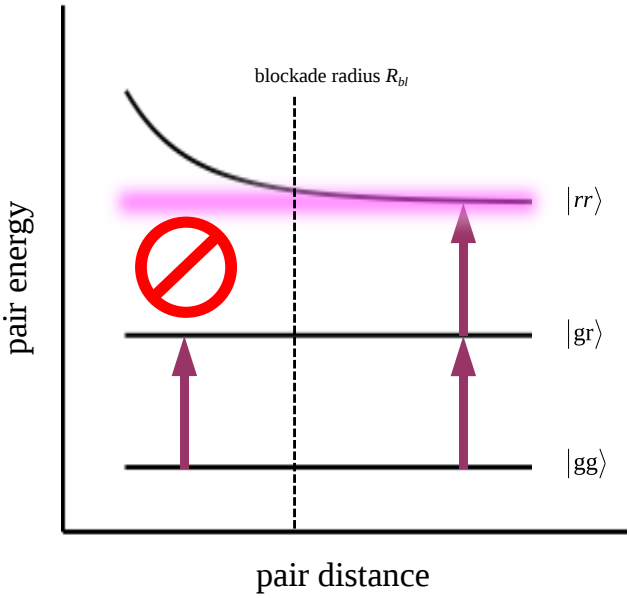

Figure 2.2: Dipole blockade of excitation. The energy of a pair of atoms is plotted vs. their distance for the pair states $|gg\rangle$ (both atoms in the ground state), $|rg\rangle$ (one atom in the ground state, one in the Rydberg state) and $|rr\rangle$ (both atoms in the Rydberg state). In the latter case the (in this example repulsive) interaction bends the potential at short distances. A laser resonant with the excitation frequency of an isolated Rydberg atom (indicated as the violet arrow) can excite two well-separated atoms to the Rydberg state. For short pair distances, however, the laser frequency does not match the energy required for the excitation of a second Rydberg atom due to the interaction induced level-shift. The blockade radius R_{bl} is defined as the pair distance at which the interaction energy matches the bandwidth $\mathcal{W}$ associated with the excitation (indicated by the pink bar). For van der Waals type interaction, e.g., $R_{bl} = (C_6/\mathcal{W})^{1/6}$.

for resonant dipole interactions. R_{bl} defines the pair distance within which the excitation of both atoms to the Rydberg state is strongly suppressed due to the large energy shift.

Extending this picture to a gas of many atoms, the system can be thought of as made up of a collection of blockade spheres, each with at most one Rydberg atom within a certain radius. However, the presence of many ground state atoms within one blockade radius leads to a collective enhancement of the Rabi frequency by a factor $\sqrt{N}$ where N is the number of atoms within one blockade radius. Since the Rabi frequency can influence the excitation bandwidth, both N and the Rabi frequency have to be determined self-consistently [Löw *et al.*, 2012].

Dipolar energy exchange

In the case of resonant dipole interaction the coupling not only leads to a shift of the pair energy but also to an energy exchange between the two atoms resulting in an oscillation of excitations. There are different state constellations featuring exchange interactions, which are sketched in fig. 2.3 and can all be thought of as excitons.

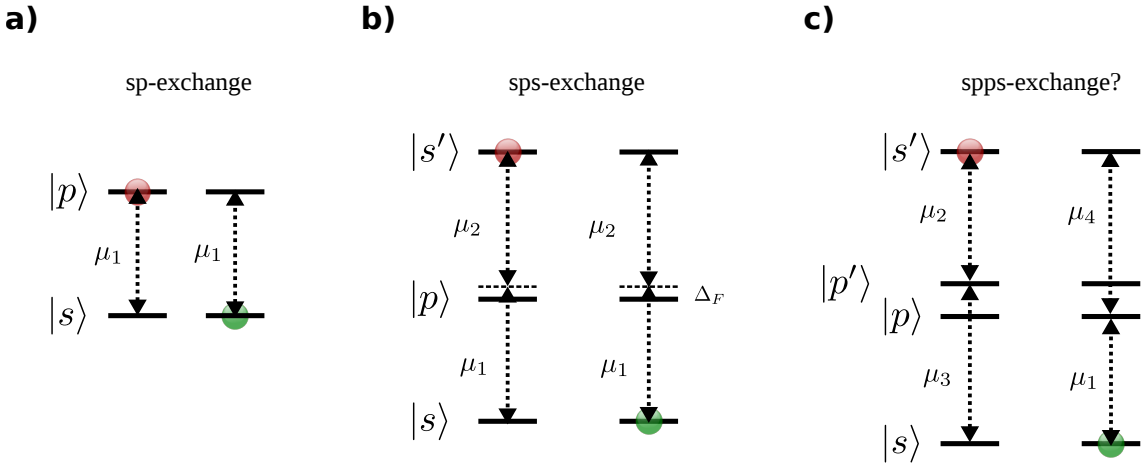

Figure 2.3: Different exchange mechanism between Rydberg states: a) shows the direct process involving the Rydberg states $|s\rangle$ and $|p\rangle$ which are coupled by μ_1. This process is independent of the electric field and thus always resonant. In contrast, b) shows an exchange between two Rydberg S states, $|s\rangle$ and $|s\rangle$, via one intermediate state $|p\rangle$, where the Förster defect Δ_F can be tuned to 0 by means of an electric field. The scheme sketched in c) involves two intermediate states $|p\rangle$ and $|p'\rangle$. Typically this scheme does not feature exchange between $|s\rangle$ and $|s'\rangle$ since the couplings μ_3 and μ_4 are almost never comparable to μ_1 and μ_2.

The simplest mechanism is

$$|s,p\rangle \leftrightarrow |p,s\rangle \tag{2.10}$$

which we refer to as *sp*-exchange and where $|s\rangle$ and $|p\rangle$ are Rydberg states featuring a direct dipolar coupling. This so-called Förster process is known in many other research areas such as semi-conductor physics [Williams, 2007] and biology [Clegg, 2009], and it was also one of the first interaction effects to be observed in ultracold Rydberg atom experiments [Anderson *et al.*, 1998; Mourachko *et al.*, 1998; Anderson *et al.*, 2002]. The process $|s,p\rangle \leftrightarrow |p,s\rangle$ is the simplest exchange process, since it involves only two states.

In contrast, fig. 2.3 b) shows an exchange between two Rydberg states, $|s\rangle$ and $|s'\rangle$, via one intermediate state $|p\rangle$. The Förster defect Δ_F (the energy difference

between the pair states $|s, s'\rangle$ and $|p, p\rangle$) can be tuned to 0 by means of an electric field. Since both $|s\rangle$ and $|s'\rangle$ couple strongly to $|p\rangle$ with the dipole moments μ_1 and μ_2, the second order exchange process

$$|s, s'\rangle \leftrightarrow |p, p\rangle \leftrightarrow |s', s\rangle \tag{2.11}$$

can occur, which we refer to as an *sps*-exchange.

The scheme sketched in fig. 2.3 c) involves two different intermediate states $|p\rangle$ and $|p'\rangle$. Like the two processes discussed before this arrangement results in an energy shift of the pair state $|s, s'\rangle$ which is given by eq. 2.4. However, an exchange process between the two S states requires the strength of the couplings μ_3 and μ_4 to be of the same order as the couplings μ_1 and μ_2, which is almost never the case. Therefore, the exchange process $|s, s'\rangle \leftrightarrow |p, p'\rangle \leftrightarrow |s', s\rangle$ is strongly suppressed when the Förster resonance involves two intermediate P states. However, the process

$$|s, s'\rangle \leftrightarrow |p, p'\rangle \tag{2.12}$$

can occur. Since it creates two P excitations and can then be followed by the two direct *sp*-exchange processes

$$|s, p\rangle \leftrightarrow |p, s\rangle \quad \text{and} \quad |s', p'\rangle \leftrightarrow |p', s'\rangle \tag{2.13}$$

we call this process (eq 2.12) "fission".

Fig. 2.4 shows the occurrence of Förster resonances between two Rydberg S states of principal quantum numbers n_1 and n_2 for electric fields below 4 V/cm. The different marker styles indicate the P states involved in the resonance. In this thesis we will use resonances with a difference in principal quantum number $\Delta n = 1$ ($|37S, 38S\rangle \leftrightarrow |37P, 37P\rangle$) and $\Delta n = 2$ ($|48S, 50S\rangle \leftrightarrow |48P, 49P\rangle$), but also $\Delta n = 13$ ($|37S, 50S\rangle \leftrightarrow |36P, 51P\rangle$). These are indicated in the figure with red circles.

2.2 Decoherence in Rydberg systems

In this section we will discuss different sources of decoherence in Rydberg systems. Decoherence is an irreversible change of the population or the phase of a quantum state. Decoherence can be introduced accidentally or on purpose, e.g. in the process of a measurement. In some cases, decoherence can even serve as a tool for engineering interesting quantum states as proposed in [Diehl *et al.*, 2008]. In Rydberg systems decoherence can e.g. be exploited for engineering a deterministic single photon absorber [Honer *et al.*, 2011] or single photon source [Dudin and Kuzmich, 2012]. It

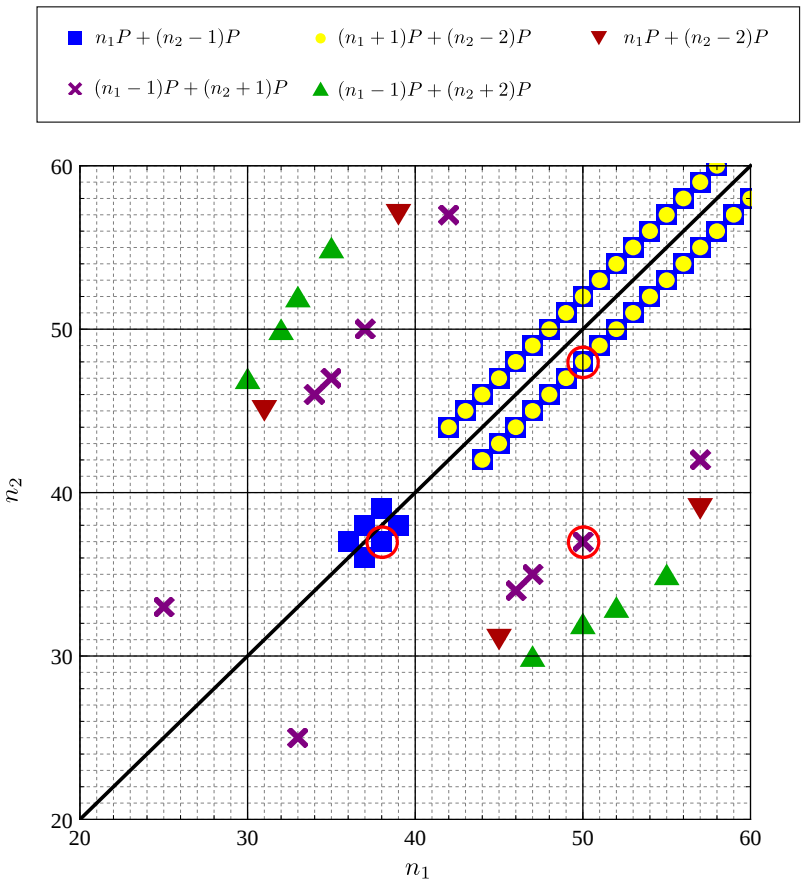

Figure 2.4: Occurrences of Förster resonances between Rydberg S states of principal quantum numbers n_1 and n_2 at fields below 4 V/cm. The markers indicate the different state combinations for the resonances, at the top the relevant P-pair states are indicated. During this thesis we have mainly used resonances with a difference in principal quantum number $\Delta n = 1$ (e.g. $|37S, 38S\rangle \leftrightarrow |37P, 37P\rangle$) and $\Delta n = 2$ (e.g. $|48S, 50S\rangle \leftrightarrow |48P, 49P\rangle$), but also $\Delta n = 13$ ($|37S, 50S\rangle \leftrightarrow |36P, 51P\rangle$). These resonances are indicated with red circles.

also strongly affects the formation of correlated structures [Lee *et al.*, 2011; Lee *et al.*, 2012; Petrosyan *et al.*, 2013; Höning *et al.*, 2013; Schempp *et al.*, 2014; Schönleber *et al.*, 2014; Lesanovsky and Garrahan, 2014] as will be discussed in the context of our experiments in Ch. 4, as well as the energy transport dynamics which we present in Ch. 6. In the context of quantum simulation it can become necessary to introduce and control different types of decoherence in order to model key processes of certain systems, as will be used to our advantage in Ch. 6.

In Rydberg systems we find various processes which result in decoherence with different implications for the system:

Ionization processes: these can e.g. be due to mechanical forces ([Amthor *et al.*, 2007b; Amthor *et al.*, 2007a]), due to blackbody radiation, or due to field ionization, and result in a total decay of the Rydberg population. Eventually the whole sample can evolve into an ultracold plasma as we have studied in [Robert-de-Saint-Vincent *et al.*, 2013]. Spontaneous ionization can be minimized by using repulsively interacting Rydberg states [Amthor *et al.*, 2007b; Amthor *et al.*, 2007a].

Population redistribution among Rydberg states due to blackbody radiation [Gallagher, 1994] and radiative decay of Rydberg states: the respective rates depend on the principal quantum number of the involved Rydberg states. Rydberg states have long lifetimes as compared to ground state atoms, typically on the order of $\approx 10 - 100\mu$s [Beterov *et al.*, 2009]. In most experiments presented here these processes do not play a major role.

Radiative decay of other states involved in the excitation process: we typically exploit a two-photon scheme for Rydberg excitation, involving an intermediate state. The rapid decay of this intermediate state does not directly result in a change of the Rydberg state population, but it can be a source of decoherence of the system.

Dephasing: laser frequency fluctuations due to technical limitations are a source of dephasing for the coupled atom-light system, since it leads to fluctuations of dressed-state energies. Typically this source of dephasing is common to all atoms. In addition the motion of the atoms can lead to dephasing when during the experiment the atoms move by a significant fraction of the optical wavelength and thus experience different phases of the coupling field. Since the atomic motion is thermal the resulting fluctuations are independent for all atoms.

Measurement induced decoherence: this can either be a destructive measurement or a non-demolition measurement. Even an ideal measurement constitutes a projection of the systems's quantum state. In the imaging scheme discussed in Ch. 5 and 6 the measurement arises from photon scattering from a rapidly decaying state. In our experiment this mechanism is especially important when studying energy transport between different Rydberg states.

Theoretical description

Formally the effect of decoherence on the time evolution of a system can be incorporated with the density matrix formalism by solving the Lindblad Master equation

$$\dot{\rho} = -\frac{i}{\hbar}[\hat{H}, \hat{\rho}] + \mathcal{L}[\hat{\rho}]. \tag{2.14}$$

This equation describes the time evolution of an ensemble average. The so-called Lindblad term $\mathcal{L}$ can be obtained by separating the Hamiltonian of the system into a coherent time-independent part and a fluctuating part (see e.g. [Breuer and Petruccione, 2002; Gardiner and Zoller, 2004]). This second part can contain fluctuations of the energy levels (the diagonal terms) as well as the coherent couplings (the off-diagonal terms). Assuming uncorrelated fluctuations and averaging over these fluctuations yields

$$\mathcal{L}[\hat{\rho}] = \sum_{n,m} \hat{L}_{n,m}\hat{\rho}\hat{L}_{n,m}^{\dagger} - \frac{1}{2}(\hat{L}_{n,m}^{\dagger}\hat{L}_{n,m}\hat{\rho} + \hat{\rho}\hat{L}_{n,m}^{\dagger}\hat{L}_{n,m}) \tag{2.15}$$

The off-diagonal terms $\hat{L}_{n,m\neq n} = \sqrt{\Gamma_{n,m}}|n\rangle\langle m|$ represent decays from state $|m\rangle$ to $|n\rangle$ with the respective decay constant $\Gamma_{n,m}$, and the diagonal terms $\hat{L}_{m,m} = \sqrt{\gamma_m}|m\rangle\langle m|$ reflect the dephasing of state $|m\rangle$ due to energy fluctuations, where γ_m specifies the dephasing rate. In the Lindblad equations the decay $\hat{L}_{n,m}$ leads to changes in the populations of states $|n\rangle$ and $|m\rangle$ with rate $\Gamma_{n,m}$, and to a decay of the coherences $|m\rangle\langle n|$ and $|n\rangle\langle m|$ with rate $\Gamma_{n,m}/2$. In contrast the dephasings $\hat{L}_{m,m}$ only lead to a decay of the coherences, i.e. the off-diagonal density matrix elements. The decay rate for the coherence between two particular states depends on their relative energy fluctuations. This description also captures laser dephasings which lead to fluctuating energies of the dressed states. Alternatively laser frequency fluctuations can be included by adding a phenomenological term $\mathcal{L}^{laser}[\hat{\rho}] = \sum_{n,m}\gamma_{nm}(\hat{\rho}|n\rangle\langle m| + |m\rangle\langle n|\hat{\rho})$ to eq. 2.14. Here the γ_{nm} quantify the frequency fluctuation of the laser field coupling the states $|n\rangle$ and $|m\rangle$. This approach can be of practical use when constructing the Lindblad operator for systems involving a large number of states. Note that the description of laser dephasing within the density matrix formalism holds for a single atom. For an ensemble of atoms the laser frequency fluctuations are common to all atoms. Therefore all atoms undergo the same phase evolution and can thus in principle still interfere with each other. This fact will be important for the formation of Rydberg aggregates as discussed in Ch. 4. In contrast, a mechanism which can decohere atoms independent of each other, is motional dephasing.

2.3 Experimental approach to ultracold Rydberg atoms

The experimental apparatus which was built during this thesis has to fulfill various requirements. First of all it has to allow for the preparation of cold and dense atomic samples in order to realize strongly interacting Rydberg systems. Fast duty cycles are required to obtain large statistical samples in a reasonable time. In addition the mechanical design has to be such that good optical access is preserved for all kinds of imaging, excitation and trapping. In our experiments we work with ^{87}Rb atoms since these are comparably straightforward to cool and trap. In the following the details of our experimental apparatus will be introduced. Ch. 2.3.1 describes the preparation of cold and dense clouds of ground state atoms. The ingredients required for Rydberg atom experiments will be described in Ch. 2.3.2. This includes the design of an electrode structure which allows to apply arbitrary electric fields and field gradients for Rydberg atom excitation, manipulation and detection. In addition our single atom sensitive detection scheme is discussed. A more detailed description of the complete apparatus can be found in [Hofmann *et al.*, 2013a; Hofmann, 2013].

2.3.1 Preparing ultracold and dense atomic samples

Cooling and Trapping in a magneto-optical trap

In order to perform fast duty cycles it is crucial to achieve a fast loading of the magneto-optical trap (MOT). We realize this by loading the three-dimensional (3D) MOT from a two-dimensional (2D) MOT [Dieckmann *et al.*, 1998]. The 2D-MOT creates a high-flux beam of cold atoms which is aligned towards the 3D-MOT and thus allows for much faster loading rates as compared to loading from a hot and undirected background gas.

We realize the 2D-MOT in a glass cell which is attached to our main vacuum chamber under an angle of 20°. A small hole of 800 μm diameter, through which the cold atom beam is guided, serves as a differential pumping stage, which allows to maintain very good vacuum in the main chamber (below 10^{-12} mbar) while at the same time allowing for high partial pressure of Rb in the glass cell. We use permanent magnets to create the required magnetic quadrupole field for the 2D-MOT in combination with Helmholtz coils, which allow to fine tune the magnetic field such that its zero crossing is aligned with the differential pumping tube. The gradient is chosen to be 16 G/cm. Four regions in the cell are illuminated with

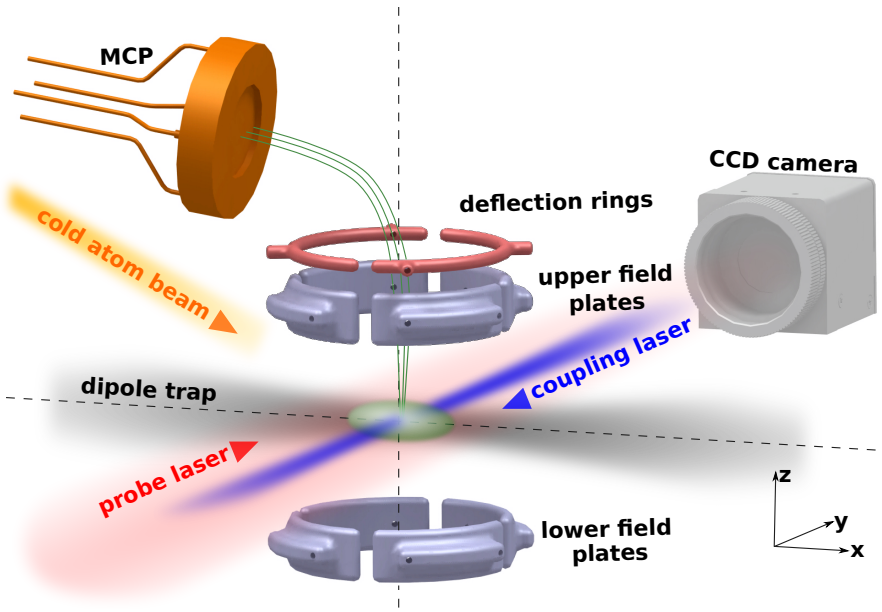

Figure 2.5: Schematic of the experimental setup. Sketched are the atomic cloud which is located in the center of an electrode structure. This electrode structure on the one hand serves to apply small electric compensation fields during the experiments. On the other hand fields as large as 1.2 kV/cm can be applied to ionize the Rydberg atoms. The ions are then guided to a microchannel plate detector (MCP) using an extra pair of electrodes (deflection rings). The atoms can be imaged on a CCD camera using absorption imaging. The laser beam at 480 nm for the Rydberg excitation is focused to the center of the atomic cloud in order to achieve reasonable coupling strengths.

cooling and repumping light, where each beam is retro-reflected and has a circular geometry with a diameter of 20 mm. The light for cooling in the two directions is provided from one optical fiber each and subsequently distributed to the four cooling regions by a combination of polarizing beam splitter cubes and wave plates. An additional laser beam of 7 mm diameter is aligned on the symmetry axis of the glass cell and serves to push the atoms through the differential pumping stage towards the center of the main chamber. The lasers we use for the 2D-MOT are a TOPTICA DLX 110 (1000 mW) diode laser for cooling and pushing and a home-built diode laser for repumping, which at the same time also serves as a repumper for the 3D-MOT. We achieve loading rates as large as $3.9 \times 10^9 s^{-1}$ when running at a dispenser current of 3.2 A. For routine operation we run at a lower dispenser current of 2.3 A yielding loading rates of $5 \times 10^8 s^{-1}$. Our particular setup is also described in detail in [Höltkemeier, 2011; Busche, 2011; Götz *et al.*, 2012; Hofmann, 2013]. An important advantage of a 2D-MOT in the context of Rydberg experiments is the

fact that only the ^{87}Rb *atoms* are cooled in the 2D-MOT whereas ions that are also produced by the dispenser remain hot and are thus very unlikely to pass through the differential pumping tube into the main chamber, where they could possibly lead to uncontrolled conditions for the Rydberg atom excitation.

The 3D-MOT is realized by six independently adjustable cooling beams of 20 mm diameter and an overall power of 125 mW obtained from a tapered amplifier system (TOPTICA TA100, 1500 mW). The magnetic field coils are situated outside the vacuum and built from hollow wires which allow for water cooling and thus for high currents. The details on their mechanical design can be found in [Hofmann, 2013]. We start loading with a magnetic field gradient of 10.5 G/cm and a cooling laser detuning of ≈ -19 MHz. After typically 2-4 s of loading we ramp up the magnetic field gradient to 14 G/cm in order to compress the cloud and thus to match its size to that of the optical dipole trap which is already on during the MOT loading. The compression is followed by a molasses phase during which we reduce the cooling as well as the repumping power while increasing the cooling detuning to -48 MHz. Turning the repumper off 2 ms in advance we end up with the atoms in the optical dipole trap being mainly prepared in the lowest hyperfine state $|5S_{1/2}, F = 1\rangle$. This preparation minimizes losses due to state changing collisions in the optical dipole trap.

Optical dipole trap

Cooling below MOT temperatures and overcoming the density limitations of a MOT requires to work with conservative potentials as e.g. magnetic traps, optical dipole traps or combinations of the two approaches. We chose to work with optical dipole traps since they have proven to allow for faster cooling cycles and they can also be switched off arbitrarily fast as compared to magnetic traps. In the framework of a Diploma thesis [Faber, 2011] we have designed a geometry for the optical dipole trap which is composed of three laser beams in total. Two beams of 120 μm waist are crossed under an angle of 5° to form a reservoir into which we initially load the atoms. Their diameter is chosen such that we can at the same time achieve a good spatial overlap with the MOT and realize sufficient trap depths. Crossing the two beams under a small angle provides much better axial confinement as compared to a single reservoir beam of the same power. A third beam (dimple beam) is tightly focused onto the atoms and crosses the reservoir under an angle of 45°. This tightly focused beam allows for large trap frequencies and thus for efficient thermalization required for fast evaporative cooling.

The three beams are provided by a high power laser system at a wavelength of 1064 nm. Initially we used a 50 W fiber amplifier (Nufern) seeded by a narrow band solid state laser (Innolight Mephisto 1 W). Later on this system was replaced by a 55 W solid state laser (Mephisto MOPA 55) because of degradation of the beam profile. Part of the overall power (typically up to 5 W) is used for the dimple beam. This beam is first enlarged to a size of ≈ 10 mm and then focused onto the atoms with a 230 mm focal length lens resulting in a beam waist of $\approx 10\,\mu$m (when diffraction limited). Depending on the experimental requirements we can also use either the dimple or the reservoir trap exclusively, e.g. to realize different dimensionalities of the cloud.

After loading into the dipole trap we hold the atoms for up to a few 100 ms for initial thermalization. If required we then start a series of evaporation ramps by reducing both the reservoir as well as the dimple power. As mentioned before we prepare the atoms in the lowest hyperfine state $|5S_{1/2}, F = 1\rangle$ at the end of the MOT cycle to prevent losses caused by state changing collisions. Although not used in daily operation we can reach Bose-Einstein condensation (BEC) with the scheme described above within an overall cycle duration of 4.5 s resulting in a BEC of 8×10^3 atoms. Realizing slightly longer cycles we have obtained up to 6×10^4 atoms in the condensate. Details of the evaporation ramps can be found in [Faber, 2011; Hofmann *et al.*, 2013a].

Preparing a well-defined ground state

In order to start from a well defined atomic ground state we make use of a microwave field to prepare the atoms in a single Zeeman state, e.g. $|5S_{1/2}, F = 2, m_F = +2\rangle$. Starting from the atoms in the optical dipole trap which are distributed among the three Zeeman states of the lower hyperfine state $|5S_{1/2}, F = 1\rangle$ (see also fig. 2.6) we set the microwave frequency to be resonant with the transition $|5S_{1/2}, F = 1, m_F = +1\rangle \rightarrow |5S_{1/2}, F = 2, m_F = +2\rangle$ at a finite magnetic field B_0 (typically $B_0 \approx 2.5$ G) and sweep the magnetic field adiabatically from $B_0 - \Delta B$ to $B_0 + \Delta B$ where typically $\Delta B \approx 0.05$ G. Due to the Zeeman shift this procedure is equivalent to a microwave frequency sweep and provides a robust and efficient way to transfer population between two states.

Timing of the experiment

The timing of the experiments is realized using LogicBoxes. The LogicBox is a FPGA (field programmable gate array) based system developed by the electronics

workshop of the Physikalisches Institut which features digital as well as analog inputs and outputs. It allows programming arbitrary experimental sequences with a time resolution of 100 ns (digital channels) and 5 μs (analog channels). The LogicBoxes are interfaced with a LabView Programm which allows to define and combine various experimental sub-sequences. A few other instruments are controlled from the same LabView interface, as e.g. the high and low voltage supplies (W-IE-NE-R MPOD mini Crate with modules for positive (EHS F030p-305-SHV) and negative (EHS F030n-305-SHV) high voltages, as well as a low voltage module with switchable polarity), a microwave synthesizer (Anritsu MG3697C) to realize transitions between Rydberg states, a fast oscilloscope (LeCroy WavePro 7000) for reading out the ion signals from the micro-channel plate detector (MCP) as well as different cameras for absorption imaging. The images as well as the ion traces are automatically analyzed immediately after acquisition and the results are written into a file.

2.3.2 Rydberg atom excitation and detection

Two-photon excitation scheme

We realize the excitation to Rydberg states using a two-photon scheme which involves an intermediate state ($5P_{3/2}$). The laser wavelengths required for this excitation scheme are ≈ 780 nm and ≈ 480 nm. The corresponding level scheme is sketched in fig. 2.6. The light at 780 nm is provided by a diode laser (TOPTICA DL100 pro, 120 mW) which illuminates the atomic cloud homogeneously. At the same time this light serves for absorption imaging of the ground state atoms. Whenever larger powers are required for excitation we recycle light from the MOT laser system (TOPTICA TA, 1500 mW). The blue light (480 nm) is provided by two frequency doubled diode laser systems (TOPTICA TA-SHG and TOPTICA TA-SHG pro) with an output power of 130 mW and up to 1 W of blue light, respectively. We stabilize the frequency of these lasers to an EIT resonance in a thermal vapor cell as described in [Abel *et al.*, 2009; Müller, 2010]. For switching the blue laser beams on and off we use electro-optical modulators (EOMs) in combination with mechanical shutters. In order to make sure that we work with only stretched transitions and can thus assume to have a clean three-level system we apply a magnetic field of typically 3 G along the excitation axis [Busche, 2011] and use appropriate laser polarizations.

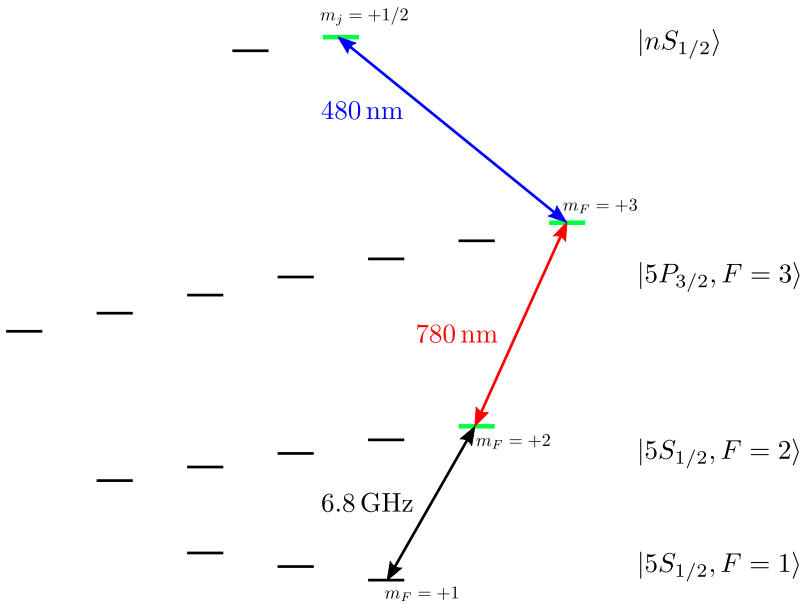

Figure 2.6: Relevant levels of ^{87}Rb in the presence of a small magnetic field. From the lowest hyperfine state we prepare the atoms in the state $|5S_{1/2}, F = 2, m_F = +2\rangle$ using a 6.8 GHz microwave sweep. This is the starting point for the three-level system (highlighted in green) that we couple optically with lasers at 780 nm and 480 nm. Note that the level spacings as sketched here are not to scale. Detailed information on the level scheme of Rubidium can be found in [Steck, 2001].

Stray field compensation

As mentioned in Ch. 2.1 Rydberg atoms have huge polarizabilities and therefore experience pronounced Stark shifts at fields as small as a few mV/cm. Hence stray electric fields have to be compensated as accurately as possible. To this end we have designed an electrode structure for field compensation [Müller, 2010]. It consists of two rings which are each cut into four equal segments. These segments (field plates) are symmetrically placed around the atoms as sketched in fig. 2.5 and can be individually supplied with different voltages. This geometry allows us to control fields and field gradients in arbitrary spatial directions. Simulations using SimION predict that stray field compensation below 5 mV/cm over a volume of 1mm^3 should be possible. The design of the electrode structure is shown in fig. 2.7 and discussed in detail in the following section.

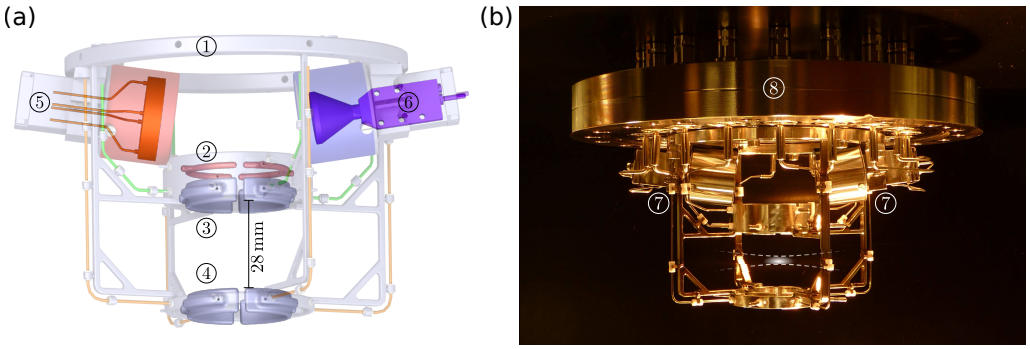

Figure 2.7: Electrode assembly for electric field control and for field ionization of Rydberg atoms. (a) Schematic drawing of the electrode assembly for electric field control and for field ionization of Rydberg atoms. A grounded supporting structure ① holds two deflection rings ② as well as four upper ③ and four lower ④ field plates in place, that are used to control the electric field landscape at the position of the atoms. Ion detection is possible with either a micro-channel plate detector (MCP) ⑤ or a channel electron multiplier detector (CEM) ⑥. (b) Photograph of the stainless steel structure which also shows the Faraday cages ⑦ that surround the detectors and the vacuum flange ⑧ with 18 high voltage connections. The position of the atom cloud and the orientation of the dipole trap are sketched on the photograph.

Field ionization detection

For Rydberg atom detection we make use of field ionization. The electrode structure used for field compensation therefore also serves to apply high voltages of up to $\pm 3000\,\mathrm{V}$ resulting in electric fields of up to $1200\,\mathrm{V/cm}$, which is sufficient to ionize Rydberg atoms with principal quantum number as small as $n \approx 23$ (classical ionization threshold as taken from [Gallagher, 1994]). To this end all the components used in the electrode structure have to stand voltages of $3\,\mathrm{kV}$, in particular in the fabrication process of the metal parts smooth surfaces have to be machined in order to prevent sparking. The high as well as the low voltages are provided by a combined device (Wiener MPOD). This device is controlled from the LabView interface via an ethernet connection and can thus not be programmed in real time. In order to realize fast electric field changes, e.g. in order to switch between (small) compensation and (large) ionization fields, we make use of Behlke switches which can be triggered from the LogicBox and have switching times as short as $\approx 300\,\mathrm{ns}$.

The apparatus contains two ion detectors: a channel electron multiplier (CEM, Dr. Sjuts KBL15RS) and a micro-channel plate detector (MCP, Hamamatsu F1551-21S). During this thesis we mainly used the MCP since it is suited for the detection

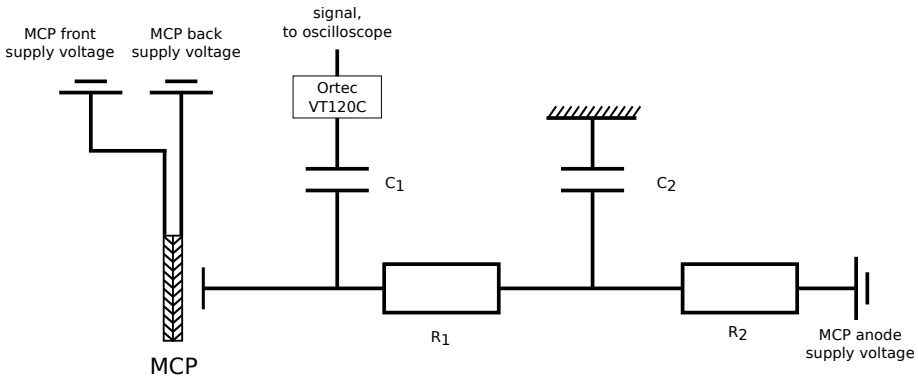

Figure 2.8: Readout scheme of the MCP. The MCP anode is supplied with -180 V which accelerates the secondary electrons from the MCP towards this anode. The capacity $C_1 = 100\,\text{pF}$ together with the input resistance of the preamplifier (50 Ω for ORTEC VT120C) determines the time constant of the readout scheme. In our case voltage spikes as narrow as 1.5 ns corresponding to single ions can clearly be resolved. C_2 =1 nF together with $R_2 = 1\,\text{M}\Omega$ buffers the supply voltage and thus prevents voltage spikes on the preamplifier as well as on the anode itself, which could otherwise be caused by abrupt switching of the supply voltage. $R_1 = 1\,\text{M}\Omega$ is chosen to be large as compared to the input resistance of the preamplifier.

of many ions, but at the same time also allows for the detection of very few and even single ions. In contrast, the CEM which has only one amplification channel cannot handle large ion signals. This is due to a dead time after any detection event which is caused by a charge depletion in the channel walls. In an MCP also each channel has a dead time, but since it is very unlikely for two ions to hit the same channel, many ions can still be simultaneously detected.

As can be seen in fig. 2.7 both detectors are situated in a plane above the atoms in order to not obscure the optical access to the atoms. To guide the ions onto the ion detectors we therefore added two additional electrodes shaped as half-rings which are located above the upper field plates and help to guide the ions around the corner. The major source for electric stray fields are the supply voltages of the ion detectors. For this reason these are placed inside Faraday cages in order to shield the stray field as much as possible. The entrance of the cage is realized using a highly transparent mesh. Despite the shielding the supply voltages of the detectors still create fields of $\approx 0.6\,\text{V/cm}$ at the position of the atoms as can be seen in fig. 2.12 and will be discussed later in the context of optimized stray field compensation.

The whole electrode structure together with the Faraday cages containing the ion detectors is mounted to the top flange of the vacuum chamber. The supply voltages

are provided using 18 SHV feedthroughs (8 electrodes, 2 deflection rings, 2 Faraday cages and 3 connections for each of the two ion detectors) which are welded into the top flange. Wherever possible the wires inside the vacuum are guided behind the holding structure in order to reduce stray fields at the position of the atoms as much as possible. Insulating pieces inside the vacuum were fabricated from Macor, a machinable glass-ceramic.

In order to detect the $^{87}Rb^{+}$ ions we apply -1900 V to the front surface of the MCP and -280 V to its back. The signal is read out from the anode (-180 V) via a capacitor as depicted in fig 2.8. After pre-amplification (ORTEC VT120C) the signal is displayed and saved on a fast oscilloscope (LeCroy WavePro 7000, 1 GHz). The 100 pF capacity of C_1 together with the input resistance of the preamplifier of 50 Ω determines the time resolution of the readout scheme. In our case we are able to resolve signals corresponding to single ions, which are as narrow as 1.5 ns. The second capacitor, C_2 =1 nF, together with the resistor $R_2 = 1\,\mathrm{M}\Omega$ buffers the supply voltage and thus prevents voltage spikes on the preamplifier as well as on the anode itself which could otherwise be caused by abrupt switching of the supply voltage. $R_1 = 1\,\mathrm{M}\Omega$ is chosen to be large as compared to the input resistance of the preamplifier and thus forces the signal into the preamplifier.

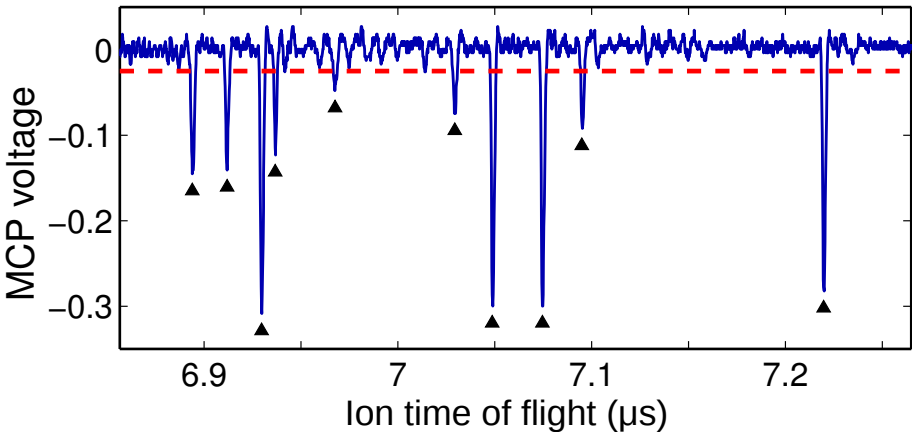

Figure 2.9: Typical ion trace as obtained from the MCP. Each voltage spike (indicated by the black triangles) above a certain threshold (red dashed line) corresponds to a single detection event. Depending on the ionization field configuration the ions are spread over a certain range of arrival times. From the number and width of the spikes we estimate the probability for temporal overlap of two spikes, thereby judging on whether we can simply count the spikes to get a measure for the Rydberg atom number.

MCPs as well as CEMs have a finite detection efficiency, i.e. not every ion hitting

the detector creates a voltage spike in the signal. This detection efficiency depends on the energy of the incoming particles as well as on the angle at which they hit the channels. In our particular setup we can also not consider the guiding of the ions to the detector and the transmission through the mesh to be perfect. Overall we estimate the detection efficiency of our system to be around 40 %. The avalanche amplification mechanism in addition leads to a pulse height distribution, i.e. there is no fixed gain for one ion but instead the voltage spikes amplitudes cover a large range.

At low count rates (at our typical settings for up to 10 detection events) each voltage spike as depicted in fig. 2.9 can be assigned to a single detection event since the probability for the spikes to overlap is negligible. The number of spikes in this range together with a particular detection efficiency therefore serves as a good measure for the number of Rydberg atoms. At higher count rates the spikes are more likely to overlap. In this case the integral of the MCP signal is a better measure for the number of Rydberg atoms. Note that the fields used for ionization strongly influence the spread of the ions on the MCP. Therefore the number of spikes at which counting does not yield reliable information any more has to be determined independently for each field configuration.

Optimizing parameters using an evolutionary algorithm

In the experiments we routinely scan various experimental parameters in order to find the best conditions. However, in situations where several parameters are coupled they cannot be easily optimized by independent scans because their effects cannot be separated. This is usually the case for the voltages we apply to the electrode structure, for stray field compensation as well as for guiding the ions to the MCP. But also in other parts of the experiment we find coupled parameters as e.g. the laser parameters at the end of the molasses, which are critical for efficiently loading the optical dipole trap. To still optimize these parameters we have (in the framework of a Bachelor's thesis) implemented into our experimental control an evolutionary algorithm [Argus, 2013] which searches the best parameters within a certain window without trying every possible combination of parameters.

An evolutionary algorithm works as sketched in fig 2.10 (see e.g. [Weise, 2009]): first of all an initial population, i.e. a finite number of possible parameter combinations ("individuals"), is created by sampling from a uniform random distribution in a restricted search space. This population of individuals is then tested experimentally and their performance ("fitness") is evaluated. The individuals which performed best

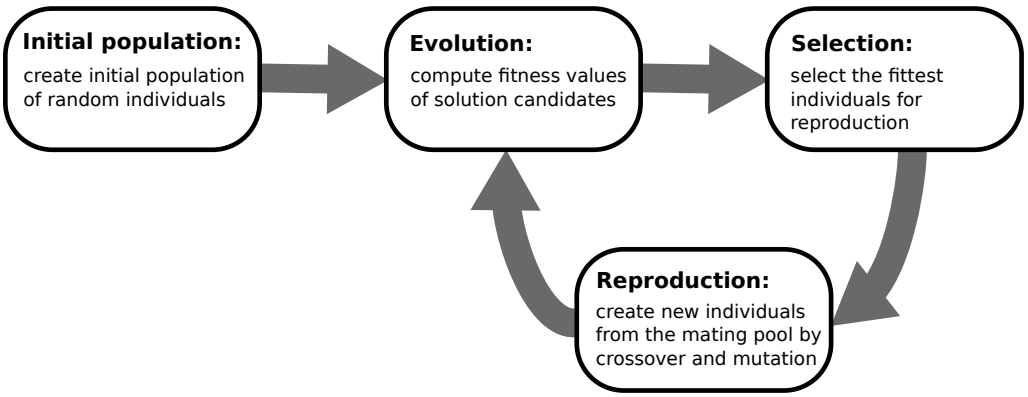

Figure 2.10: Illustration of an evolutionary algorithm. In a first step an initial population is created of which the performance is tested in a second step. Those individuals which perform best are selected for reproduction, i.e. they serve as a pool from which a new generation of individuals is created. Figure adapted from [Weise, 2009]

are selected and serve as a pool from which a new generation of individuals is created for further optimization. Using biological language these new individuals are created by crossover and mutation i.e. by mixing the properties of the parents combined with additional random variation of parameters. This crossover and mutation can be realized using various approaches where the amount of randomness has to be balanced such that the search does not take too long (too much randomness) but at the same time it is not too much restricted to an initially found local optimum (not enough randomness). The best choice for this procedure as well as for the initial population size depends strongly on the optimization problem. For our experimental applications these choices are discussed in detail in [Argus, 2013].

The implementation of the algorithm into the experiment is sketched in fig. 2.11. The optimization is set up via the LabView interface where the parameters for the optimization, the initial size of the population and the boundaries of the search space are specified. The optimization algorithm, which is implemented in Python, receives this information and creates an initial population which is given back to the control program. The control program launches a set of experiments using the initial population of parameter combinations. The results of these experiments are obtained from an analysis program written in Matlab and saved into a table. The values of the quantity that is to be optimized are read from this table and used to create a new generation of individuals which is again passed to the control program.

We have used the evolutionary algorithm for three different experimental applications. An important step is e.g. the initial loading of the dipole trap which depends

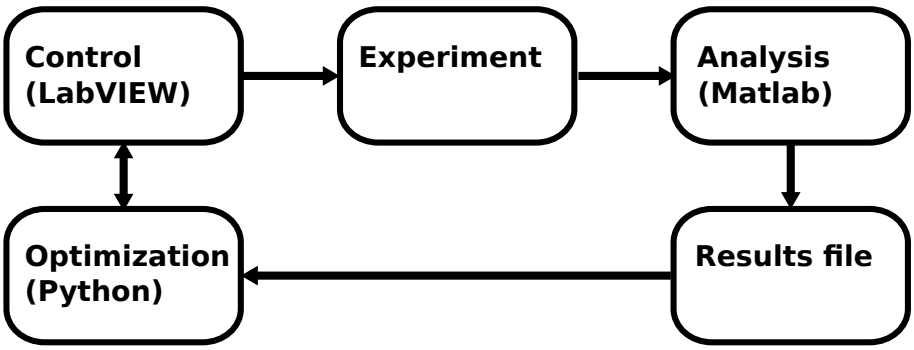

Figure 2.11: Sketch of the implementation of the algorithm. Via the LabView control program the optimization (implemented in Python) is configured and the experiments are are initiated with the parameters provided by the optimization program. The experiments are analyzed using Matlab and the results are written into a table from which they are again read by the Python program.

crucially on the powers and detunings of the MOT lasers at the end of the molasses phase. Since the effects of these parameters are strongly coupled they represent a typical set of parameters to be optimized using an evolutionary algorithm. Also the voltages applied for field ionization and subsequent guiding of the ions towards the detector have been optimized accordingly. Since we use at least four different voltages for guiding, and since a voltage applied to an electrode changes the electric field not only in one but in all three directions, the applied voltages cannot be independently scanned. With the evolutionary algorithm, however, we have been able to optimize these voltages very efficiently.

The optimization of the compensation fields is slightly more involved since in principle the resonance position would have to be determined for each combination of voltages. To avoid taking a full spectrum for every combination of voltages we exploit the quadratic Stark effect of Rydberg S states where any finite electric field reduces the energy of the state and thus leads to a smaller resonance frequency. Starting from a Rydberg excitation spectrum at a random electric field with a resonance frequency ν_0 we can in the next step detune our excitation frequency to a slightly higher frequency $\nu_0 + \delta\nu$. The detuning $\delta\nu$ could e.g. be chosen such that the excitation signal has dropped to 50% at $\nu_0 + \delta\nu$. The voltages for stray field compensation can now be optimized by maximizing the excitation signal, e.g. the number of ions, at the fixed frequency $\nu_0 + \delta\nu$. Any combination of voltages leading to larger electric field at the position of the atoms would shift the resonance to smaller frequencies $\nu < \nu_0$ from which the actual excitation frequency $\nu_0 + \delta\nu$ is farther detuned, thus leading

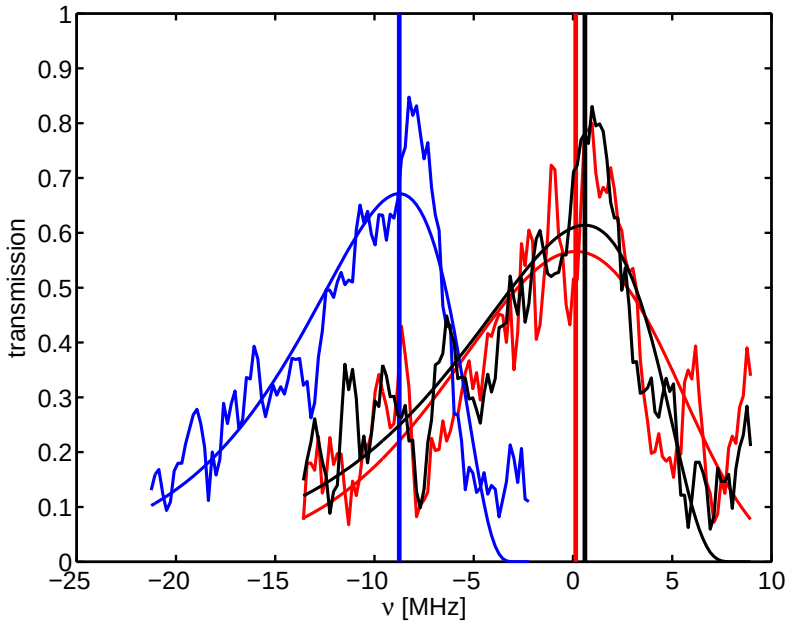

Figure 2.12: EIT transmission spectra for different field configurations. The maximum of the transmission indicates the position of the resonance. A scan without MCP supply voltage and without any compensation fields (red curve) serves as a reference for a situation close to zero field. With the MCP supply voltage turned on but still without compensation fields (blue curve) we find a shift of the resonance frequency of -8.9 MHz corresponding to a field of $\approx 0.6\,\mathrm{V/cm}$. After optimizing the voltages for stray field compensation we obtain a spectrum (black curve) which is almost on top of the "voltage-free" spectrum, indicating very good compensation of the field caused by the MCP voltage. The fits are exponential-gaussian hybrids as discussed in [Lan and Jorgenson, 2001]. The vertical lines indicate the resonance positions obtained from the fits.

to a smaller excitation probability. In contrast, a voltage combination reducing the electric field at the position of the atoms shifts the resonance to larger frequencies, i.e. closer to $\nu_0 + \delta\nu$, thereby enhancing the excitation probability. Thus optimizing on the excitation signal of a blue detuned excitation reduces the electric field at the position of the atoms. If after one round of optimization the spectrum has significantly shifted to larger frequencies the procedure might have to be repeated at even larger excitation frequencies to not just reduce the fields but to actually reach the minimum.

In our experiment we start by taking a reference spectrum without any voltages applied to the electrodes and without supply voltage for the MCP detector. This should be an almost field free situation since we suspect the MCP supply voltage to

be the largest source of stray fields. Since without the MCP supply voltage we cannot take excitation spectra based on field ionization we determine the resonance position using electro-magnetically induced transparency (EIT), which will be discussed in detail in Ch. 3. Essentially the atoms feature a transparency resonance for the 780 nm light (see fig. 2.6) when the 480 nm light couples resonantly to a Rydberg state. The reference EIT spectrum using the Rydberg state $50S$ is shown in fig. 2.12 (red curve). When turning the MCP supply voltage on we find the EIT resonance shifted by $-8.9\,\mathrm{MHz}$ (blue curve). Considering the polarizability of $50.61\,\mathrm{MHz/(V/cm)^2}$ for the state $50S$ [O'Sullivan and Stoicheff, 1985] this corresponds to a field of $\approx 0.6\,\mathrm{V/cm}$ which has to be compensated. After running the field optimization by maximizing the ion signal as discussed above we take again an EIT spectrum with the MCP supply voltage and the compensation fields turned on in order to judge on the success of the optimization (black curve). We find the spectrum lying almost on top of the reference spectrum indicating that the stray fields induced by the MCP supply voltage can be very well compensated. In order to compensate stray fields even more precisely the procedure as described above would have to be repeated at higher lying Rydberg states which are even more sensitive to electric fields.

Chapter 3

Coupling light to interacting three-level atoms

This chapter is partially based on the following publications:

Coherent population trapping with controlled interparticle interactions
H. Schempp, G. Günter, C. S. Hofmann, C. Giese, S. D. Saliba, B. D. DePaola, T. Amthor, M. Weidemüller, S. Sevinçli, T. Pohl
Physical Review Letters **104**, 173602 (2010)

Sub-Poissonian statistics of Rydberg-interacting dark-state polaritons
C. S. Hofmann, G. Günter, H. Schempp, M. Robert-de-Saint-Vincent, M. Gärttner, J. Evers, S. Whitlock, M. Weidemüller
Physical Review Letters **110**, 203601 (2013)

In atomic three-level systems there is a variety of effects such as Stimulated Raman Adiabatic Passage (STIRAP) [Bergmann *et al.*, 1998], Coherent Population Trapping (CPT) [Arimondo, 1996] and Electromagnetically Induced Transparency (EIT) [Fleischhauer *et al.*, 2005], which all rely on the population of a dark state. These effects have been widely investigated, ranging from applications for light storage protocols [Phillips *et al.*, 2001], to the preparation of molecules in their absolute ground state [Ni *et al.*, 2008]. Combining these intensely studied phenomena with strong interactions in ultracold Rydberg gases has recently lead to the discovery of new interesting effects. First experiments on dark resonances in interacting systems [Pritchard *et al.*, 2010], including our own work [Schempp *et al.*, 2010], have revealed a suppression of dark resonances with increasing interaction strength. Only in the

last three years different groups have realized effective photon-photon interactions using EIT in combination with strong Rydberg interactions [Dudin and Kuzmich, 2012; Peyronel *et al.*, 2012; Maxwell *et al.*, 2013; Firstenberg *et al.*, 2013]. These effects can be understood in the framework of dark-state polaritons (DSP) as proposed by [Fleischhauer and Lukin, 2000]. After a short review of the mechanisms and the mathematical description of CPT and EIT for non-interacting systems, i.e. for independent atoms, the concept of DSPs will therefore be introduced in Ch. 3.1.2. This concept provides a picture for how interatomic interactions change the optical as well as the atomic properties under EIT conditions. Our studies of CPT in strongly interacting systems will be presented in Ch. 3.2.1. In Ch. 3.2.2-3.2.4 we discuss our work on interacting dark-state polaritons. On the one hand these interactions become apparent as an optical nonlinearity, but at the same time they are also reflected in the counting statistics of the polaritons which can be accessed by measuring their matter part.

3.1 Three-level effects in non-interacting systems

3.1.1 Dark states and electromagnetically induced transparency

Atom-light interactions

In the following we will review some properties of atomic three-level systems coupled to two coherent light fields. Our particular system is a so-called ladder system as depicted in fig. 3.1, however, most of the effects discussed here can be directly mapped onto so-called Λ-systems comprised of two ground states and one excited state. The ground state $|g\rangle$, the excited state $|e\rangle$ and a highly excited Rydberg state $|r\rangle$ are the relevant levels for most of the experiments discussed in this thesis, and they are coherently coupled by two laser fields ω and Ω, respectively. For the theory introduced here it is of particular importance that $|r\rangle$ is long-lived as compared to $|e\rangle$, i.e. for the decay rates we assume $\Gamma_e \gg \Gamma_r$.

The Hamiltonian of an atom interacting with two light fields has three contributions describing the bare atom, the light field and the coupling between atom and light field. A convenient basis for this combined system are the so-called dressed states which contain information on both the bare atomic levels as depicted in fig. 3.1

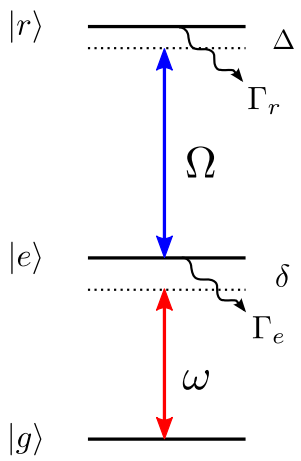

Figure 3.1: Relevant properties of the three-level systems discussed in this thesis. The three levels (ground state $|g\rangle$, excited state $|e\rangle$ and Rydberg state $|r\rangle$) are coherently coupled by two laser fields of coupling strengths ω and Ω. The states $|e\rangle$ and $|r\rangle$ are subject to decay with decay constants Γ_e and Γ_r, respectively.

as well as on the light field:

$$|1\rangle = |g, n+1, N\rangle \tag{3.1}$$
$$|2\rangle = |e, n, N\rangle\,, \tag{3.2}$$
$$|3\rangle = |r, n, N-1\rangle \tag{3.3}$$

where n and N are the number of photons in the laser fields ω and Ω, i.e. an atomic excitation comes along with the reduction of the number of photons. The energy difference between the dressed states is therefore given only by the detunings δ and Δ of the laser fields from the atomic transition frequencies.

Using the dipole approximation and the rotating wave approximation (see e.g. [Scully and Zubairy, 1997]) the Hamiltonian in the basis of the dressed atomic states $|1\rangle$, $|2\rangle$ and $|3\rangle$ is given by

$$H = \hbar \begin{pmatrix} -\delta & \omega/2 & 0 \\ \omega/2 & 0 & \Omega/2 \\ 0 & \Omega/2 & \Delta \end{pmatrix} . \tag{3.4}$$

where ω and Ω are the Rabi frequencies of the transitions $|g\rangle \leftrightarrow |e\rangle$ and $|e\rangle \leftrightarrow |r\rangle$), respectively.

Dark states

To gain a more intuitive understanding of the effects mentioned above it is instructive to choose the following states as a basis

$$|b\rangle = \frac{1}{\sqrt{\omega^2+\Omega^2}}(\omega\,|1\rangle + \Omega\,|3\rangle) \tag{3.5}$$

$$|2\rangle = |2\rangle \tag{3.6}$$

$$|d\rangle = \frac{1}{\sqrt{\omega^2+\Omega^2}}(\Omega\,|1\rangle - \omega\,|3\rangle)\,. \tag{3.7}$$

The appearance of a dark resonance e.g. can directly be seen when transforming the Hamiltonian of the coupled atom-light system (eq. 3.4) into this new basis. The states 3.5 - 3.7 can be obtained from the dressed atomic states $|1\rangle$, $|2\rangle$ and $|3\rangle$ by applying the unitary transformation

$$T = \frac{1}{\sqrt{\omega^2+\Omega^2}} \begin{pmatrix} \omega & 0 & \Omega \\ 0 & \sqrt{\omega^2+\Omega^2} & 0 \\ \Omega & 0 & -\omega \end{pmatrix} \tag{3.8}$$

Hence the Hamiltonian in the new basis reads

$$\widetilde{H} = T^\dagger H T = \hbar \begin{pmatrix} \frac{-\delta\omega^2+\Delta\Omega^2}{\omega^2+\Omega^2} & \frac{1}{2}\sqrt{\omega^2+\Omega^2} & -\frac{(\delta+\Delta)\omega\Omega}{\omega^2+\Omega^2} \\ \frac{1}{2}\sqrt{\omega^2+\Omega^2} & 0 & 0 \\ -\frac{(\delta+\Delta)\omega\Omega}{\omega^2+\Omega^2} & 0 & \frac{\Delta\omega^2-\delta\Omega^2}{\omega^2+\Omega^2} \end{pmatrix}\,. \tag{3.9}$$

We see that on two-photon resonance ($\delta = -\Delta$) only the states $|b\rangle$ and $|2\rangle$ are coupled while the state $|d\rangle$ is not coupled to any other state

$$\widetilde{H} = \hbar \begin{pmatrix} \Delta & \frac{1}{2}\sqrt{\omega^2+\Omega^2} & 0 \\ \frac{1}{2}\sqrt{\omega^2+\Omega^2} & 0 & 0 \\ 0 & 0 & \Delta \end{pmatrix}\,. \tag{3.10}$$

i.e. $|d\rangle$ is a long-lived eigenstate of the coupled atom-light system. Since it is decoupled from the light field, $|d\rangle$ is called a dark state. The dark state can be populated due to spontaneous decay of state $|2\rangle$ or be prepared via adiabatic passage. However, once the atoms have reached the dark state, they are trapped in there. This fact has consequences for the light field propagation as well as for the atomic state populations. While the intermediate state $|2\rangle$ is not at all populated the populations of states $|1\rangle$ and $|3\rangle$ are given by $\frac{\Omega^2}{\omega^2+\Omega^2}$ and $\frac{\omega^2}{\omega^2+\Omega^2}$ respectively.

Optical Bloch Equations

Knowing the Hamiltonian as given in eq. 3.4 the coherent evolution of the system can be calculated. Within the density matrix formalism this time evolution reads

$$\dot{\rho} = -\frac{i}{\hbar}[H, \rho] \tag{3.11}$$

However, in order to capture incoherent processes such as decay and dephasing, additional terms, the so-called Lindblad terms, have to be taken into account:

$$\dot{\rho} = -\frac{i}{\hbar}[H, \rho] + \mathcal{L}_{deph}(\rho) + \mathcal{L}_{dec}(\rho) \tag{3.12}$$

Here the laser dephasings γ_p and γ_c are incorporated as a decay of coherences, such that in our three-level system $\mathcal{L}_{deph}(\rho)$ reads as

$$\mathcal{L}_{deph}(\rho) = \begin{pmatrix} 0 & \gamma_p\rho_{12} & (\gamma_p+\gamma_c)\rho_{13} \\ \gamma_p\rho_{12} & 0 & \gamma_c\rho_{23} \\ (\gamma_p+\gamma_c)\rho_{13} & \gamma_c\rho_{23} & 0 \end{pmatrix}. \tag{3.13}$$

$\mathcal{L}_{dec}$ accounts for population decays and the resulting loss of coherence. In its general form it reads

$$\mathcal{L}_{dec}(\rho) = -\frac{1}{2}\sum_k (C_k^\dagger C_k \rho + \rho C_k^\dagger C_k) + \sum_k C_k \rho C_k^\dagger \tag{3.14}$$

where the sums run over all possible decay channels. C_k expresses the decay strength and the involved states of the kth decay channel. In our specific system we have to account for two decay channels, namely from $|e\rangle$ to $|g\rangle$ with strength Γ_e and from $|r\rangle$ to $|e\rangle$ with strength Γ_r. Therefore the sums in eq. 3.14 have two contributions which are

$$C_{ge} = \sqrt{\Gamma_e}|g\rangle\langle e| \tag{3.15}$$

$$C_{er} = \sqrt{\Gamma_r}|e\rangle\langle r| \tag{3.16}$$

Having the set of eqs. 3.12 at hand allows for the calculation of the time evolution of all populations and coherences. Eqs. 3.12 are called Optical Bloch equations (OBE).

Electromagnetically Induced Transparency

As mentioned above the population of the dark state $|d\rangle$ comes along with the atoms being transparent for the light field. I.e., the presence of the light field Ω, also often referred to as the coupling field Ω_c, changes the optical properties of the light field ω, also referred to as the probe field Ω_p, from absorbing to transparent. The width

of this transparency resonance is determined by the Rabi frequencies as can be seen from the respective coupling element in eq. 3.9. In addition finite laser linewidths as discussed in the previous section can broaden and smear out the resonance. For $\omega, \Omega \ll \Gamma_e$ the resonance width can be particularly narrow. In an atomic Mott insulator e.g., where motional dephasing is minimized, EIT transmission windows of 81 Hz width have been realized [Schnorrberger *et al.*, 2009].

Solving the OBEs (eq. 3.12) yields expressions for all coherences and populations. Of particular interest is ρ_{12} which relates to the optical susceptibility χ of the lower transition as

$$\chi = -\chi_0 \frac{\Gamma_e}{\omega} \rho_{12} \tag{3.17}$$

where $\chi_0 = \sigma_0 \rho_0 / k$ incorporates the resonant absorption cross section $\sigma_0 = 3\lambda^2/(2\pi)$ of the atoms, the atomic density ρ_0 and the wave vector $k = 2\pi/\lambda$ (see e.g. [Pritchard, 2011]). Solving for the steady state of the OBEs (i.e. $\dot{\rho} = 0$) with parameters $\Omega = 2\pi \times 2\,\mathrm{MHz}$, $\omega = 2\pi \times 0.5\,\mathrm{MHz}$, $\Delta = 0$, decay rates $\Gamma_e = 2\pi \times 6.1\,\mathrm{MHz}$ and $\Gamma_r = 2\pi \times 3\,\mathrm{kHz}$ and laser dephasings $\gamma_p = 2\pi \times 0.1\,\mathrm{MHz}$ and $\gamma_c = 2\pi \times 0.1\,\mathrm{MHz}$ we obtain the spectra shown in fig. 3.2 (blue lines). For comparison the red lines show the results for $\Omega = 0$, i.e. the bare two-level response. The three graphs show the imaginary (left) and the real (center) part of ρ_{12} as well as the Rydberg population ρ_{33} (right). As expected from the discussion on the dark states we find $\mathrm{Im}[\rho_{12}]$, which determines the absorption of the probe light, close to 0 for $\delta = 0$. In addition $\mathrm{Re}[\rho_{12}]$, determining the group index of the atomic medium, features a steep positive slope which results in a reduced group velocity v_{gr} since

$$v_{gr} = \frac{c}{n_{gr}} = \frac{c}{n(\omega_p) + \omega_p \frac{dn}{d\omega_p}} \tag{3.18}$$

where ω_p is the frequency of the probe field. The narrower the EIT width can be made the steeper the slope $dn/d\omega_p$ will be, resulting in a smaller group velocity.

In some special cases the OBEs can be simplified to yield analytic expressions e.g. for the quantities displayed in fig. 3.2. Analyzing the steady state (i.e. $\dot{\rho} = 0$) in the weak probe limit ($\omega \ll \Omega, \Gamma_e$) yields an analytic solution for the width of the transparency window

$$\mathcal{W}_{EIT} = \frac{\Omega^2}{2\Gamma_e} \tag{3.19}$$

as well as for ρ_{12},

$$\rho_{12} \approx \frac{i\Gamma_{13}\omega}{\Gamma_{12}\Gamma_{13} + \Omega^2} \tag{3.20}$$

where we have defined the rates $\Gamma_{12} = \Gamma_e + \gamma_p + 2i\delta$ and $\Gamma_{13} = \gamma_p + \gamma_c + 2i(\delta + \Delta)$. We see that e.g. Ω can be tuned in order to control the group velocity. Simplifications

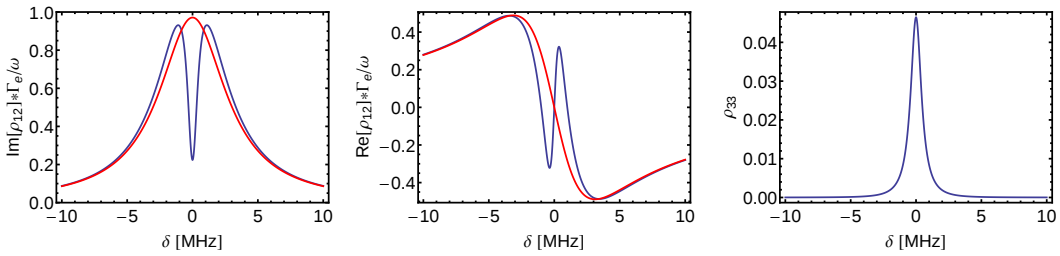

Figure 3.2: Steady state of the imaginary (left) and real (center) part of ρ_{12} as well as the Rydberg population ρ_{33} (right) as a function of the probe detuning δ. In the presence of a resonant coupling laser field Ω the absorption ($\sim \mathrm{Im}[\rho_{12}]$) shows the characteristic dip on resonance (blue line) while for $\Omega = 0$ we obtain the well-known Lorentzian absorption profile of a two-level atom (red line). The real part $\mathrm{Re}[\rho_{12}]$ shows a steep positive slope associated with a small group velocity. Parameters are $\Omega = 2\pi \times 2\,\mathrm{MHz}$, $\omega = 2\pi \times 0.5\,\mathrm{MHz}$, $\Delta = 0$, $\Gamma_e = 2\pi \times 6.1\,\mathrm{MHz}$, $\Gamma_r = 2\pi \times 3\,\mathrm{kHz}$, $\gamma_p = 2\pi \times 0.1\,\mathrm{MHz}$ and $\gamma_c = 2\pi \times 0.1\,\mathrm{MHz}$.

similar to that in eq. 3.20 can be made for the other entries of the density matrix (see [Hofmann *et al.*, 2014]).

3.1.2 Dark-state polaritons

We have seen in the previous section that $\omega \ll \Omega$ is a very interesting situation and that the group velocity, e.g. can become extremely slow for particularly small ω, Ω. [Fleischhauer and Lukin, 2000] have shown that in the limit of very weak probe field strengths, in particular in the limit of single probe photons, an adequate description of EIT is the concept of dark-state polaritons (DSP). In this description the coupling field Ω is treated as a classical field whereas the probe field is treated in terms of single quanta. The DSP is a superposition of an electromagnetic excitation (a probe field photon) and a collective atomic excitation in state $|r\rangle$ shared among N atoms. This concept of collective excitations is justified as long as the density of probe field photons is much smaller than the atomic density, which is the case in all our experiments. As discussed in [Fleischhauer and Lukin, 2002] a DSP can mathematically be written as

$$|D, 1\rangle = \cos(\theta)|g, 1\rangle_N - \sin(\theta)|r, 0\rangle_N \tag{3.21}$$

i.e. a superposition of all the atoms being in the atomic ground state $|g\rangle$ while the probe field contains one photon, and the photon being converted into an atomic

excitation $|r\rangle$. The mixing angle θ, which at the same time determines the group index n_{gr} of the atomic medium, is given by

$$\tan^2(\theta) = \frac{6\pi c\rho\Gamma_e}{k_p^2\Omega^2} \approx n_{gr}. \tag{3.22}$$

Here c is the speed of light, Γ_e the decay rate of the intermediate state, $k_p = 2\pi/\lambda_p$ the wave number of the probe field photon and ρ the atomic density. Tuning the atomic density ρ or the coupling field strength Ω therefore allows to change the character of the DSP from a photon-like particle moving at the speed of light into a matter-like particle moving at a reduced group velocity. While the absorption of a photon is usually a dissipative process and therefore irreversible, the conversion into a DSP is a coherent and fully reversible process which has been proposed in the context of an interface for quantum information [Fleischhauer and Lukin, 2000; Fleischhauer and Lukin, 2002] and experimentally demonstrated in e.g. [Phillips *et al.*, 2001].

3.2 Dark resonances in interacting systems

The above discussion was dealing with the treatment of individual three-level atoms. The situation becomes of course more involved when it comes to atoms interacting with each other. In our particular scheme the atoms only interact when they are both in the Rydberg state $|r\rangle$. As was discussed in Ch. 2.1 these interactions come along with a level shift. Hence one could assume that the dark resonance would be shifted as well.

However, in our experiments on CPT in interacting systems [Schempp *et al.*, 2010] we found no shift of the dark resonance and almost no broadening. Instead we found the amplitude of the dark resonance decrease with increasing interactions. [Pritchard *et al.*, 2010] found a similar behavior when investigating EIT resonances in interacting systems, namely a reduced transparency due to interactions. In our later work on EIT in interacting systems ([Hofmann *et al.*, 2013b]) we were even able to explore the full range from an almost transparent to a completely absorbing medium when increasing the interaction strength. Many-body theories can reproduce some of the experimental data using density matrix expansion [Schempp *et al.*, 2010] or Monte Carlo simulations using many-body rate equations [Ates *et al.*, 2011; Sevinçli *et al.*, 2011a]. However, these approaches do not provide a very intuitive picture of the underlying processes.

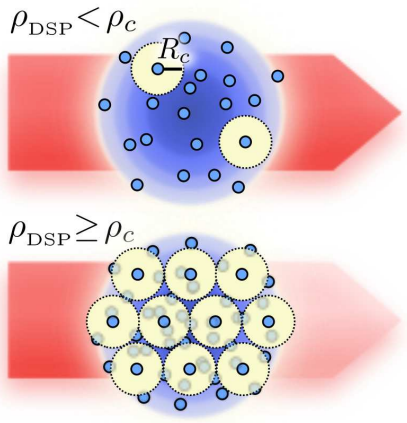

Figure 3.3: Low density of DSPs inside the medium (top) vs. dense packing of DSPs (bottom). The density of DSPs in the medium is determined by both the probe field intensity, i.e. the flux of probe field photons, as well as the atomic density which determines the group velocity. In an optically thick medium every photon that cannot be converted into a DSP is resonantly scattered from the ground state atoms thereby reducing the transparency of the medium.

As discussed in Ch. 3.1.1 the crucial condition for the existence of a dark state is two-photon resonance, i.e. $\delta = -\Delta$. In interacting systems this condition can be broken due to interaction induced level shifts. The consequences of this level shift can be well understood in terms of dark-state polaritons (DSPs) as introduced in Ch. 3.1.2. When entering an atomic medium a single probe photon is coherently converted into a DSP (eq. 3.21) with a mixing angle depending on the atomic density. This comes along with a reduced group velocity as well as a finite amplitude of the matter part of the polariton. At the typical atomic densities in cold atom experiments the mixing angle is such that the amplitude of the matter part $\sin(\theta) \approx 1$. When leaving the atomic sample the polariton is coherently converted back into a photon, i.e. into a polariton with $\sin(\theta) = 0$ due to the vanishing atomic density. Hence the photon has experienced a transparent medium. The situation changes when a second photon approaches the atomic cloud within a small time window. The first photon is still being converted into a DSP, however, since this goes along with a Rydberg excitation, its presence induces a level shift on the Rydberg states of the surrounding atoms. This level shift breaks the two-photon resonance, thereby preventing the second photon to be converted into a DSP. Only once the DSP has moved by a distance comparable with the range of the interactions, a subsequent

photon can be converted into a DSP. Any photon reaching the atomic sample before this cannot be converted into a DSP. Instead these photons experience effective two-level atoms and are thus absorbed according to Beer's law. The time it takes until the first DSP has moved sufficiently far away is determined by the range of the interaction potential as well as by the group velocity, which in turn is determined by the atomic density. The overall degree of transparency also depends on the overall number of incoming photons. Since the absolute number of photons which can pass through the atomic sample at the same time is limited, all excess photons are absorbed, thereby reducing the overall transparency. To summarize, the degree of transparency is determined by the density of DSPs inside the medium, which mainly depends on the atomic density, the amount of probe field photons and the range of the interaction potential. The suppression of EIT at high densities and/or large probe field intensities [Pritchard *et al.*, 2010; Hofmann *et al.*, 2013b], observed with macroscopic photon numbers, can be understood in this microscopic picture. The mechanism described above is also sketched in fig. 3.3.

Following the above described picture and looking at the sketch of the densely packed DSPs in fig. 3.3 the transmitted light should be highly correlated with a characteristic time between two photons. Indeed this anti-bunching has recently been observed [Dudin and Kuzmich, 2012; Peyronel *et al.*, 2012; Maxwell *et al.*, 2013] in the intensity correlations of the transmitted light field.

The ratio of Rabi frequencies ω/Ω determines the population in the Rydberg state and hence also the strength of interaction effects. In order to maximize interaction effects we chose $\omega > \Omega$ in the CPT experiments. However, when $\omega \ll \Omega$ is not fulfilled the concept of DSP is not fully applicable. In this case the basic mechanism can still be understood in the framework of a two-atom picture.

A system of two non-interacting atoms has a dark state which is the product state $|d\rangle \otimes |d\rangle$ of two single-atom dark states $|d\rangle$ as given in eq. 3.7. For interacting atoms, however, this product state is no longer a dark state, since it is not an eigenstate of the Hamiltonian. [Møller *et al.*, 2008] pointed out that the interacting two-atom system has instead two dark states $|d_\pm\rangle$. These dark states have an admixture of the intermediate state $|2\rangle$ and are thus subject to decay. On the other hand they are significantly populated due to optical pumping, therefore leading to a resonance in the spectrum. This resonance is unshifted since the states $|d_\pm\rangle$ have no contribution from the doubly excited state $|rr\rangle$. This picture can be qualitatively extended to more than two atoms, since also for more atoms only states involving at most one Rydberg excitation can be populated when using resonant light. Hence the relative height of the CPT resonance decreases with increasing density. Eventually both

the polariton as well as the two-atom picture reflect the fact that within a certain volume there can be only one excitation, or, in a photon picture, only a limited amount of photons can be transformed into atomic excitations.

3.2.1 Coherent population trapping with controlled interparticle interactions

The experiments on CPT involving interaction Rydberg states were carried out on an earlier experimental apparatus at the University of Freiburg, which was in many respects similar to the new apparatus constructed during this thesis (Ch. 2.3). Details on the Freiburg apparatus can e.g. be found in [Amthor, 2008]. Since it did not feature an optical dipole trap the experiments were performed in a MOT at atomic densities of up to $6.6 \times 10^9\,\mathrm{cm}^{-3}$.

To investigate how interactions between Rydberg states affect CPT we apply a double pulse excitation scheme where the first pulse resonantly excites up to 20 % of the ground state atoms to the Rydberg state. The resulting well-defined mixture of atoms in the ground state and Rydberg state is then probed by scanning the blue laser frequency of the second pulse. This initial partial excitation of the gas permits off-resonant excitation of strongly interacting atom pairs [Reinhard *et al.*, 2008a] during the second pulse, such that interaction effects are more pronounced. The first excitation pulse with a duration of 800 ns is realized by two circularly polarized counter-propagating laser beams, resonant with the respective transitions with peak Rabi frequencies of $\omega = 2\pi \times 7.6\,\mathrm{MHz}$ and $\Omega = 2\pi \times 1.4\,\mathrm{MHz}$, respectively. The lower (red) excitation beam has a large beam radius ($\approx 1\,\mathrm{mm}$), while the upper (blue) beam is focused to a waist of $\approx 37\,\mu\mathrm{m}$. The red Rabi frequency can thus be considered to be constant over the narrow cylindrical excitation volume, while the blue Rabi frequency varies radially. After the first excitation pulse a second pair of laser pulses having the same beam geometry, but independently adjustable Rabi frequencies, probes the system with a pulse duration of $3\,\mu\mathrm{s}$. While the lower laser transition is kept resonant ($\omega = 2\pi \times 2.7\,\mathrm{MHz}$), the upper probe transition is scanned over the atomic resonance with a Rabi frequency of $\Omega = 2\pi \times 1.4\,\mathrm{MHz}$. For the given parameters, on resonance the system is found close to the steady state after the probe pulse. A similar Rydberg excitation sequence has been employed in [Reinhard *et al.*, 2008a] to probe energy shifts in a very dense sample with a detuned second excitation pulse. In contrast to our experiment, much shorter pulses were employed leading to a system far away from the steady-state.

As a signature of interparticle interactions, the excitation blockade due to repul-

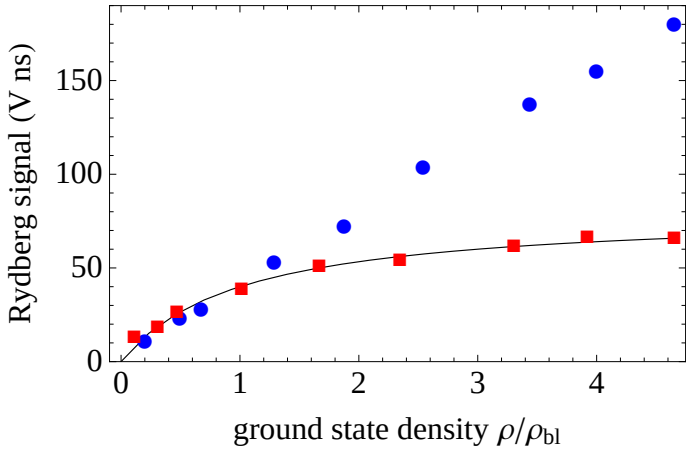

Figure 3.4: Rydberg excitation vs. ground state atom density ρ after the first (resonant) excitation pulse. The blue dots are the data obtained from the excitation of $30S$ states which does not feature any interaction effects at our densities, while the excitation of $61S$ atoms (red squares) shows a clear saturation of excitation at higher densities due to the dipole blockade. The $61S$ data is fitted with the saturation function $\sim 1/(1+\rho_{bl}/\rho)$ which yields a density of $\rho_{bl} = 1.3 \times 10^9\,\mathrm{cm}^{-3}$ at which blockade effects become apparent.

sive van der Waals interactions is presented in fig. 3.4. We measure the Rydberg signal as a function of the ground state density for the states $30S$ and $61S$. When exciting $61S$ atoms we find a saturation of the Rydberg signal due to the interactions as discussed in Ch. 2.1. There is no excitation blockade observed for the $30S$ state reflecting the n^{11} dependence of the van der Waals interaction on the principal quantum number n [Singer *et al.*, 2005].

The corresponding CPT spectrum for the $30S$ state is shown in fig. 3.5(a). At large detunings we find a finite Rydberg population which is created during the 800 ns pre-excitation pulse. Closer to resonance we find the Rydberg atoms to be deexcited to the intermediate state, thereby reducing the signal. For $\delta = 0$ we find a peak in the Rydberg signal which is due to the dark resonance. The observed CPT resonance can be well described in terms of single-particle Optical Bloch Equations (OBEs) averaged over the Gaussian distribution of the Rabi frequency Ω. The finite laser linewidth and redistribution of Rydberg states by blackbody radiation have been included as additional decay processes. Consistency of measurements with the prediction of the OBEs was confirmed for various pulse sequences and Rabi frequencies. Besides a scaling of the whole spectrum proportional to the density we do not find any density dependent features in the spectra. In the regime of

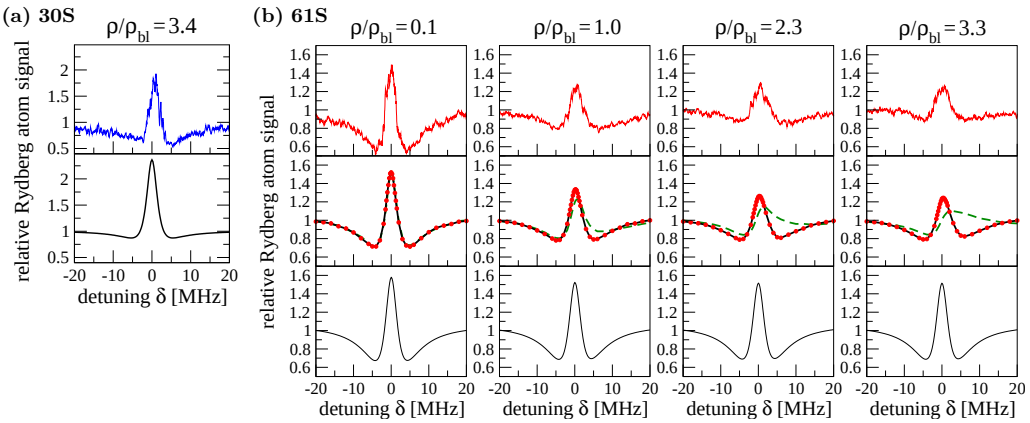

Figure 3.5: (a) Probe scan of the $30S$ Rydberg state (upper graph) and simulation using one-atom optical Bloch equations (lower graph), averaged over the Gaussian distribution of Ω. The $30S$ state is subject to stronger decay and redistribution than the $61S$ state, which is why the dip in the signal around the central peak is less pronounced. (b) Upper graphs: Similar scans for the $61S$ Rydberg state at different densities. Middle graphs: Theoretical spectra, obtained from the density matrix expansion (red dots) and from the mean-field calculation (green dashed lines). Lower graphs: Theoretical spectra considering only interacting pairs. All calculations have been performed using the experimental parameters. Densities are given relative to $\rho_{bl} = 1.3 \times 10^9\,\mathrm{cm}^{-3}$ as obtained from fig. 3.4.

strong Rydberg–Rydberg interactions (61S state with a van der Waals coefficient $C_6 = 2\pi \times 170\,\mathrm{GHz}\,\mu\mathrm{m}^6$ [Singer *et al.*, 2005]), as shown in fig. 3.5(b) the CPT spectra still exhibit a pronounced peak with sub-natural linewidth at zero detuning at all densities. The CPT resonance width of $\approx 3\,\mathrm{MHz}$ (which only slightly increases with density) is well below the natural linewidth of the intermediate state $|2\rangle$ of 6.1 MHz and mainly determined by the finite laser linewidths.

The experimental data can be well reproduced by many-body calculations based on density matrix expansion which were performed at the Max-Planck Institut for the Physics of Complex Systems in Dresden [Schempp *et al.*, 2010; Sevinçli *et al.*, 2011a]. This approach starts from the OBEs (eq. 3.12), but adds a term to account for two-atom correlations. Approximating this term by its expectation value corresponds to a meanfield model which does not reproduce our experimental data. Instead the equations of motion for the two-atom density matrix have to be solved (81 equations). These in turn contain three-atom correlations, which have to be obtained from the three-atom OBEs. As a result we obtain a hierarchy of coupled equations. Since the N-body density matrix can usually not be calculated, this hi-

erarchy has to be truncated in an appropriate way. To reproduce our experimental data three-body correlations were approximated but had to be taken into account. The result is shown in the second row of fig. 3.5. In contrast, when treating only pairs of atoms and averaging over the distribution of nearest neighbors, we cannot reproduce the suppression of the CPT resonance as observed in the experimental data (see third row in fig. 3.5). The described approach is an expansion in density, therefore it is of course not applicable to arbitrarily high densities, since every higher order correlations drastically increase the computational effort.

3.2.2 Interacting dark-state polaritons: nonlinear optical susceptibility

To observe the effect of interacting DSPs on the optical response of a medium we recorded the transmission through an atomic cloud for various densities and different probe field intensities. To this end we prepared an elongated cloud of 10^5 atoms at a temperature of $5\,\mu$K and a peak density of $\approx 3 \times 10^{12}\,\mathrm{cm}^{-3}$ in the optical dipole trap. Varying the time-of-flight, i.e. the time between releasing the atoms from the trap and performing the actual experiment, from $20\,\mu$s to 4.5 ms, we realize atomic densities ranging from $\approx 10^9 - 3 \times 10^{12}\,\mathrm{cm}^{-3}$. We work with the Rydberg state $55S$ which features repulsive van der Waals interactions with a C_6 coefficient of $2\pi \times 50\,\mathrm{GHz}\,\mu\mathrm{m}^6$. We use a diffractive optical element to create an approximately uniform distribution of the coupling laser beam in an elliptical region of size $\approx 65\mu\mathrm{m}\times 130\mu\mathrm{m}$. The strength of the coupling field is $\Omega = 2\pi \times 5.1\,\mathrm{MHz}$. The shape as well as the strength of the coupling field are determined by frequency scans and subsequent analysis of the resulting EIT spectrum for each single pixel. The details of this procedure are described in [Hofmann *et al.*, 2014]. The probe field illuminates the whole cloud homogeneously with intensities of $5\,\mu\mathrm{W/cm}^2$ or $62\,\mu\mathrm{W/cm}^2$. Both beams are tuned to the respective resonance frequencies and turned on for $100\,\mu$s. The probe light is collected on a CCD camera and yields an absorption image of the atomic cloud, which in addition features a transparent spot at the position where it is hit by the focused coupling beam (see fig. 3.6). The transparency is well pronounced at low atomic densities and is reduced at higher densities. In contrast to previous work [Pritchard *et al.*, 2010] we explore the full range from an almost transparent to a completely absorbing medium.

In order to analyze our findings more quantitatively we plot the scaled absorption, i.e. the ratio of the actual absorption of the cloud at the position of the coupling laser beam and the absorption that would be measured in the absence of the coupling

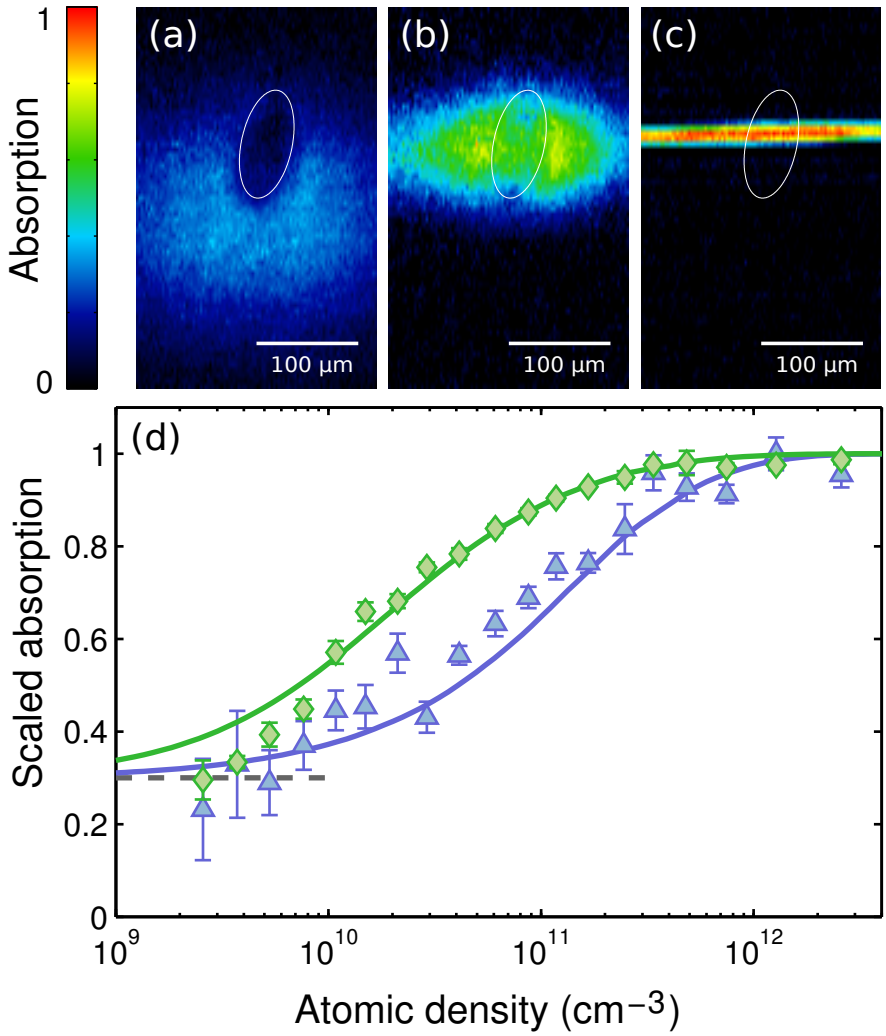

Figure 3.6: Nonlinear optical response of the Rydberg EIT medium. Top: Absorption images of the atomic cloud for three expansion times with peak densities corresponding to $5 \times 10^9\,\mathrm{cm}^{-3}$, $5 \times 10^{10}\,\mathrm{cm}^{-3}$ and $3 \times 10^{12}\,\mathrm{cm}^{-3}$ (left to right). The EIT region illuminated by the coupling laser is indicated by white ellipses. Bottom: Absorption scaled to the two-level response as a function of peak atomic density. The two curves are taken at probe field intensities of $5\,\mu\mathrm{W/cm}^2$ (blue triangles) and $62\,\mu\mathrm{W/cm}^2$ (green diamonds). The dotted horizontal line shows the expected low-density EIT absorption due to the finite laser linewidths. The solid lines are a fit to the data using a hard-sphere model with the critical DSP density ρ_c as the only free parameter for both curves.

field. The result is shown in fig. 3.6. For low densities where interactions are not yet expected to play a role we find the scaled absorption around 0.3. Considering our laser parameters we do not expect the transparency to be perfect but we estimate

a finite scaled absorption of 0.3±0.1 (indicated as dashed horizontal line) even for a non-interacting system. Higher atomic densities come along with a larger group index, hence the DSPs move more slowly and prevent the conversion of subsequent photons into DSPs for a longer time. As a consequence the photons arriving during this time are scattered, thereby reducing the transparency of the cloud. At the highest densities the ratio between photons traveling through the cloud as DSPs and photons being scattered is so small that the cloud seems fully absorptive. As expected from the discussion in Ch. 3.2 the suppression of transparency sets in earlier for higher probe field intensities (green diamonds in fig. 3.6).

The characteristic behavior of the scaled absorption has been predicted in [Ates *et al.*, 2011] where it was obtained from a rate equation model. However, a simpler model in the framework of interacting DSPs describes this characteristic behavior equally well. Once the photons enter the atomic cloud they can be treated as two components, i.e. a fraction of the photons is converted into DSPs which propagate under EIT conditions while each DSP fills a hard sphere volume given by the blockade radius $r_{bl} = (C_6 2\Gamma_e/\Omega^2)^{1/6}$. In contrast, the remaining photons experience a two-level response and are thus scattered. The results of this hard sphere model are plotted as solid lines in fig. 3.6 where the only free parameter for both curves is the critical density of DSPs, ρ_c, at which the DSPs start to be densely packed. More details on this model can be found in [Günter, 2013]. A more rigourous semi-analytical model for the non-linear light propagation in Rydberg interacting systems has been published this year [Gärttner *et al.*, 2014].

3.2.3 Probing the matter part of dark-state polaritons

As mentioned above correlations between DSPs have been recently observed as an anti-bunching of the transmitted probe photons. The measurement of these photons is one way to detect individual DSPs. Alternatively, as the DSPs have a large matter component inside the cloud (typically $\cos^2(\theta) \approx 10^{-3}$ to 10^{-7} for our experimental conditions), we show for the first time detection of Rydberg DSPs via their atomic component. Due to the mixing angle the number of Rydberg excitations is a very good measure for the number of DSPs inside the medium. Single Rydberg excitations can be sensitively detected in our experiments, thereby providing a way to measure single DSPs. To demonstrate this we first map out the coherent conversion from photons into matter-like DSPs and back in a system where interactions can be neglected. To this end we prepare a dilute cloud which we expose to a probe field pulse of 2.2 μs duration. By varying the time at which we field ionize the Rydberg

atoms we obtain the temporal evolution of the number of DSPs inside the medium which is shown in fig. 3.7. At time $t = 0$ the probe field pulse enters the atomic cloud, resulting in the creation of matter-like DSPs. While the pulse is inside the cloud we detect on average 10 ions. Taking our detection efficiency of ≈0.4 into account this corresponds to approximately 25 DSPs being inside the cloud at the same time. Once the probe field pulse leaves the atomic cloud the number of DSPs rapidly decreases due to their coherent transformation into photons.

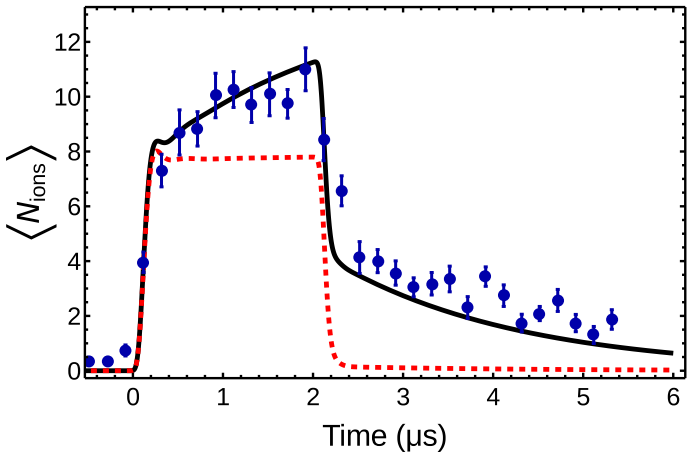

Figure 3.7: Coherent conversion of probe field photons into DSPs and back at low density (no interactions). For this measurement the coupling field was constantly on, while the probe field was switched on only for 2.2 μs, starting at $t = 0$. We vary the time at which the ionization fields were switched on, thereby obtaining a measure for the current number of DSPs (corresponding to the number of Rydberg excitations) inside the atomic cloud. Since the probe field photons are converted into DSPs when entering the cloud we measure always a finite number of DSPs while the probe field pulse is on. When exciting the atomic cloud these DSPs are coherently converted back into photons. Therefore once the probe field pulse is off we do not detect any more excitations after the remaining DSPs have left the cloud. The deviation from a perfectly square pulse (red dashed line) is due to a weak off-resonant coupling to a second Zeeman state.

The deviations from a square pulse (red dashed line in fig. 3.7), which would be expected for a square probe field pulse, can be explained by a weak coupling to a fourth state. The Rydberg state $55S_{1/2}$ has two Zeeman sublevels of which we adress one by choosing a particular polarization of the excitation laser. However, due to this polarization not being perfect we still couple weakly to the other Zeeman state. Including this fourth state in the OBEs and solving for the overall Rydberg state population reproduces the experimental findings (black line in fig. 3.7), which

show some additional dynamics, namely a slow increase of the Rydberg population during the probe field pulse and a slow decrease after the pulse. Note that under the conditions discussed here the group index of the medium does not differ significantly from 1. Once the group index would be significantly larger, i.e. the group velocity significantly slower than the speed of light, the polariton pulse shown in fig. 3.7 would be longer than the probe field pulse.

3.2.4 Counting statistics of interacting dark-state polaritons

As shown in Ch. 3.2.3 we are able to count single DSPs by counting the field ionized Rydberg excitations. In the interacting regime we expect the DSPs to exhibit spatial and temporal correlations, as discussed in Ch. 3.2 and sketched in fig. 3.3. In order to reveal these correlations in our experiments we study the counting statistics of DSPs.

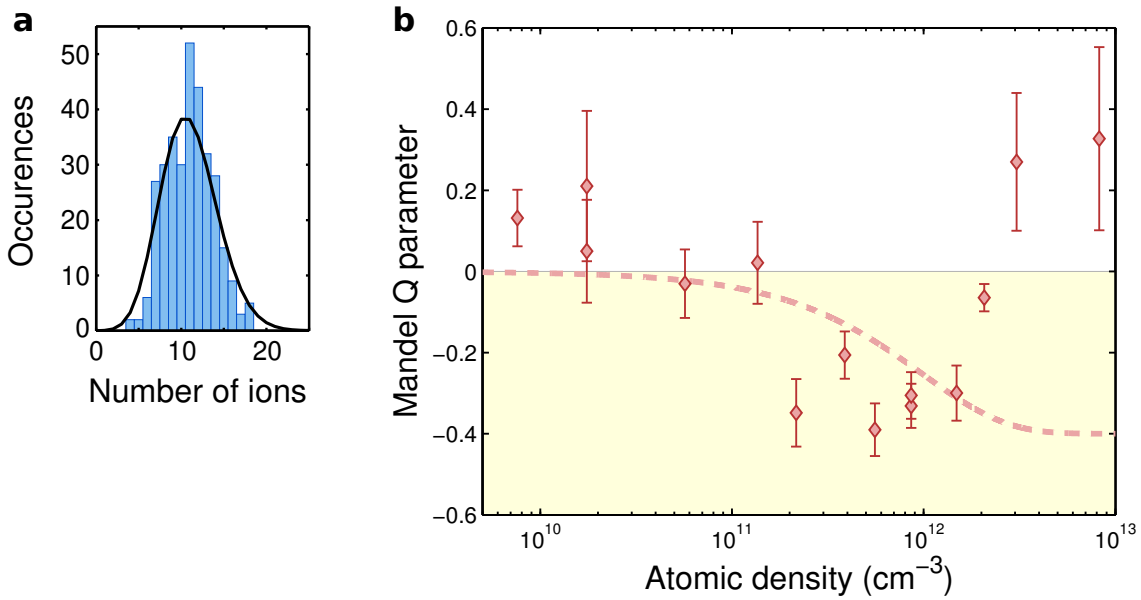

Figure 3.8: a) Histogram of the measured number of DSPs in the interacting regime. The solid black curve shows a Poissonian distribution for comparison. b) Mandel Q-parameter as a function of atomic density. Starting from Poissonian behavior (Q=0) at low densities we find Q decreasing at higher densities, reflecting correlations between polaritons. Considering our detection efficiency of $\eta \simeq 0.4$ the smallest measured values of $Q \approx -0.4$ are compatible with dense packing of DSPs, i.e. no fluctuation in the number of DSPs. At the highest densities processes as spontaneous plasma formation lead to additional fluctuations and thus to $Q > 0$. The dashed line shows the result of the hard sphere model which predicts $Q = e^{\rho/\rho_{crit}} - 1$ with the critical density ρ_{crit}.

It has been observed before that the dipole blockade in Rydberg systems leads to a suppression of number fluctuations [Reinhard *et al.*, 2008b; Viteau *et al.*, 2011; Viteau *et al.*, 2012]. Here we study the counting statistics of DSPs as a function of the atomic density. The number of DSPs is counted after a probe pulse of $2\,\mu$s and for each setting the experiment is repeated 150-300 times, yielding histograms as shown in fig. 3.8 a). We quantify the number fluctuations using the Mandel Q parameter

$$Q = \frac{(N - \langle N \rangle)^2}{\langle N \rangle} - 1 \tag{3.23}$$

which relates the variance of the measured distribution to its mean. Fig. 3.8 b) shows the measured Q parameters as a function of the atomic density. In the low density regime where all photons are converted into DSPs the number statistics of the DSPs reflects the statistics of the incoming probe field photons, which for classical fields is a Poissonian distribution. For a Poissonian distribution $(N-\langle N \rangle)^2 = \langle N \rangle$, therefore we expect $Q = 0$ which is compatible with our experimental results at low densities. At higher densities we find Q to decrease down to values of $Q \approx -0.4$.

When the DSPs are densely packed inside the atomic cloud we expect vanishing number fluctuations, i.e. $(N-\langle N \rangle)^2 = 0$ and hence $Q = -1$. However, in an experiment with a finite detection efficiency the number fluctuations never vanish since the stochastic detection process itself leads to additional fluctuations. Convolving the actual distribution with a binomial distribution therefore yields the measured distribution. As a consequence the measured Mandel parameter Q_{exp} is reduced by the detection efficiency η as compared to the real value Q_{real}: $Q_{exp} = \eta Q_{real}$. Our measured Q values of ≈ -0.4 at intermediate densities are thus compatible with $Q_{real} = -1$, indicating dense packing of DSPs. At the highest densities we find positive Q parameters which cannot be interpreted in the picture of interacting DSPs. Instead additional processes as e.g. spontaneous plasma formation, which we found to set in very quickly at high densities [Robert-de-Saint-Vincent *et al.*, 2013], are probably the reason for these increased number fluctuations.

3.3 Prospects

As mentioned above non-classical light fields caused by Rydberg interactions have recently been observed, featuring either anti-bunching [Peyronel *et al.*, 2012] or bunching [Firstenberg *et al.*, 2013] in the outgoing photon field. The above mentioned work has investigated temporal photon correlations, however, the bunching and anti-bunching should also be present in the spatial photon correlations. These

can in the future be resolved using the electron multiplying (EM) mode of a CCD camera as it is available at our experiment. Together with the improved optical resolution as achieved in a Master thesis [Helmrich, 2013] this brings the investigation of spatial photon correlations within reach. In addition it allows to investigate non-local non-linear interactions [Sevinçli *et al.*, 2011b] and Wigner crystals of photons [Otterbach *et al.*, 2013]. Both studies require elastic effective photon interactions which can be realized by detuning from the intermediate state thus reducing photon scattering. Our well-established ion detection featuring single particle sensitivity furthermore allows to gain more insight into the coupled atom-light system by combining the measurements of the atomic and the photonic correlations, which are non-trivially connected. Atomic correlations, e.g., do not necessarily imply photonic correlations, but the latter in addition require the optical depth of a blockade sphere to be large.

Chapter 4

Full counting statistics of Rydberg aggregates in a one-dimensional geometry

This chapter is based on the following publication:

Full counting statistics of laser excited Rydberg aggregates in a one-dimensional geometry
H. Schempp, G. Günter, M. Robert-de-Saint-Vincent, C. S. Hofmann, D. Breyel, A. Komnik, D. Schönleber, M. Gärttner, J. Evers, S. Whitlock, M. Weidemüller
Phys. Rev. Lett **112**, 013002 (2014)

As an alternative to direct imaging of Rydberg excitations the full counting statistics (FCS) of these systems provides a complementary approach to gain insight into the underlying many-body state. This approach is widely used in solid states physics where e.g. the counting statistics of electrons allows to reveal the nature of transport processes through nano-structures [Nazarov and Blanter, 2009]. Similarly the Rydberg atom number fluctuations reveal information about the nature of the excitation processes involved. As already discussed in Ch. 3 the independent excitation of non-interacting Rydberg atoms results in Poissonian number fluctuations, while a dipole blockaded system exhibits reduced number fluctuations. The deterministic preparation of a quantum crystal as proposed in [Pohl *et al.*, 2010], would even be characterized by the absence of any fluctuations. In this chapter we study a system which, in contrast to the reduced number fluctuations reported in [Reinhard *et al.*, 2008b; Viteau *et al.*, 2011; Hofmann *et al.*, 2013b; Viteau *et al.*, 2012], features *enhanced* number fluctuations. To be specific, we study the full counting statistics of

Rydberg excitations in a one-dimensional geometry. For positive detunings we find correlated structures comprised of several Rydberg excitations which in the following we call Rydberg aggregates. Evidence of aggregate formation is in the strongly enhanced excitation probabilities on the blue side of the resonance. The resulting asymmetric excitation spectra are discussed in Ch. 4.2. In Ch. 4.3 we discuss the enhanced number fluctuations which we find on the blue side of the resonance and which we attribute to Rydberg aggregate formation. The behavior of higher order moments is discussed in Ch. 4.4. Estimating rates for different excitation processes (Ch. 4.5.1) and comparing our experimental findings with different theoretical models (Ch. 4.5.2), we conclude on the formation process of the Rydberg aggregates.

The experiments are performed in an elongated atomic cloud which we realize by loading atoms from the MOT into the tightly focused optical dipole trap beam (dimple). The atoms thermalize in the trap for 400 ms before a microwave sweep prepares up to $\approx 2 \times 10^4$ atoms in the state $|5S_{1/2}, F = 2, m_F = 2\rangle$. Due to our finite optical resolution, the radial size of the cloud cannot be precisely measured. Therefore we adjust this parameter by comparison with theory (see Ch. 4.5). From this comparison we deduce a radial size of $\approx$1.65 μm ($1/e^2$ radius) which is within our estimates, where the lower bound of 1 μm is estimated from the trap beam parameters and the temperature while the upper bound of 3.5μm is directly extracted from absorption images. We realize different atomic densities by varying the loading time of the MOT with the highest densities being $\approx 1.5 \times 10^{12}\text{cm}^{-3}$.

After releasing the atoms from the trap we perform a detuned two-photon excitation to a Rydberg state. The first photon is red detuned by $\delta = 65\,\text{MHz}$ from the intermediate state $|5P_{3/2}, F = 3, m_F = 3\rangle$ while the second photon can be tuned such that the two-photon detuning Δ covers a range from -10 MHz to +25 MHz. Working at Rabi frequencies of $\omega_1 = 2\pi \times 8\,\text{MHz}$ (lower transition) and $\omega_2 = 2\pi \times 6.7\,\text{MHz}$ (upper transition, peak value) we realize an effective peak Rabi frequency of $\Omega = \omega_1\omega_2/(2\delta) = 2\pi \times 0.4\,\text{MHz}$ on two-photon resonance with a combined dephasing rate of $\approx 1\,\text{MHz}$. Directly after the excitation pulse of 5 μs duration we field ionize the Rydberg atoms and detect the resulting ions on a microchannel plate detector (MCP). We work with the Rydberg state 50S which features a repulsive van der Waals interaction of strength $C_6 = 2\pi \times 16\,\text{GHz}\mu\text{m}^6$ [Singer *et al.*, 2005]. The resulting blockade radius is larger than our cloud size, hence the cloud is quasi one-dimensional with respect to Rydberg excitation.

4.1 Detection and statistical analysis

In order to investigate the number statistics of Rydberg aggregates we repeat the experimental procedure described above up to 800 times under the same conditions. Working at low overall excitation numbers we can count the Rydberg atoms as single peaks in the MCP trace. Fig. 4.1 shows histograms of the measured Rydberg atom number distribution for three different detunings Δ and 800 repetitions of the same experiment each. From these histograms we can extract the mean Rydberg atom number as well as higher order moments.

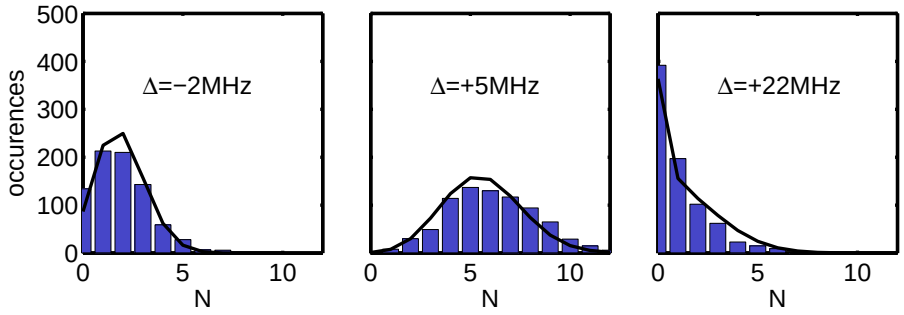

Figure 4.1: Measured histograms of the Rydberg atom number distribution for different detunings. The solid lines are the results of the numerical simulations described in Ch. 4.5.

While it is straightforward to specify an uncertainty on the mean of a statistical distribution in terms of a confidence interval, the uncertainties on any other estimator of the distribution, like e.g. the variance, cannot be directly obtained from a single histogram. For this reason we make use of bootstrapping [Efron, 1979] in order to extract uncertainties for the statistical measures we want to investigate. Bootstrapping is a so-called re-sampling technique where the actually measured distribution forms a reservoir from which other distributions are constructed. If e.g. the measured distribution $P(l)$ has a sample size k, the new distributions have the same size and are constructed by sampling with replacements from the measured distribution $P(l)$. From each of these re-sampled distributions the estimator of interest can be extracted, resulting in a distribution of values for this estimator. From this distribution it is again straightforward to specify a confidence interval for the estimator of interest. Note that depending on the respective estimator and the original sample size the number of required re-sampled distributions can strongly vary. For this reason we made sure that the amount of re-sampled distributions is large enough for the confidence interval of the respective estimator to have converged.

4.2 Asymmetric excitation spectra

As the most trivial estimator we first extract the mean of the measured Rydberg atom number distributions in order to obtain excitation spectra at different atomic densities ranging from $5 \times 10^{10}\,\mathrm{cm}^{-3}$ to $1.5 \times 10^{12}\,\mathrm{cm}^{-3}$ (see Fig. 4.2). While for low atomic densities the spectra are symmetric there is an asymmetry building up at higher densities reflecting enhanced excitation probabilities for positive laser detunings. This fact can be understood from the sign of the Rydberg interaction. Since the energy of a pair of Rydberg atoms at a small separation is enhanced as compared to the energy of two independent Rydberg atoms the excitation requires a larger frequency.

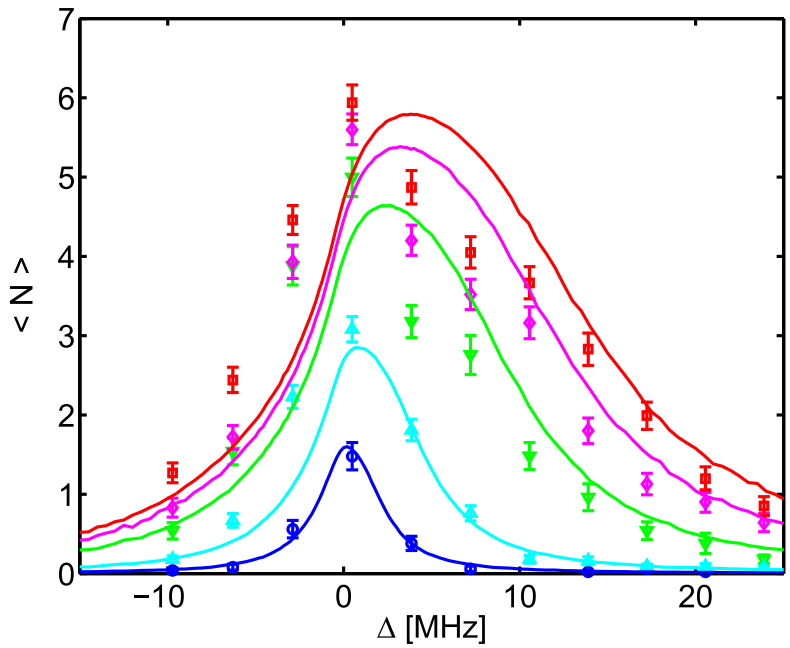

Figure 4.2: Excitation spectra for different atomic densities: $5 \times 10^{10}\,\mathrm{cm}^{-3}$ (blue circles), $2 \times 10^{11}\,\mathrm{cm}^{-3}$ (cyan triangles), $8 \times 10^{11}\,\mathrm{cm}^{-3}$ (green triangles), $1.3 \times 10^{12}\,\mathrm{cm}^{-3}$ (magenta diamonds) and $1.5 \times 10^{12}\,\mathrm{cm}^{-3}$ (red squares). With increasing density we find enhanced excitation probabilities on the blue side of the resonance due to repulsive Rydberg-Rydberg interactions. The solid lines show the result of the rate equation model.

For atoms arranged on a lattice with lattice constant d two neighboring atoms have a well-defined interaction energy $E = C_6/d^6$. In this configuration the excitation of a pair could either happen as a resonant simultaneous 2-photon process which

would require the detuning Δ to fulfill $2\Delta = E$. Alternatively the first atom could be off-resonantly excited, followed by a resonant excitation of its neighbor. This process would require $\Delta = E$ for the second excitation step to be resonant. The question which of these processes is the dominant one will be discussed in Ch. 4.5.

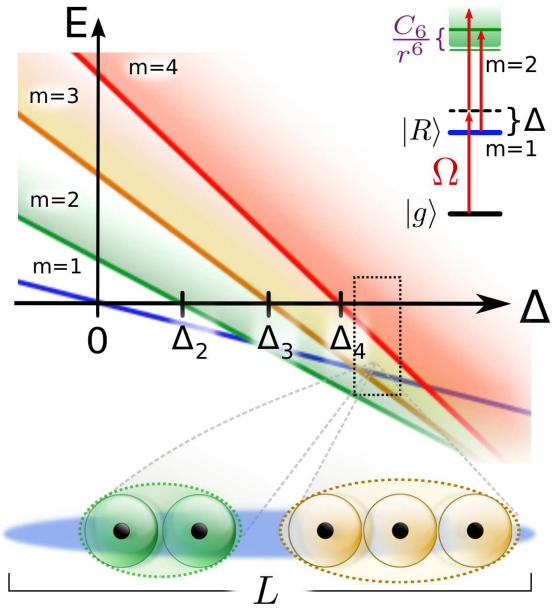

Figure 4.3: Many-body energies in a rotating frame for Rydberg aggregates of size m as a function of laser detuning Δ. The shaded areas indicate the manifold of excited states corresponding to different spatial configurations. Zero energy crossings for the lowest energy states occur at $\Delta_m = C_6(m-1)^7/(mL^6)$ where L is the system length and C_6 is the van der Waals interaction strength. For a given detuning and laser dephasing, aggregates of different sizes can be formed (dotted rectangle), either through sequential growth or by multi-photon excitation.

Our experiments were performed in a disordered gas, hence the required laser frequencies as discussed above are not sharp, because E depends on the interatomic separation. In addition, correlated structures comprised of more than two atoms, which in the following we are going to refer to as aggregates, can also be excited. Fig. 4.3 shows the many-body energies in a rotating frame for Rydberg aggregates of size m as a function of laser detuning Δ. The minimum energy of an aggregate in a system of finite size L is realized when the excitations are arranged at maximum separation from each other. This minimum energy is indicated by the solid lines, whereas the shaded areas above these lines indicate the manifold of possible aggregate energies which correspond to spatial configurations involving smaller distances

between excitations. Thus the aggregates can not only be created by different mechanisms requiring different excitation frequencies, but aggregates of different size can have the same interaction energy and hence be excited at the same laser detuning. As a consequence we can not identify the excitation of aggregates of a certain size as sharp lines in the spectra shown in fig. 4.2. We rather see an enhanced excitation probability for all $\Delta > 0$, leading to an asymmetric excitation spectrum, where any structure is washed out due to the random spatial distribution of atoms as well as the different excitation mechanisms. The observed asymmetry in the spectra gets more pronounced at higher densities since here the pair distances required for aggregate formation are more likely to be available.

4.3 Enhanced number fluctuations

The excitation spectrum, i.e. the mean detected Rydberg atom number, hints already at processes beyond the excitation of independent atoms. As discussed above the enhanced excitation probability for positive detunings is due to the excitation of aggregates of Rydberg atoms whose interaction energy increases the energy required for excitation. Further insight into the underlying many-body system can be obtained by analyzing higher order statistical moments of the measured distribution. As demonstrated by [Reinhard *et al.*, 2008b; Viteau *et al.*, 2011; Hofmann *et al.*, 2013b; Viteau *et al.*, 2012] the dipole blockade results in reduced Rydberg atom number fluctuations for resonant excitation since due to the interactions each Rydberg atom blocks a certain volume. A dense packing of these blockade spheres therefore sets an upper limit on the Rydberg atom number, hence suppressing number fluctuations.

The Mandel Q-factor $Q = \frac{\langle (N-\langle N\rangle)^2\rangle}{\langle N\rangle} - 1$ as already introduced in Ch. 3.2.4 relates the second statistical moment of a distribution to its mean, thereby providing a comparison with a Poissonian distribution where $Q = 0$. Measuring Q as a function of the detuning at a density of $1.5 \times 10^{12}\,\mathrm{cm}^{-3}$ we find the behavior shown in Fig. 4.4. On the red side of the resonance, i.e. for $\Delta < 0$ we measure Q-factors around 0 indicating independent excitation of Rydberg atoms. Around resonance we find negative Q-factors which is in agreement with earlier measurements mentioned above ([Reinhard *et al.*, 2008b; Viteau *et al.*, 2011; Hofmann *et al.*, 2013b; Viteau *et al.*, 2012]). In contrast, for $\Delta > 0$ we find Q positive and increasing with Δ. A qualitatively similar behavior has been predicted in [Gärttner *et al.*, 2013] based on numerical simulations. We attribute this behavior to the formation of Rydberg

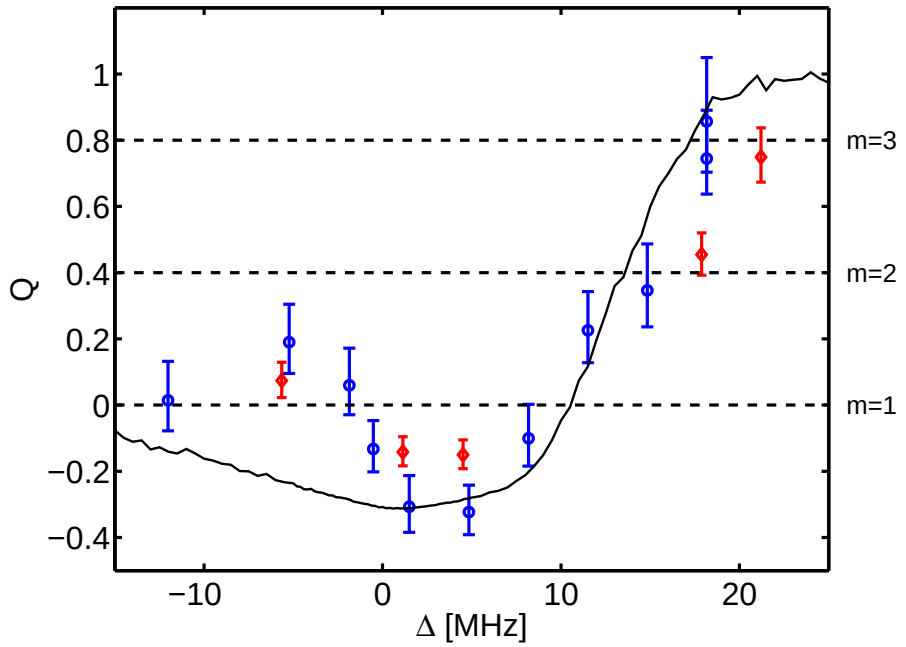

Figure 4.4: Mandel Q factors of the distributions as a function of the detuning Δ of the excitation lasers at a density of $1.5 \times 10^{12}\,\mathrm{cm}^{-3}$. The red diamonds (blue circles) are extracted from a dataset with 200 (800) experiments per data point. Error bars represent 68% confidence intervals determined via bootstrapping. The dashed lines indicate the expected Q factors corresponding to the excitation of exclusively single atoms, pairs and triples. The solid lines show the statistical moments as obtained from the rate equation model described in Ch. 4.5.2.

aggregates of increasing size.

In order to get an intuition how the counting statistics of Rydberg aggregates are changed as compared to independently excited atoms, we assume for simplicity to exclusively excite Rydberg aggregates of size m. The number of Rydberg aggregates K follows a distribution $P(K)$ which we assume to be Poissonian, i.e. we assume the aggregates to be excited independently. This assumption is justified for low overall excitation numbers i.e. a system far from saturation. The mean overall Rydberg excitation number is hence $\langle N \rangle = m\langle K \rangle$ and the p-th central moment (defined for a distribution $P(L)$ as $\mu_{L,p} = \langle (L - \langle L \rangle)^p \rangle$) of the distribution $P(N)$ results in

$$\mu_{N,p} = \langle (mK - \langle mK \rangle)^p \rangle = m^p \langle (K - \langle K \rangle)^p \rangle \tag{4.1}$$

Using the expressions above we find for the Q-factor resulting from independent

excitation of aggregates of size m

$$Q = \frac{m^2\langle(K - \langle K\rangle)^2\rangle}{m\langle K\rangle} - 1 = m - 1 \tag{4.2}$$

since for a Poissonian distribution $\langle(K - \langle K\rangle)^2\rangle = \langle K\rangle$. This means that from the measured Q it is possible to extract a typical aggregate size. To be more specific, whenever $Q > m$ there is on average at least one aggregate of size $m + 1$.

In order to compare the calculated Q-factors with measured quantities we have to account for the finite detection efficiency $\eta \approx 0.4$ as already discussed in Ch. 3, i.e. for the measured Q-factor as plotted in Fig. 4.4 we expect $\eta(m - 1)$. From the measured Q-factors and the respective thresholds shown in Fig. 4.4 we conclude that at our largest detunings of ≈20 MHz we excite aggregates of typical size $m = 3$ and that the presence of even larger aggregates is very likely. Recently, similar findings on the Δ-dependence of the Q parameter have been reported in [Malossi *et al.*, 2013].

4.4 Higher order statistical moments

Following the reasoning above we can deduce what to expect for higher order statistical moments of the measured Rydberg atom number distribution. As a measure for the third statistical moment we define

$$Q_3 = \frac{\langle(N - \langle N\rangle)^3\rangle}{\langle N\rangle} - 1 \tag{4.3}$$

in analogy to the Mandel Q-factor. As can be seen from eq. 4.1 Q_3 scales as

$$Q_3 = \frac{m^3\langle(K - \langle K\rangle)^3\rangle}{m\langle K\rangle} - 1 = m^2 - 1 \tag{4.4}$$

with the aggregate size m since for a Poissonian distribution $\langle(K - \langle K\rangle)^3 = \langle(K - \langle K\rangle)^2 = \langle K\rangle$. As in the case of the Mandel parameter Q the finite detection efficiency also affects Q_3 such that the measured quantity is

$$Q_3' = 3Q(\eta - \eta^2) + Q_3\eta^2 \tag{4.5}$$

(see Supplemental Material of [Schempp *et al.*, 2014]).

Figure 4.5 shows the measured Q_3 as a function of detuning together with the respective thresholds for the excitation of aggregates with $m = 2$ and $m = 3$. Similar to our findings in Q we find $Q_3 \approx 0$ for negative detunings indicating Poissonian statistics due to independent excitation. The measured Q_3 at large positive detunings implies a typical aggregate size of $m = 3$ and hence confirms our conclusion

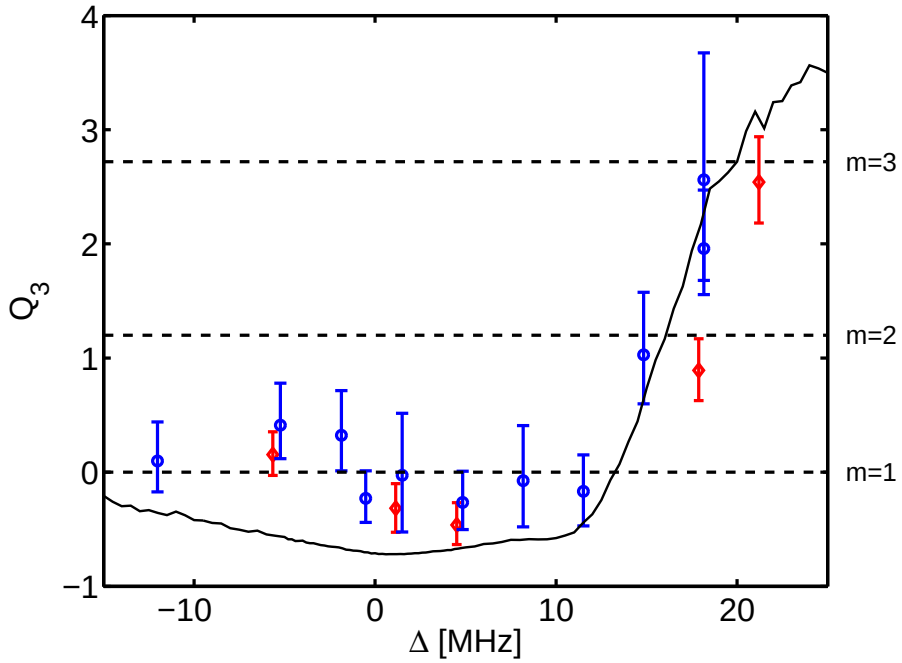

Figure 4.5: $Q_3 = \frac{\langle (N-\langle N\rangle)^3\rangle}{\langle N\rangle} - 1$ as a function of the laser detuning Δ at a density of $1.5 \times 10^{12}\text{cm}^{-3}$. The red diamonds (blue circles) are extracted from a dataset with 200 (800) experiments per data point. The dashed lines indicate the expected Q_3 corresponding to the excitation of exclusively single atoms, pairs and triples as given in eq. 4.5. The solid lines show the statistical moments as obtained from the rate equation model described in Ch. 4.5.2.

from the analysis of Q. Due to the limited sample size of the measured distributions the fourth and higher order statistical moments cannot be determined with the required precision.

4.5 Formation process

4.5.1 Rate estimations

In order to get insight into the mechanism by which the aggregates form we estimate rates for the two possible formation processes, i.e. simultaneous multi-photon as well as sequential single-photon excitation. In the case of sequential excitation a first atom is excited off-resonantly as the initial grain while the following atoms are resonantly excited with the distance from an already excited Rydberg atom being determined by the laser detuning. Since the off-resonant excitation of the grain is

slow as compared to the resonant excitation of the following atoms the dynamics of the overall process is determined by the off-resonant excitation rate γ_1 of the first atom

$$\gamma_{n,seq} \approx \gamma_1 = \frac{\Omega^2}{\Gamma} \frac{1}{1 + 4\Delta^2/\Gamma^2} \approx \frac{\Omega^2 \Gamma}{4\Delta^2} \tag{4.6}$$

where Γ is a dephasing rate and the last approximation is valid for $\Delta \gg \Gamma$.

In the case of simultaneous multi-photon excitation, the rate is given by

$$\gamma_{m,sim} = \left(\frac{\Omega^m}{2^{m-1} \prod_{i=1}^{m-1} \delta_i} \right)^2 / (m\Gamma) \tag{4.7}$$

(as can be deduced from e.g. [Grynberg and Cagnac, 1977]), assuming that the overall process is resonant, i.e. that the energy of m photons matches the overall energy of the aggregate. δ_i is the detuning from the ith intermediate state, i.e. from the state containing i excitations. For the formula given in eq. 4.7 to be valid each detuning δ_i has to be large as compared to both the dephasing rate and the respective multi-photon Rabi frequency.

Comparing the two rates we find the ratio of sequential to simultaneous excitation to scale as $\Gamma^2 \Delta^{2m-4} \Omega^{2-2m}$. Accounting for the availability of atoms at specific distances slightly modifies these rates, nonetheless for $\Omega < \Delta$ the ratio still increases exponentially with aggregate size m.

Applying the above scaling to our experimental parameters ($\Omega \approx 0.4\,\mathrm{MHz}$ and $\Gamma \approx 1\,\mathrm{MHz}$) and accounting for the availability of atoms at specific distances we estimate that for pair excitation the simultaneous excitation rate is already approximately one order of magnitude smaller than the sequential excitation rate. For the excitation of aggregates of size m=3 the simultaneous excitation is suppressed by an additional factor of $\approx 4 \times 10^3$ at Δ=20 MHz. Hence we conclude that in our experiments the dominant formation mechanism is the sequential excitation of aggregates.

4.5.2 Comparison with many-body calculations

In order to strengthen the conclusions drawn from the simple rate estimates in Ch. 4.5.1 we compare our experimental data to many-body calculations which were performed by David Schönleber and Martin Gärttner in the group of Jörg Evers at the Max-Planck-Institut für Kernphysik in Heidelberg (see e.g. [Schempp *et al.*, 2014; Schönleber *et al.*, 2014]). The general challenge in the description of interacting Rydberg systems is the fact that the Hilbert space grows exponentially with the

atom number. In interacting Rydberg systems the Hilbert space can be truncated by discarding those states which contain more Rydberg excitations than allowed by the dipole blockade. However, exact treatments are still limited to a small number of excitations.

In quantum optics the so-called Monte-Carlo Wave Function (MCWF) [Dalibard *et al.*, 1992; Mølmer *et al.*, 1993] approach is a standard technique for the description of open quantum systems, e.g. systems subject to dephasing. The approach is based on wave function evolution which in the presence of dephasing and decay not only depends on the Hamiltonian of the system (describing the coherent evolution), but an additional imaginary term. This term contains contributions from the different dephasing mechanisms of the system and makes the overall evolution non-Hermitian, i.e. irreversible in time. In the MCWF approach the initial wave function is evolved with this non-Hermitian operator for a sufficiently small time step. In addition at each step one decides whether the system has undergone a quantum jump. Many of these small time steps are then repeated in order to obtain possible evolutions (trajectories) of the system. In the end many of these trajectories have to be averaged in order to gain information about the typical behavior. The method is equivalent to solving the optical Bloch equations (OBE), however it requires less computational power since the number of variables to solve for scales as the size of the Hilbert space N while the OBE require N^2 equations to be solved. For interacting Rydberg systems, however, despite the Hilbert space truncation, the MCWF approach is still computationally demanding since it requires averaging over various spatial configurations as well as different temporal evolutions (trajectories) of the same spatial arrangement. Hence a feasible system size is smaller than the one used in our experiments. Nonetheless the MCWF approach on a small system can be used to benchmark other calculations.

In systems where the dephasings are large as compared to the coherent couplings the excitation dynamics are well captured by a rate equation (RE) formalism which treats each atom separately and hence allows for the description of large systems. The interactions are incorporated via an energy shift depending on the state of the neighboring atoms which modifies the excitation rate for the atom of interest [Ates *et al.*, 2007; Heeg *et al.*, 2012]. By construction, this approach cannot capture processes like the simultaneous multi-photon excitation of several Rydberg atoms since only one atom is treated at a time.

Comparing both models for our experimental parameters on a small volume shows very good agreement between the two approaches (see Supplemental Material of [Schempp *et al.*, 2014]). This finding plus the fact that the RE agrees well with

the experimental data (see figs. 4.1, 4.2, 4.4 and 4.5) strengthens our conclusion that simultaneous multi-photon excitation, which is fundamentally not captured by the RE model, does not play an important role for our experimental parameters.

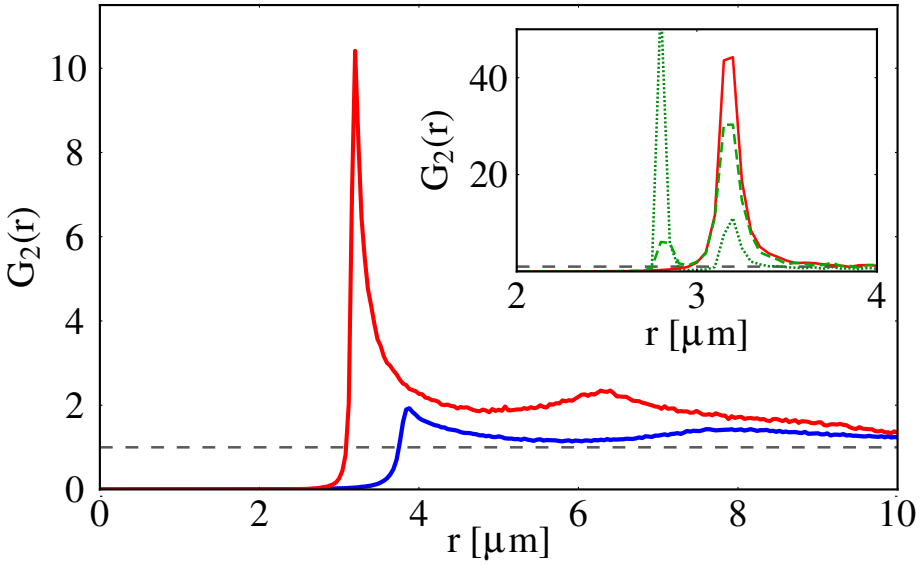

Figure 4.6: Pair correlation functions $G_2(r)$ obtained from the RE model. The blue curve shows the correlation function for $\Delta = 5\,\mathrm{MHz}$, the red curve for $\Delta = 15\,\mathrm{MHz}$. The inset shows MCWF simulations for $\Delta = 15\,\mathrm{MHz}$, and dephasing rates Γ =0 (green, dotted) and $\Gamma = 1\,\mathrm{MHz}$ (green, dashed), compared to the RE simulation with $\Gamma = 1\,\mathrm{MHz}$ (red, solid). To improve visibility, the dotted curve is scaled by a factor of $1/10$. The different peak amplitudes between the inset and main figure are due to the different simulation volumes and finite size effects.

The many-body calculations described above can also provide extra information about the system which is not directly accessible in the experimental data. Fig. 4.6 shows the pair correlation function $G_2(r)$ as extracted from the RE (main graph and red curve in inset) as well as from the MCWF model (green curves in the inset). As expected the result from the RE model features a strong peak at $r = (C_6/\Delta)^{1/6}$ corresponding to the preferred pair distance in the case of sequential excitation. A second smaller peak at $r = 2(C_6/\Delta)^{1/6}$ hints at structures extending beyond pairs of atoms. Clearly the excitation at Δ=15 MHz (red curve) results in much stronger correlations than that at Δ=5 MHz (blue curve). The inset shows a comparison with the MCWF results. While the RE model fundamentally does not capture simultaneous excitation of correlated atoms and hence results in only one peak in $G_2(r)$ corresponding to sequential excitation, the MCWF calculations produce a peak at $r = (C_6/(2\Delta))^{1/6}$ indicating a small contribution from simultaneous excitation for

Γ=1 MHz (green dashed line) and a stronger contribution for Γ=0 (green dotted line). The weak contribution from simultaneous excitation for Γ=1 MHz supports again our conclusion from Ch. 4.5.1, i.e. that the process of simultaneous excitation plays only a minor role in our system.

4.6 Dephasing mechanisms

We have seen from comparison with the rate equation model that in our system the dominant aggregate formation mechanism is sequential excitation. So far we have assumed a dephasing rate of 1 MHz which was inferred from spectroscopic measurements of the EIT excitation lineshape. As has been mentioned in Ch. 2.2, laser dephasing alone is probably not sufficient to destroy multi-atom coherence since it is common to all atoms. Instead most likely the atomic motion is the reason for the observed dephasing, since it dephases all atoms independent of each other. The experiments presented here were performed at a temperature of 82 μK which corresponds to an average velocity of the atoms of $\langle v \rangle = \sqrt{\frac{8k_BT}{\pi m}} = 0.14 \mu m/\mu s$. As a consequence, the time it takes the atoms to move by 50% of the optical wavelength (480 nm) is 1.7 μs. Though this is not a rigorous definition of a dephasing rate, the resulting rate is within a factor of two consistent with the value of 1 MHz use for our calculations.

4.7 Prospects

In the future distinguishing the two formation mechanisms experimentally will provide a much better understanding of the formation of correlated structures. For this purpose it would be interesting to investigate the excitation *dynamics* experimentally. Coherent multi-photon excitation of an m-atom aggregate would result in Rabi oscillations between 0 and m Rydberg excitations, where the result of a single measurement would always be either 0 or m. To see this bimodal behavior, however, requires a detection efficiency close to 1, which could in principle be achieved using the newly developed interaction enhanced imaging approach discussed in Ch. 5.1. In order to get into a regime where coherent multi-photon excitation is expected to be dominant, the ratio between coherent coupling and dephasing processes has to be increased. Using a better laser source will allow for Rabi couplings which are stronger by an order of magnitude. Combined with lower temperatures, e.g. by evaporative cooling, which would reduce the dephasing rate by an order of magnitude we can

reach the regime of coherent multi-photon excitation.

Chapter 5

Interaction enhanced imaging of Rydberg atoms

This chapter is based on the following publications:

Interaction enhanced imaging of individual Rydberg atoms in dense gases
G. Günter, M. Robert-de-Saint-Vincent, H. Schempp, C. S. Hofmann, S. Whitlock, M. Weidemüller
Physical Review Letters **108**, 013002 (2012)

Observing the dynamics of dipole-mediated energy transport by interaction enhanced imaging
G. Günter, H. Schempp, M. Robert-de-Saint-Vincent, V. Gavryusev, S. Helmrich, C. S. Hofmann, S. Whitlock, M. Weidemüller
Science **342**, 953-956 (2013)

In Ch. 4 we have demonstrated the possibilities of extracting information about a correlated many-body system by investigating its counting statistics. Also other indirect approaches can prove the existence and to some extend also the character of many-body correlations. However, the ultimate goal has of course always been the direct imaging of these many-body states. In general the imaging of Rydberg atoms is a challenging task and has only been realized in the last few years. Spatially resolved images of Rydberg atoms have first been obtained using field ion microscopy, i.e. elaborate ion optics are used, followed by spatially resolved detection of the

magnified ion distribution [Schwarzkopf *et al.*, 2011]. An optical approach has recently been realized using an atom microscope. In this approach, after exciting the Rydberg many-body state from an optical lattice, the remaining ground state atoms are removed using resonant light. The Rydberg atoms are subsequently deexcited to the ground state where they are pinned in a deep optical lattice site and are finally imaged using fluorescence imaging [Schauß *et al.*, 2012]. In earth alkali atoms a direct fluorescence imaging approach is possible when only one valence electron is excited to a Rydberg state while the second one can be driven on a cycling transition to scatter photons. This approach has recently been demonstrated with Strontium atoms [McQuillen *et al.*, 2013].

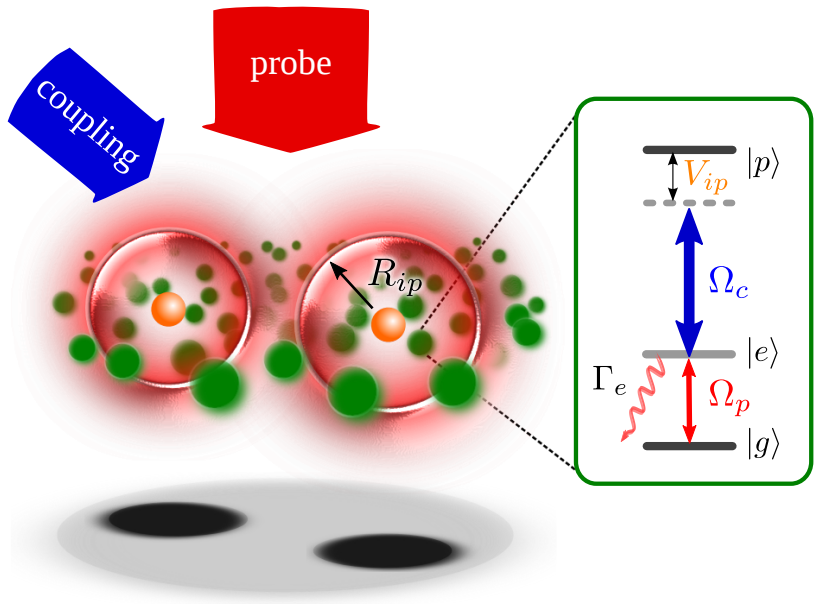

Figure 5.1: Basic mechanism of the imaging scheme discussed in this chapter: each impurity (indicated as orange spheres) interacts with the Rydberg states of the surrounding bath of probe atoms (green) within a radius R_{ip}. These interactions of strength V_{ip} shift the Rydberg levels of the probe atoms and thus break the two-photon resonance condition required for EIT. As a consequence the atoms in the vicinity of an impurity are rendered absorbing. Therefore each impurity casts a shadow in the absorption image.

In this Chapter we introduce and demonstrate a new imaging technique developed during this thesis. It is based on electromagnetically induced transparency (EIT) as introduced in Ch. 3, and on the interactions between the Rydberg atom of interest and the Rydberg states of the surrounding atoms. Mapping the properties of a Rydberg state onto a strong optical transition using EIT, we realize a

first amplification mechanism. A second amplification mechanism makes use of the fact that many ground state atoms surrounding the Rydberg atom of interest contribute to its signature. In contrast to the schemes described in [Schwarzkopf *et al.*, 2011; Schauß *et al.*, 2012] our technique is non-destructive in a sense that the actual Rydberg atom distribution is not destroyed by the imaging process, and therefore in principle allows for taking a series of images on the same sample to e.g. follow its time evolution. Fundamentally the detection efficiency is only limited by the time required for imaging, during which the Rydberg atoms can decay.

5.1 Interaction enhanced imaging scheme

The basic mechanisms of our interaction enhanced imaging scheme are sketched in fig. 5.1 and discussed in detail in [Günter *et al.*, 2012] (a similar idea has been proposed in [Olmos *et al.*, 2011]). We first excite some atoms to the Rydberg state $|i\rangle$ (indicated as orange spheres). These atoms are actually to be imaged and will in the following be referred to as "impurities". The impurities are embedded in a bath of ground state atoms which can in principle be rendered transparent by realizing an EIT system involving a "probe" Rydberg state $|p\rangle$ as sketched in fig. 5.1 and discussed in detail in Ch. 3.1. However, the impurity Rydberg atom shifts the Rydberg states of the surrounding atoms thereby introducing an effective detuning of the coupling field. This effective detuning is given by the interaction energy V_{ip} between the impurity $|i\rangle$ and the atom in the probe Rydberg state $|p\rangle$ and therefore depends on their spatial separation d.

Fig. 5.2 a) shows theoretical EIT spectra for different distances from the impurity (i.e. for different effective coupling laser detunings due to interaction induced level shifts). While for $d \to \infty$ we find the spectrum as calculated in Ch. 3.1 with a pronounced transparency on resonance, any finite effective detuning (caused by a finite interaction energy V_{ip}) shifts the transparency resonance and thus increases the absorption for resonant probe light. For very small distances, the spectrum is the Lorentzian absorption spectrum of a two-level system. Fig. 5.2 b) shows the absorption of a bath atom as a function of its distance d from the impurity for resonant probe light ($\Delta_p = 0$) and assuming van der Waals interaction between the impurity and the probe Rydberg state $V_{ip} = C_6/d^6$, with C_6 being the interaction strength. The absorption rapidly drops from the two-level response to almost no absorption at the interstate blockade radius $R_{ip} = (C_6 2\Gamma_e/\Omega_c^2)^{1/6}$ at which the interaction strength equals the EIT bandwidth $\Omega_c^2/(2\Gamma_e)$. This means that all bath atoms in a sphere of

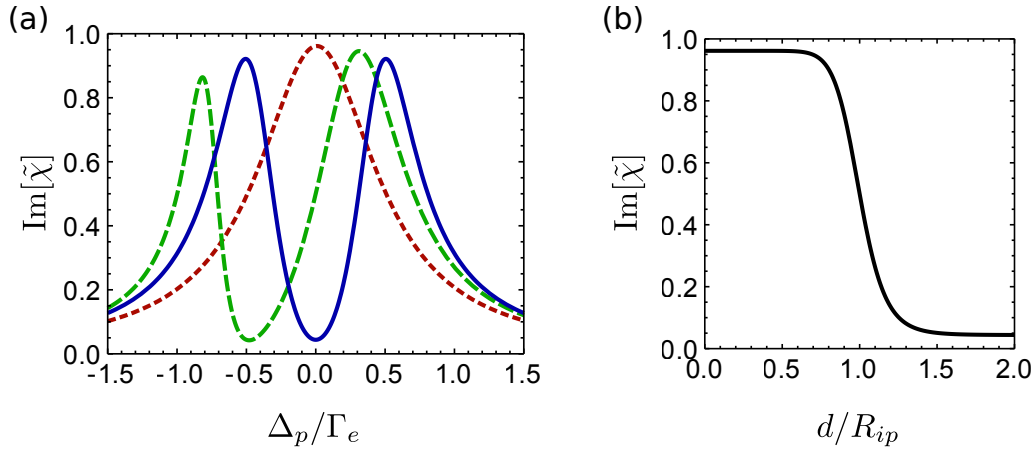

Figure 5.2: a) EIT spectra (Im$[\tilde{\chi}]$ as a measure for absorption with $\tilde{\chi} = \rho_{12}\Gamma_e/\Omega_p$) for different distances of a bath atom from the impurity with $\Omega_c = 1$ and $\Delta_c = 0$ (in units of Γ_e): the solid blue line corresponds to $d \to \infty$ where the interaction induced level shift vanishes, the dashed green line to $d = R_c$ where $V_{ip} = \Omega_c^2/(2\Gamma_e)$ and the dotted red line to $d = 0$ where $V_{ip} \to \infty$. We see that the absorption of a resonant probe laser beam ($\Delta_p = 0$) depends on the distance of the bath atom from the impurity causing the level shift. b) shows this absorption as a function of distance. At $d = R_c$ the absorption has dropped to 50 % of its maximum value. As a consequence each impurity creates an absorbing disk of radius R_c.

radius R_{ip} around an impurity are rendered absorbing.

As mentioned above our scheme exploits two amplification mechanisms: on the one hand we probe many atoms in the vicinity of one impurity in order to detect this one impurity. On the other hand we probe on a strong optical transition such that many scattered photons contribute to the detected signal. Interestingly, our scheme can also be used to image other objects like e.g. an ion embedded in a bath of atoms if this object shifts the Rydberg energy levels of the surrounding bath atoms. A similar approach has also been used to spatially resolve the electric field distribution caused by surface charges [Tauschinsky *et al.*, 2010].

From the discussion above we can already define some criteria for the choice of the two Rydberg states as well as the other experimental parameters. First of all, the interaction between probe state atoms V_{pp} has to be small in order to achieve good transparency in the absence of impurities. As discussed in Ch. 3 the degree of transparency depends on the Rydberg state $|p\rangle$, the atomic density and the probe light intensity. The larger the *coupling* Rabi frequency is the higher can the probe field intensity and the atomic density be while still maintaining high

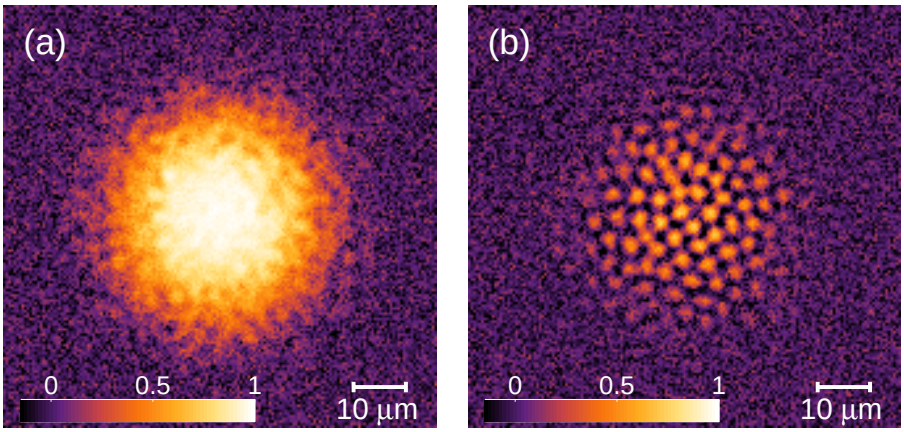

Figure 5.3: Simulated images of a two-dimensional cloud without EIT laser (a) and with EIT laser and impurities (b). (a) is a standard absorption image where the bright regions indicates high absorption while in (b) only the atoms in the vicinity of an impurity contribute to the absorption signal, thus leading to a distribution of absorbing spots which represents the distribution of impurities.

transparency. Unfortunately the available laser power sets an upper limit on the achievable coupling Rabi frequency. Therefore at first glance we have to use low-lying Rydberg states, small atomic densities and small probe field intensities [Pritchard *et al.*, 2010; Hofmann *et al.*, 2013b]. However, when the probe field intensity is too small the image quality is eventually limited by photon shot noise. Furthermore, having many atoms contributing to the signal of an impurity, as it is desirable in order not to be limited by atom shot noise, requires a sufficiently large atomic density. For the same reason (atom shot noise) a large radius R_{ip}, determined by the interstate interaction V_{ip}, is beneficial, which favors higher-lying Rydberg states. Finally, in order to resolve single impurities their corresponding absorbing spheres should not overlap. To this end the interaction strength between two impurities should be larger than that between an impurity and a probe Rydberg atom to prevent two impurities being excited too close to each other. To summarize, the different interactions should be such that the corresponding blockade radii fulfill the relation $R_{pp} < R_{ip} < R_{ii}$. In addition, the probe field intensity as well as the atomic density have to be chosen such that on the one hand a reasonable transparency is preserved and on the other hand atom as well as photon shot noise do not distort the image quality too much.

Fig 5.3 shows simulated single-shot images using a two-dimensional cloud, i.e.

a cloud of which the extent along the imaging axis is smaller than the blockade radius of an impurity atom. The simulations include relevant experimental quantities such as a finite optical resolution (NA=0.25), and atom as well as photon shot noise. Fig. 5.3 a) is a standard absorption image of this cloud with the bright regions corresponding to large absorption. Fig. 5.3 b) in addition features impurities as well as a coupling laser beam to render the cloud transparent. As a consequence only the atoms in the vicinity of an impurity absorb light, thereby casting a shadows of radius R_{ip} around each impurity, which is blurred by the finite optical resolution. For the simulations we assumed a 2D-density of $40\,\mu\mathrm{m}^{-2}$ and Rydberg states $|i\rangle = |55S\rangle$ and $|p\rangle = |28S\rangle$. The laser parameters are $\Omega_c = 2\pi \times 50\,\mathrm{MHz}$, $\Omega_p = 2\pi \times 5.8\,\mathrm{MHz}$ for Rabi frequencies and $\gamma_c = \gamma_p = 2\pi \times 1\,\mathrm{MHz}$ for the laser dephasings. The exposure time is $10\,\mu\mathrm{s}$ during which the atoms are assumed to not move significantly. Further details, in particular on the simulation of the impurity excitation are described in [Günter *et al.*, 2012; Günter, 2013].

5.2 Experimental demonstration

To experimentally demonstrate the imaging scheme as described above we chose the Rydberg states $|i\rangle = |50S\rangle$ and $|p\rangle = |37S\rangle$. We start by preparing atoms in a cigar-shaped cloud at typical densities of $5 \times 10^{10}\,\mathrm{cm}^{-3}$. Part of the cloud is illuminated by an elliptically shaped laser beam of size $64\,\mu\mathrm{m} \times 10\,\mu\mathrm{m}$ (Gaussian beam waists) which couples the atoms to the probe state $37S$ with a peak Rabi frequency of $\Omega_c \approx 2\pi \times 9\,\mathrm{MHz}$, thereby rendering this part of the cloud transparent. In the center of this transparent region we excite impurity atoms using a tightly focused excitation beam. The geometry described here is sketched in fig. 5.5. The lasers for the impurity excitation are red detuned from the intermediate state by $\approx 65\,\mathrm{MHz}$. The probe light illuminates the cloud homogeneously with a Rabi frequency of $\Omega_p \approx 2\pi \times 2\,\mathrm{MHz}$. Fig. 5.4 illustrates the typical pulse sequence.

The geometry of the beams as well as raw images are shown in fig. 5.5. Fig. 5.5 b) shows raw absorption images without previously excited impurities, i.e. an elliptical transparent spot at the center of the atomic cloud. Fig. 5.5 c) shows the same raw images with previously excited impurities. As a signature we find enhanced absorption in the center of the transparent spot. Subtracting these images from each other we obtain an image of the distribution of additional absorbers which reflects the distribution of impurities as shown in fig. 5.5 d). While we have not yet spatially resolved single impurities we can determine the number of atoms rendered absorbing

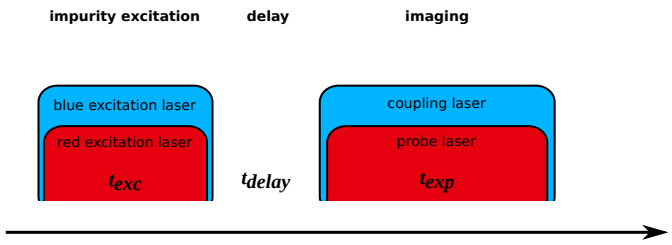

Figure 5.4: Typical pulse sequence for interaction enhanced imaging. The impurities are excited during a time t_{exc}. After a short time t_{delay} the imaging pulses are turned on for a variable exposure time t_{exp}. In order to obtain a reference image without impurities we apply the same pulse sequence but with the blue impurity excitation laser pulse turned off.

due to the presence of impurities, as well as their spatial distribution.

To maximize the total absorption signal we apply an electrical field of 0.5 V/cm in order to tune into the Förster resonance

$$|37S_{1/2} + 50S_{1/2}\rangle \leftrightarrow |36P_{1/2} + 51P_{3/2}\rangle. \tag{5.1}$$

Doing so we realize strong dipolar interactions which come along with an increased interstate blockade radius of 3.8 μm and thus enhance the number of additional absorbers per impurity.

The best imaging sensitivity was achieved by compressing the atoms to a quasi one-dimensional shape of radial extent $\sigma_r = 4.9\mu$m and a peak density of $\rho_0 = 2.4 \times 10^{11}\,\mathrm{cm}^{-3}$. Fig. 5.6 a) shows the number of additional absorbers as a function of the number of impurities. The number of impurities is determined from field ionization and varied by changing the excitation power. For small excitation numbers we find a linear relation between the number of additional absorbers and the number of impurities from which we can calculate the gain factor of the imaging process. We find that in the linear regime each impurity renders 19 ± 2 atoms absorbing. For larger impurity numbers, where the excitation saturates due to the dipole blockade, impurities are more likely to be excited in the wings of the atomic cloud where the density is smaller than in the center. As a consequence these impurities render less atoms absorbing, thereby reducing the average number of absorbers per impurity. Fig. 5.6 a) shows data averaged over 50 repeats, however, we are able to see the distribution of as few as 6 impurities even in a single realization as can be seen in fig 5.6 b).

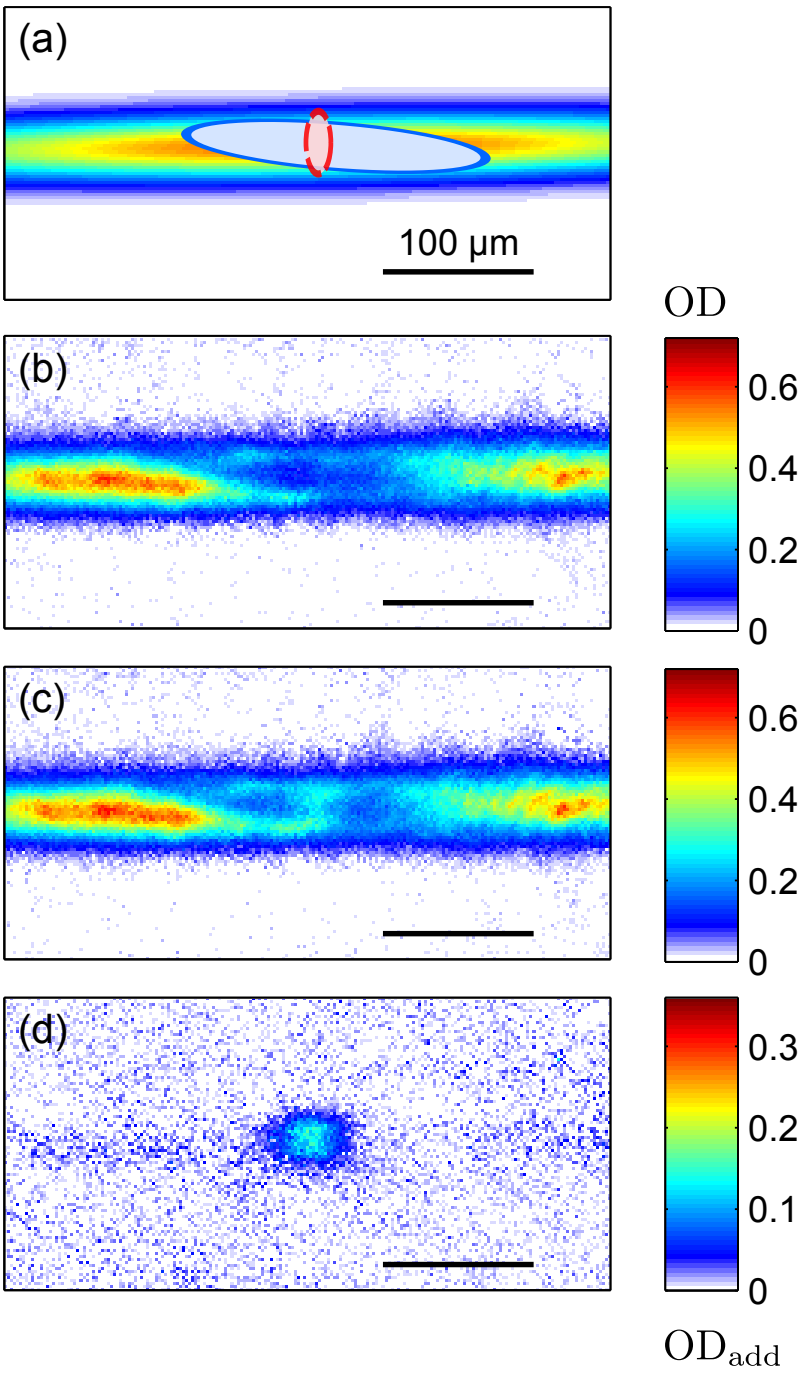

Figure 5.5: Absorption images illustrating the procedure to obtain images of the impurity distribution. a) sketches the geometry of the imaging as well as the excitation laser with respect to the atomic cloud. b) shows an absorption image of the cloud which is rendered transparent by the elliptically shape coupling beam, while c) shows the same image but impurities have been excited previously in the center of the transparent spot which render the atoms absorptive. d) shows the difference between c) and b), from which we obtain information about the number as well as the spatial distribution of additional absorbers.

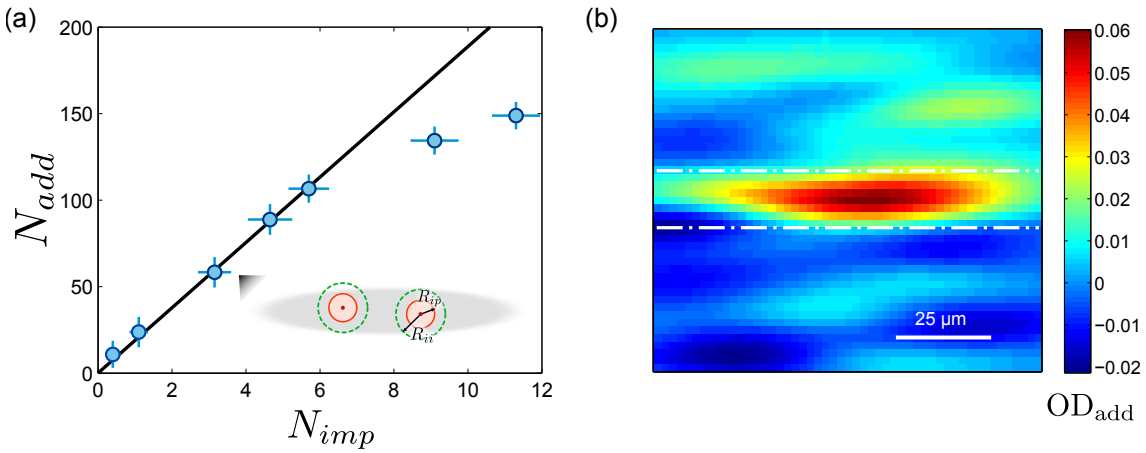

Figure 5.6: a) shows the number of additional absorbers N_{add} in the EIT images vs. the number of impurities N_{imp} as obtained from the ion signal in a quasi one-dimensional atomic cloud. The Rydberg states are $50S$ (impurities) and $37S$ (probe). We find a linear increase of the absorber number when exciting small numbers of impurities. Once the impurity number starts to saturate due to the Rydberg blockade the excitations are likely to be placed in the wings of the cloud where due to the lower ground state atom density the number of absorbers per impurity is reduced. Fitting a slope to the non-saturated part of the data we find a gain factor of 19 ± 2 additional absorbers per impurity. b) shows an image of a distribution of ≈ 6 impurities obtained from a single experimental realization with an exposure time $t = 5\mu$s. The white dashed lines indicate the extent of the atomic cloud.

Chapter 6

Coherent and incoherent energy transport

This chapter is partially based on the following publications:

Observing the dynamics of dipole-mediated energy transport by interaction enhanced imaging
G. Günter, H. Schempp, M. Robert-de-Saint-Vincent, V. Gavryusev, S. Helmrich, C. S. Hofmann, S. Whitlock, M. Weidemüller
Science **342** 953-956 (2013)

Quantum and classical spin transport in Rydberg dressed atomic gases
H. Schempp, G. Günter, S. Wüster, M. Weidemüller, S. Whitlock
in preparation

In this Chapter we discuss the applications of our imaging scheme to study dipole-mediated transport of Rydberg excitations. After presenting first indications of energy transport in Ch. 6.1 and discussing a simplified model for this transport, we study the observed classical energy transport in more detail in Ch. 6.2. We introduce an effective operator model in Ch. 6.3 to describe the transport in our system more rigorously and compare its results to our experimental data. Finally, in Ch. 6.4 we present first observations on the dynamics in a purely coherent regime, before discussing a scheme to realize the transition between classical and coherent dynamics in future experiments.

6.1 Imaging transport phenomena

Here we discuss the observation of dipole-mediated energy transport of Rydberg excitations. Optimizing the imaging scheme presented in the last Chapter, we find that using a Förster resonance allows for maximizing the impurity-probe interactions. With the states $50S$ as impurity and $37S$ as the probe state we were thus able to increase the gain of the imaging system by tuning into the Förster resonance $|37S_{1/2} + 50S_{1/2}\rangle \leftrightarrow |36P_{1/2} + 51P_{3/2}\rangle$. In the following we choose the states $|i\rangle = |38S\rangle$ and $|p\rangle = |37S\rangle$ which exhibit strong dipolar interactions due to the Förster resonance $|37S + 38S\rangle \leftrightarrow |37P + 37P\rangle$. In addition this particular type of Förster resonance features dipolar exchange since the state $37P$ couples strongly to both $37S$ and $38S$, thereby allowing for the exchange process $|37S + 38S\rangle \leftrightarrow |38S + 37S\rangle$. Later on we will use the states $|i\rangle = |50S\rangle$ and $|p\rangle = |48S\rangle$, for which direct exchange is strongly suppressed, but which instead exhibits a different exchange mechanism. Dipolar exchange processes have been observed before, also in early experiments using cold Rydberg gases [Mourachko *et al.*, 1998; Anderson *et al.*, 1998]. However, now we are able to see the dynamics of this process in a spatially resolved way for the first time.

In the following we give a simplified description of the relevant physics. In Ch. 6.3 we will then introduce a more rigorous theoretical model. The particular exchange process for our experimental setting is that between an impurity in state $38S$ and the $37S$ Rydberg state of the surrounding optically dressed gas. The coherent exchange frequency depends on the interaction strength V_{ip} between impurity and probe state as well as on the steady state Rydberg state admixture ρ_{pp} of the probe atom, assuming that we can treat the EIT in the adiabatic limit. Both of these contributions depend on the distance between the impurity and the probe atom such that the coherent exchange rate is

$$\omega_{coh}(r) = V_{ip}(r)\rho_{pp}(r) = \frac{C_3}{r^3}\rho_{pp}(r). \tag{6.1}$$

where C_3 quantifies the interaction strength between impurity and probe state. For large distances and in the weak probe limit ρ_{pp} asymptotes to $\approx \Omega_p^2/\Omega_c^2$ as known for an EIT system. At short distances the interaction with the impurity shifts the probe Rydberg state out of resonance thereby reducing the population ρ_{pp}. $\rho_{pp}(r)$ can be calculated from the laser parameters by introducing an additional distance dependent detuning of the coupling laser. $\rho_{pp}(r)$ vanishes at small distances. Together with the $1/r^3$-dependence of the interaction potential this leads to a maximum of the coherent exchange rate ω_{coh} at $r \approx R_{ip}$.

In addition to the coherent exchange process the imaging can be thought of as introducing decoherence by continuously projecting the quantum state of the many-body system. This decoherence rate is given by the photon scattering rate, which is related to the intermediate state population and thus also depends on the distance from the impurity. For a simple estimate of the scattering rate caused by one impurity we spatially integrate the photon scattering rate around the impurity assuming a constant atomic density.

For our experimental parameters we estimate the decoherence rate γ_{env} to be ≈ 150 times larger than the typical coherent exchange rate. Assuming that this process can be treated as a dephasing, which leads to a rapid decay of the atomic coherence, we can neglect the coherences of the density matrix and define an effective classical rate equation for the populations. The resulting hopping rate reads

$$\Gamma_{hop} \approx \frac{\omega_{coh}^2}{\gamma_{env}}. \tag{6.2}$$

For purely classical hopping we expect a diffusive behavior, thus we can describe the evolution of the second moment of the impurity distribution by a diffusion law:

$$\sigma(t)^2 = \sigma^2(0) + 2Dt. \tag{6.3}$$

where D is proportional to the hopping rate Γ_{hop}. Using eq. 6.2, eq. 6.1 together with $\rho_{pp} \sim \Omega_p^2$ and $\gamma_{env} \sim \Omega_p^2$ (since the two-level photon scattering rate Ω_p^2/Γ_e) we estimate $D \sim \Omega_p^2$.

We observe the above discussed transport dynamics by varying the exposure time of the interaction enhanced imaging pulse, i.e. the time during which impurity-probe exchange can occur due to the presence of Rydberg dressed atoms serving as hopping partners. Fig. 6.1 shows images of the impurities after different exposure times (a) as well as the size of the cloud as a function of exposure time (blue circles in b). We find σ_x^2, i.e. the second moment of the impurity distribution in x-direction, to grow approximately linearly with time as expected from the above discussion (transport in y-direction is suppressed due to the geometry of the EIT coupling laser beam as sketched in fig. 6.1). However, based on the data shown in fig. 6.1 we can not rule out a possible deviation from linear behavior. Given the small number of data points makes it hard to estimate statistical uncertainties. In addition the range of measured $\sigma(t)^2$ is not even close to spanning an order of magnitude, thus fitting a power law does not yield very reliable results.

By detuning from the Förster resonance we reduce the interaction strength, thus slowing down the transport dynamics as we can see in the experiment. Namely the

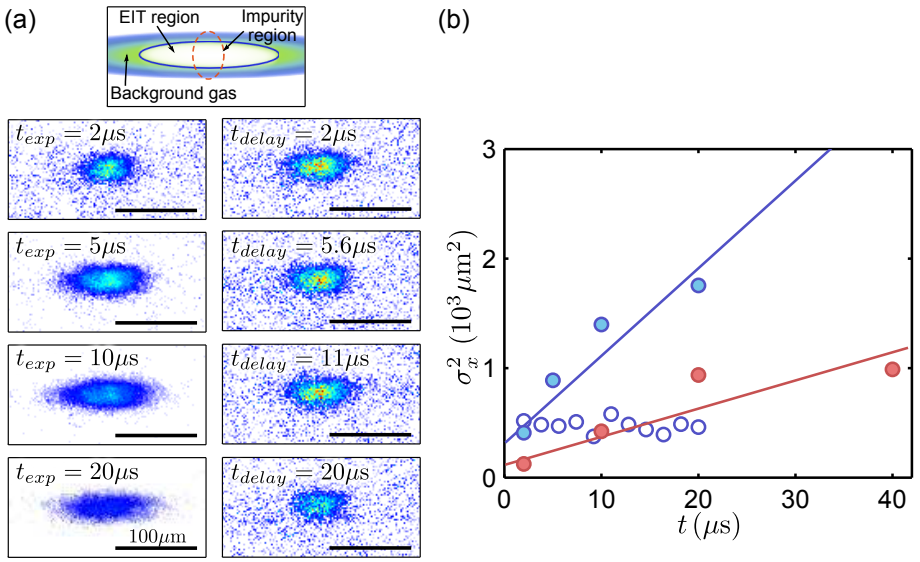

Figure 6.1: Growth of the distribution of additional absorbers during imaging. a) shows snapshots of the impurity distribution after different exposure times (left column) and after different delay times at fixed exposure time (right column). The geometry of the cloud and the different laser beams are sketched above. b) shows the second moment of the measured impurity distribution σ_x^2 vs. exposure time. Tuning into the Förster resonance we find a fast energy transport with σ_x^2 growing approximately linearly with exposure time (blue filled circles). Slower transport is found when the Förster defect is slightly detuned from 0. For comparison the blue empty circles are taken with a fixed exposure time of 2 μs and a variable delay t between impurity excitation and the actual imaging.

red circles in fig. 6.1 show the dynamics at a Förster defect of 100 MHz. This defect also changes the character of the interactions from $1/r^3$ to $1/r^6$. A simple estimate of the diffusion rate based on van der Waals interaction alone is too small to explain the data, suggesting additional mechanisms to be at work as discussed in [Günter *et al.*, 2013].

To make sure that the observed expansion is indeed due energy transport we performed experiments where we introduced a variable delay between the excitation of impurities and the imaging pulse and found a constant size independent of the delay. This results excludes e.g. mechnical forces between the impurities to be responsible for the expansion.

6.2 Investigating transport dynamics

So far we have discussed our first observation of energy transport and indications for this energy transport to behave classically, i.e. for the impurities to spread out diffusively. In order to understand the transport dynamics in more detail we have taken better data for a different pair state, namely we prepare the impurities in the state $50S$ and use the state $48S$ for the EIT imaging. These two states feature a Förster resonance at a small electric field via the pair state degeneracy $|48S_{1/2}, 50S_{1/2}\rangle \leftrightarrow |48P_{1/2}, 49P_{1/2}\rangle$ as can be seen from fig. 2.4. In contrast to the $37S - 38S$ resonance discussed above, the direct exchange interaction $|48S, 50S\rangle \leftrightarrow |50S, 48S\rangle$ is strongly suppressed. Instead we expect the dominant process, even at a finite Förster defect, to be a "fission" process of the states $48S$ and $50S$, resulting in the population of the pair state $|48P_{1/2}, 49P_{1/2}\rangle$. In the following the $48P$ atom produced during this process can diffuse resonantly via the exchange $|48S, 48P\rangle \leftrightarrow |48P, 48S\rangle$. The S-P diffusion can be considerably simple since it does not involve any intermediate states, and to lowest order it does not depend on the electric field.

The resulting transport dynamics is shown in fig. 6.2. The initial Förster defect is $\Delta_F = 103\,\mathrm{MHz}$. The size σ_x^2 is extracted from averages over 100 repeats of the same experiment. In order to estimate statistical uncertainties we resample with replacements from these 100 repeats, similar to the bootstrapping procedure discussed in Ch. 4. We average the images of each of these resamples and determine the widths of the averaged images. The error is obtained from the distribution of the obtained widths. Note that in the graph we have subtracted the initial size of the impurity distribution, which we estimate to be 10μm.

Fitting a power law $D_\beta t^\beta$ to the experimental data including the statistical uncertainties we find an exponent $\beta = (1.04 \pm 0.08)$ which is in good agreement with a classical diffusive behavior. Fixing the exponent to 1 we find the diffusion coefficient $D = (153 \pm 5)\mu\mathrm{m}^2/\mu\mathrm{s}$. Note that to account for the fact that the obtained image reflects the time integrated size of the cloud we fit $\sigma(t)^2 = Dt$ instead of the usual definition $\sigma(t)^2 = 2Dt$ in order to extract the diffusion coefficient D (see Supplementary Material of [Günter *et al.*, 2013]).

We expect the diffusion coefficient as determined from fig. 6.2 to depend on various experimental parameters as e.g. the Rabi frequencies used for the EIT imaging. The probe Rabi frequency Ω_p e.g. determines both the coherent exchange rate via the probe state admixture as well as the decoherence rate γ_{env} via the photon scattering rate and should thus influence the diffusion coefficient. To study this dependence we have measured the size of the impurity distribution (state $50S$) using

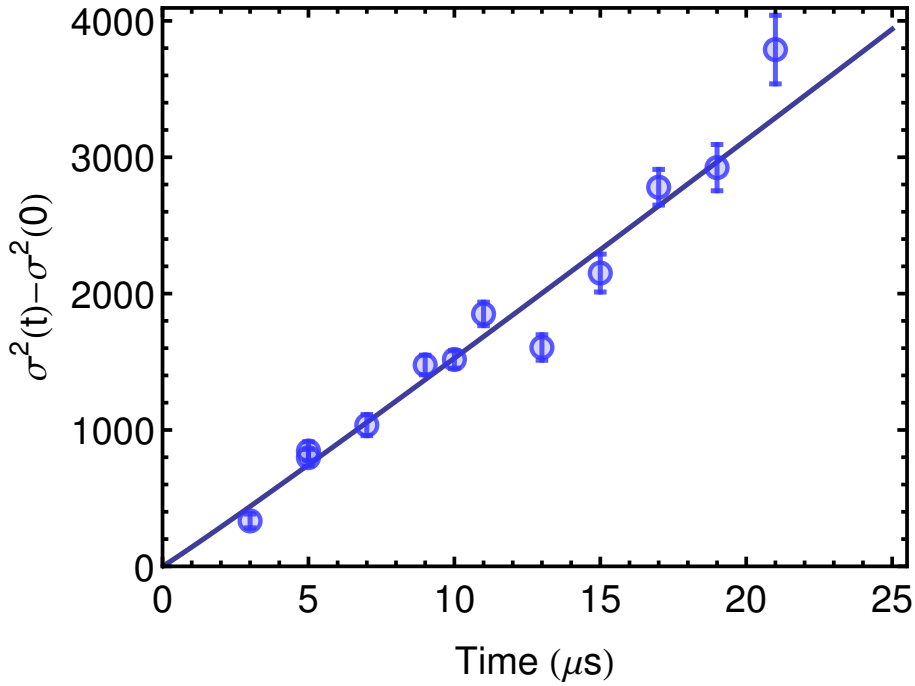

Figure 6.2: Transport dynamics of impurities in the state $50S$ embedded in atoms dressed with the probe state $48S$. The second moment of the impurity distribution (with the initial size of the impurity distribution subtracted) is plotted vs. the exposure time during which transport can happen. The fit with a power law (solid line) yields an exponent of 1.04 ± 0.08. Fixing the exponent to 1 we find a diffusion coefficient $D = (153 \pm 5)\mu\text{m}^2/\mu\text{s}$. The size σ_x is extracted from averages over 100 repeats of the same experiment, the errorbars are obtained by resampling from these 100 repeats.

EIT imaging (state $48S$) at a fixed exposure time of 21μs, but using different probe Rabi frequencies Ω_p.

As shown in fig. 6.2 the squared size of the impurity distribution grows linearly with time. Hence by measuring the squared size of the distribution at a fixed time we can infer how the diffusion coefficient depends on other experimental parameters. Fig. 6.3 shows σ_x^2 as a function of Ω_p^2. When fitting a power law $\sigma_0^2 + \alpha t^\beta$ we obtain an exponent $\beta = 0.8 \pm 0.2$ which is consistent with D being proportional to Ω_p^2 as predicted by the simple model described in Ch. 6.1.

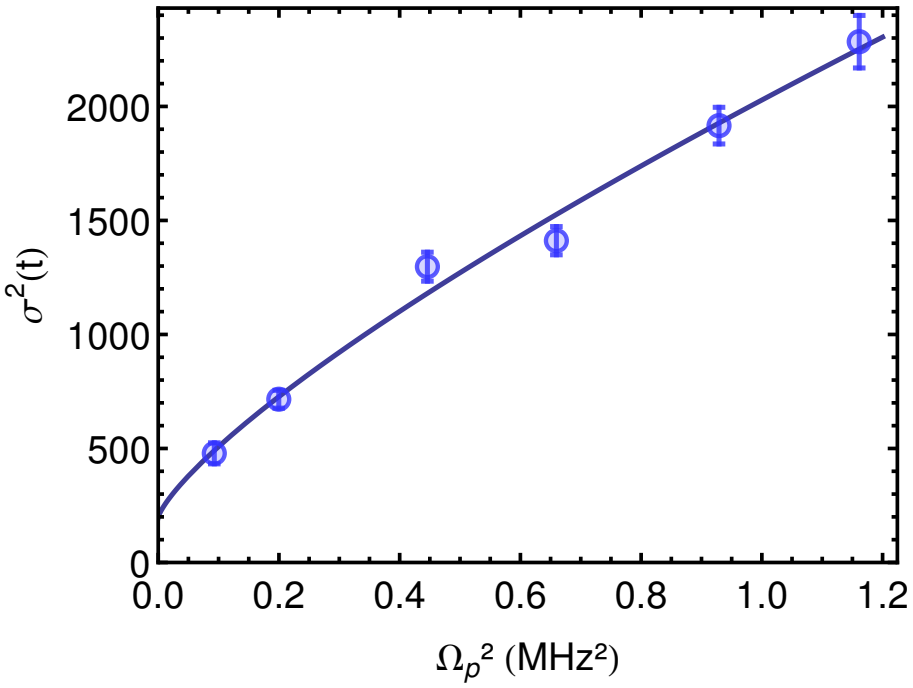

Figure 6.3: Second moment of the measured impurity distribution σ_x^2 after 21 μs exposure for different probe light intensities ($\sim \Omega_p^2$). A power law fit $\sigma_0^2 + \alpha t^\beta$ yields an exponent $\beta = 0.8 \pm 0.2$ which is consistent with the linear increase $D \sim \Omega_p^2$ as predicted by the simple model discussed in Ch. 6.1.

6.3 An effective operator model for energy transport with Rydberg dressed atoms

In this section we improve on the simple model discussed before and derive a more rigorous model to describe the transport dynamics of a Rydberg impurity within a bath of atoms dressed with a Rydberg state. The model has been set up by Shannon Whitlock in the context of spin transport and is applied here to provide a better understanding of the observed energy transport. The exact solution of a system consisting of a Rydberg impurity dressed with a different Rydberg state using an EIT configuration as discussed in the previous sections, is very difficult when including all atomic states involved as well as interactions, and is thus limited to several atoms. Therefore we aimed for an effective description which would reduce the Hilbert space and thus allow for modeling larger systems. We assume that the impurity is a Rydberg P state (i.e. following the initial "fission" process) and thus features direct and field-independent dipolar exchange with the bath atoms dressed

with a Rydberg S state.

The derivation of the effective coupling constants follows the effective operator approach as introduced in [Reiter and Sørensen, 2012]. The basic idea is to separate the Hilbert space into sub-spaces for which the dynamics happens on different time scales. When this criterion is fulfilled certain states may be adiabatically eliminated, thereby allowing for the construction of effective operators describing the dynamics of the remaining states. The usual approach to adiabatic elimination is to solve the density matrix equations for the states subject to fast dynamics under the assumption that other states evolve slowly [Brion *et al.*, 2007]. This procedure can however get quite involved when applied to large systems. In the approach described here the rapidly evolving atomic states are eliminated before setting up the density matrix equations for the reduced system. The two approaches are equivalent, however the later is useful as it allows to identify the dominant terms of the resulting master equation with the effective coupling and decay operators.

We start with a description of two atoms. The relevant levels of our system are sketched in fig. 6.4 a) for a pair of atoms. Note that from here on we use a different notation for the involved Rydberg states: the impurity state is now labeled $|p\rangle$ following the atomic notation, since it is a Rydberg state with angular momentum $l = 1$. As a probe state we assume a Rydberg state with $l = 0$ which is therefore labeled $|s\rangle$. As before, $|g\rangle$ is the ground state and $|e\rangle$ a rapidly decaying excited state. Initially atom 1 starts in the Rydberg state $|p\rangle$ while atom 2 is in a superposition of $|g\rangle$, $|e\rangle$ and $|s\rangle$ due to the applied laser fields of strength Ω_p and Ω_c. The impurity and the dressed atom undergo dipolar energy exchange. As a consequence the impurity excitation $|p\rangle$ can hop to atom 2 which is accompanied by a redistribution of the states of atom 1. Given that one impurity excitation is always present we end up with six pair states in total where the $|p\rangle$ excitation can sit on atom 1 or atom 2 and the state of the respective other atom a is superposition of $|g\rangle$, $|e\rangle$ and $|s\rangle$ as sketched in fig. 6.4 b).

Following [Reiter and Sørensen, 2012] we separate the Hilbert space into a sub-space $\mathcal{H}_g$ comprised of $|pg\rangle$ and $|gp\rangle$, and a second sub-space $\mathcal{H}_e$ comprised of the other four states as indicated by the dashed boxes in fig. 6.4 b). The dynamics within $\mathcal{H}_e$ for finite V_{dd} and Ω_c are fast as compared to the dynamics between $|pg\rangle$ and $|gp\rangle$ which are not directly coupled. In EIT configuration with $\Omega_p \ll \Omega_c$ the coupling $\hat{V}_\pm$ between the two sub-spaces is very weak. Under these conditions we can adiabatically eliminate the sub-space $\mathcal{H}_e$, thereby deriving effective equations for the evolution of the system comprised of the states $|pg\rangle$ and $|gp\rangle$.

To derive the effective operators we write the Hamiltonian of the complete system

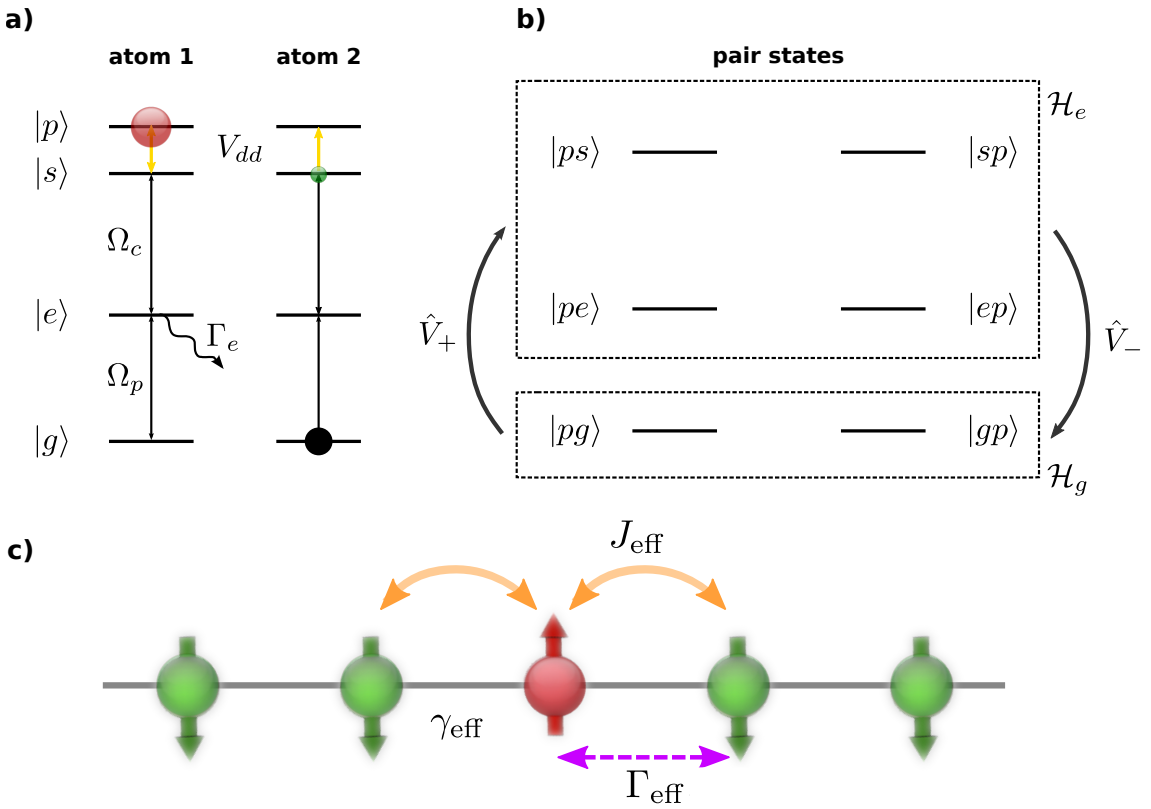

Figure 6.4: a) Relevant levels for the dynamics of an impurity atom in state $|p\rangle$ (initially atom 1) and a an atom in the ground state $|g\rangle$ which is weakly dressed with $|s\rangle$ in an EIT scheme involving the intermediate state $|e\rangle$ (initially atom 2). b) shows the relevant pair states of the system in the single-excitation manifold. When the probe Rabi frequency Ω_p is much smaller than both the coupling Rabi frequency Ω_c and the decay from the intermediate state Γ_e, i.e. when the redistribution of the populations of the states involved in the EIT is fast, we can eliminate the weakly populated pair states $|pe\rangle$, $|ps\rangle$, $|ep\rangle$ and $|sp\rangle$ and thus reduce the system to an effective two-level system comprised of $|pg\rangle$ and $|gp\rangle$. c) shows the mapping onto a spin system where $|p\rangle$ is mapped onto spin up and $|g\rangle$ to spin down. The effective coherent coupling J_{eff}, incoherent coupling Γ_{eff} and dephasing γ_{eff} rates can be derived by adiabatic elimination of the states $|e\rangle$ and $|s\rangle$.

as

$$\hat{H} = \hat{H}_g + \hat{H}_e + \hat{V}_+ + \hat{V}_- \tag{6.4}$$

where $\hat{H}_g$ acts on $\mathcal{H}_g$, $\hat{H}_e$ on $\mathcal{H}_e$, and $\hat{V}_\pm$ couples between the two sub-spaces. The

non-Hermitian Hamiltonian of the quantum jump formalism

$$\hat{H}_{\mathrm{NH}} = \hat{H}_e - \frac{i}{2}\sum_k \hat{L}_k^\dagger \hat{L}_k \tag{6.5}$$

accounts for the different decay channels indexed by k. In our system we have two decay processes contributing to the sum, $\hat{L}_1 = \sqrt{\Gamma_e}|gp\rangle\langle ep|$ and $\hat{L}_2 = \sqrt{\Gamma_e}|pg\rangle\langle pe|$ due to the decay of the intermediate state $|e\rangle$. As shown in [Reiter and Sørensen, 2012] the effective Hamiltonian and Lindblad terms are

$$\hat{H}_{\mathrm{eff}} = -\frac{1}{2}\hat{V}_-[\hat{H}_{\mathrm{NH}}^{-1} + (\hat{H}_{\mathrm{NH}}^{-1})^\dagger]\hat{V}_+ + \hat{H}_e \tag{6.6}$$

$$\hat{L}_{\mathrm{eff}}^k = \hat{L}_k \hat{H}_{\mathrm{NH}}^{-1}\hat{V}_+. \tag{6.7}$$

Applying these formulas to our system we find expressions for three different coupling terms of which $J_{\mathrm{eff}}|gp\rangle\langle pg|$ describes a coherent effective exchange interaction, $\Gamma_{\mathrm{eff}}|gp\rangle\langle pg|$ an incoherent hopping term and $\gamma_{\mathrm{eff}}|gp\rangle\langle gp|$ an irreversible dephasing, where both decoherence mechanisms originate from the decay of the intermediate state $|e\rangle$. The generalization from the above described pair system to a system comprised of N sites can be achieved by applying the effective operators to each pair within the entire system.

The two-level system can be mapped onto a spin system where $|p\rangle$ corresponds to spin up and the dressed state $|g\rangle$ to spin down. The effective Hamiltonian for a system comprised of N sites and using the spin raising and lowering operators $\hat{S}_+$ and $\hat{S}_-$ then reads as

$$\hat{H}^{\mathrm{eff}} = \sum_{k>j} J_{\mathrm{eff}}^{(j,k)}(\hat{S}_+^k\hat{S}_-^j + \hat{S}_+^j\hat{S}_-^k) \tag{6.8}$$

and the effective Lindblad operators for each site j

$$\hat{L}_j^{\mathrm{eff}} = \sum_{k\neq>j} \sqrt{\Gamma_{\mathrm{eff}}^{(j,k)}}\hat{S}_+^k\hat{S}_-^j + \sqrt{\gamma_{\mathrm{eff}}^{(j,k)}}\hat{S}_+^k\hat{S}_-^k. \tag{6.9}$$

The effective coupling coefficients turn out to have the simple form

$$J_{\mathrm{eff}}^{(j,k)} = \frac{1}{2}\frac{KV(j,k)}{1+V(j,k)^2} \tag{6.10}$$

$$\Gamma_{\mathrm{eff}}^{(j,k)} = \frac{KV(j,k)^2}{(1+V(j,k)^2)^2} \tag{6.11}$$

$$\gamma_{\mathrm{eff}}^{(j,k)} = \frac{-KV(j,k)^4}{(1+V(j,k)^2)^2} \tag{6.12}$$

where we have defined $K = \Omega_p^2/\Gamma_e$ and $V(j,k) = V_{dd}(j,k)/(\Omega_c^2/(2\Gamma_e)) = (R_{ip}/|R_j - R_k|)^3$. These two quantities can be recognized as the two-level photon scattering rate and the interaction strength scaled by the EIT bandwidth, respectively. We find that K simply defines an overall timescale for the evolution since it influences all three coupling constants simultaneously. This result confirms our experimental finding from the previous section on the linear dependence between the diffusion coefficient and Ω_p^2 (see fig. 6.3). The interaction strength V is responsible for the competition between coherent and incoherent processes.

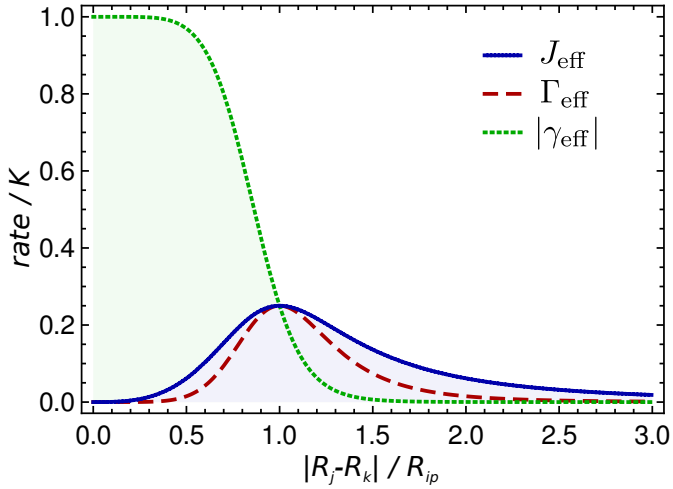

Figure 6.5: Effective couplings as a function of interparticle distance $|R_j - R_k|$. The effective couplings are scaled with the two-level scattering rate K, the distance is given in units of R_{ip}. At short distances the Rydberg blockade leads to enhanced photon scattering corresponding to a large dephasing rate γ_{eff}, and at the same time it leads to a reduced Rydberg state admixture thereby reducing the hopping rates. Therefore we expect the dynamics to be dominated by dephasing at short distances, while at large distances it is dominated by coherent hopping.

Plotting the effective coupling rates as given in eqs. 6.10-6.12 as a function of distance we find the different contributions dominating in different regimes (see fig. 6.5). For short distances spin exchange is suppressed due to the Rydberg blockade which suppresses the Rydberg population of the second atom, while at large distances the exchange rate follows the R^{-3} behavior of the dipolar interaction. In between we find a maximum at $|R_j - R_k| = (2\Gamma_e C_3/\Omega_c^2)^{1/3}$ for both the coherent as well as the incoherent hopping rate where $J_{\text{eff}} = \Gamma_{\text{eff}} = K/4$. At small distances the photon scattering increases, causing strong dephasing in this regime.

From the behavior of the coupling coefficients we expect three different regimes:

for $V \ll 1$, coherent hopping dominates, whereas for $V \approx 1$ coherent and incoherent hopping are equally important, leading to classical transport. For $V \gg 1$, i.e. in the strong blockade regime, the coherent dynamics is suppressed due to the large dephasing, leaving incoherent hopping as the dominant process.

6.3.1 Numerical simulations

Using the effective couplings from eqs. 6.10-6.12 we can perform numerical simulations of the transport dynamics on a one-dimensional chain of up to 101 atoms. We set the intersite spacing a as well as the two-level photon scattering rate K to 1 and vary the typical scaled next-neighbor interaction $C = V(a = 1) = 2\Gamma_e C_3/\Omega_c^2$. Fig. 6.6 shows the probability to find the impurity at site j for different values of C. When the range of the interaction is small as compared to the intersite spacing, i.e. $C \ll 1$, we expect coherent evolution. In this case we find the impurities spread ballistically as expected for coherent dynamics on a regular lattice (see fig. 6.6 a). For $C \approx 1$ the coherent and incoherent hopping are equally important, resulting in a classical diffusion of impurities (fig. 6.6 b). $C \gg 1$ corresponds to a regime where many sites are within the blockade radius R_{ip} which leads to strong dephasing. As a result we find a preferred hopping distance as can be seen from fig. 6.6 c with an overall diffusive expansion.

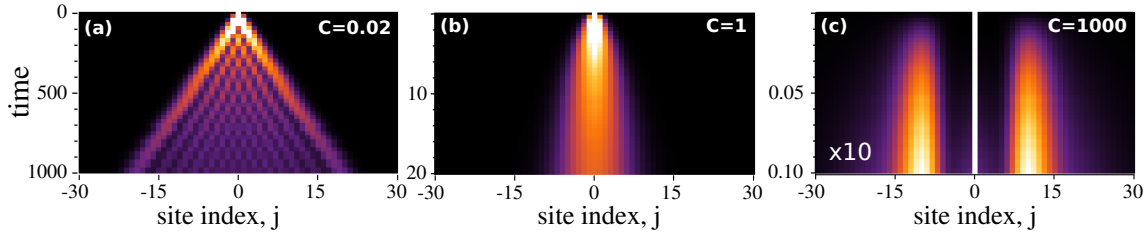

Figure 6.6: Simulations of the transport dynamics on a regular 1D chain. a)-c) shows the probability to find the impurity on a specific site as a function of time in different regimes of the next-neighbor interaction strength C. We find ballistic expansion for $C = 0.02$ where the coherent hopping dominates, whereas for $C = 1$ the dephasing leads to classical diffusion. $C = 1000$ results in a preferred hopping distance.

6.3.2 Including disorder

To study the type of transport observed in the experiment we include the effect of random atom positions to the simulations, which corresponds to off-diagonal disor-

der, i.e. a statistical distribution of coherent coupling rates. We simulate various degrees of decoherence and disorder and find that the degree of disorder only influences the dynamics in the coherent regime where we find a transition from ballistic expansion to an almost localized regime. In contrast, in the incoherent regime the degree of disorder does not influence the dynamics. This finding can be understood from the fact that static disorder of sites has the same effect on the system dynamics as dephasing, i.e. random fluctuations in the coupling terms, when looking at ensemble averages. In the limit of weak interactions ($C < 1$) and no disorder ($\eta = 0$) the simulated dynamics compares well with analytic expressions for nearest neighbor exchange including dephasing as derived within the Haken-Reineker-Strobl (HRS) model in the context of Frenkel exciton transport in molecular aggregates [Haken and Reineker, 1972; Haken and Strobl, 1973].

6.3.3 Classical hopping

In the regime $C \gg 1$, where incoherent hopping with rate Γ_{eff} dominates the dynamics, we find classical diffusion and we can derive analytical solutions for the diffusion coefficient. We first integrate Γ_{eff} to calculate a characteristic hopping rate while assuming a homogeneous atomic density n

$$\Gamma_{char} = n \int \Gamma_{\text{eff}}(\vec{r}) d\vec{r}. \tag{6.13}$$

We use $\Gamma_{\text{eff}}(r) = \frac{KV(r)^2}{(1+V(r)^2)^2}$ as taken from eq. 6.11 and $V(r) = (R_{ip}/r)^3$. In the next step we calculate

$$\langle \vec{r}^2 \rangle = \frac{n}{\Gamma_{char}} \int \Gamma_{\text{eff}}(\vec{r}) \vec{r}^2 d\vec{r} \tag{6.14}$$

from which we can extract the characteristic hopping distance $\sqrt{\langle \vec{r}^2 \rangle} = c \cdot R_{ip}$, where the factor c depends on the dimensionality and reads $c = \{\sqrt{3/2}, \sqrt{2}, \sqrt{10/3}\}$ for a $\{1D, 2D, 3D\}$ system. Note that also the characteristic hopping rate depends on the dimensionality of the system. To obtain a diffusion coefficient we multiply the squared characteristic hopping distance with the characteristic hopping rate following the usual definition

$$D = \frac{1}{2} \langle \vec{r}^2 \rangle \Gamma_{char}. \tag{6.15}$$

Alternatively we directly integrate

$$D = \frac{1}{2} n \int \Gamma_{\text{eff}}(\vec{r}) \vec{r}^2 d\vec{r}. \tag{6.16}$$

The result differs from the simple model used in [Günter *et al.*, 2013], in particular it depends on the atomic density as well as on the dimensionality of the system and reads

$$D_{1D} = \frac{\pi K n_{1D} R_{ip}^3}{12} \tag{6.17}$$

$$D_{2D} = \frac{2\pi^2 K n_{2D} R_{ip}^4}{9\sqrt{2}} \tag{6.18}$$

$$D_{3D} = \frac{5\pi^2 K n_{3D} R_{ip}^5}{9} \tag{6.19}$$

where n_{1D}, n_{2D} and n_{3D} are the atomic 1D-, 2D- and 3D-densities of the system. From the equations we see that the relation between R_{ip} and the typical interatomic separation determines the diffusion coefficient. Note that depending on the dimensionality d these values are to be scaled by $1/d$ when looking at only one component of the $\langle \vec{r}^2 \rangle$ distribution as we do in our experiments. The dependence on atomic density and dimensionality will be possible to distinguish in future experiments.

6.3.4 Comparison to experimental data

The expression found in eq. 6.19 can be compared to the diffusion coefficient as extracted from fig. 6.2 in case the relevant quantities such as the probe Rabi frequency Ω_p, the atomic density n_{3D} as well as the blockade radius R_{ip} are known. It turns out that R_{ip} exhibits the largest uncertainty due to the angular dependence of the dipolar interaction. Therefore we introduce an effective interaction strength $C_3^{(\mathrm{eff})}$, which is not known a priori. The transport experiments presented in Ch. 6.2 were performed in the absence of a quantization field. In addition the polarization of the excitation beams was such that the initial population was distributed over the Zeeman states $m_j = \pm 1/2$ of the state $48S_{1/2}$. Both are coupled to the two Zeeman states of $48P_{1/2}$. As a consequence four Zeeman states are coupled together, where the respective transitions can have a different strengths and the relative contributions of the different transitions are unknown. Therefore, as mentioned above, the effective interaction strength cannot be theoretically calculated, however, it can be determined from the experimental data. Using eq. 6.19 (i.e. assuming 3D diffusion) and the measured diffusion coefficient $D = 153\mu\mathrm{m}^2/\mu\mathrm{s}$ we find $R_{ip} = 5\mu\mathrm{m}$ and thus $C_3^{(\mathrm{eff})} = 2\pi \times 0.53\,\mathrm{GHz}\ \mu\mathrm{m}^3$ (since $\Omega_c \approx 2\pi \times 7.2\,\mathrm{MHz}$ and $\Omega_c \approx 2\pi \times 0.8\,\mathrm{MHz}$). This value is an order of magnitude smaller than the value $C_3 = 2\pi \times 5.2\,\mathrm{GHz}\ \mu\mathrm{m}^3$ calculated from the radial dipole matrix element while ignoring the spatial orientation. This reduction seems surprisingly high, however, we find comparable numbers

for $C_3^{(\mathrm{eff})}$ when investigating the damping of microwave Rabi oscillations as will be discussed in Ch. 7.

From eq. 6.19 we also find that the diffusion coefficient is proportional to the photon scattering rate $K = \Omega_p^2/\Gamma_e$, which therefore defines an overall timescale of the dynamics. This finding is consistent with the predictions of the simple model, and is confirmed by our experimental data shown in fig. 6.3.

To summarize we have seen that a rigorous description as introduced here is indeed required to understand the transport dynamics, since e.g. in the simple model sketched in Ch. 6.1 the process of incoherent hopping is not captured at all. The same holds for the dependence on the atomic density.

6.3.5 Engineering the transition between coherent and classical dynamics

The effective operator model predicts that the parameter $V = 2\Gamma_e V_{dd}/\Omega_c^2$ allows for tuning between different transport regimes, leaving the dipolar interaction strength C_3 and the coupling Rabi frequency Ω_c as experimentally adjustable parameters. Changing C_3 involves changing the Rydberg states, whereas Ω_c can be easily tuned, with the available laser power being the only limitation. A possible transition from coherent to classical transport could therefore be realized using the following parameters and settings. The atoms should prepared in an optical lattice with lattice constant $a = 2\mu$m and be dressed with the Rydberg probe state $|20s\rangle$, while the impurity is in state $|19p\rangle$. With the couplings strengths of the dressing lasers $\Omega_c = 2\pi\times 80\,\mathrm{MHz}$ and $\Omega_c = 2\pi \times 10\,\mathrm{MHz}$, we calculate $V = 0.02$, corresponding to a regime where the coherent coupling with an effective exchange rate $J_{\mathrm{eff}} = 2\pi \times 150\,\mathrm{kHz}$ dominates. As a consequence the impurity will spread ballistically. In contrast, with $\Omega_c = 2\pi \times 10\,\mathrm{MHz}$ and $\Omega_p = 2\pi \times 2\,\mathrm{MHz}$ we access the classical regime with $V = 1$, resulting in a diffusive expansion. With the laser power currently available $\Omega_c = 2\pi \times 80\,\mathrm{MHz}$ is a challenge and requires working at low principal quantum numbers. Coupling to $|20s\rangle$ is a trade-off between reasonable coupling strength and sufficiently a long lifetime of the Rydberg state.

6.4 First studies of coherent transport

Our experiment provides the possibility to explore the transition from coherent to classical transport. As predicted by our simple model and confirmed by the effective operator model the decoherence is caused by photon scattering during the imaging.

Naively one could think that the transition to a coherent regime could be realized by simply reducing Ω_p, however, Ω_p not only affects the dephasing rate but it also modifies the coherent exchange rate by changing the Rydberg state admixture of the dressed probe atoms.

6.4.1 Experimental realization

To overcome the decoherence induced by the imaging process we now perform pulsed experiments. We turn on the EIT fields for a short time to prepare Rydberg atoms, which act as hopping partners for the impurities. After a variable evolution time we switch on a short imaging pulse to determine the spatial extent of the impurities. While the EIT fields are off no photons are scattered, thus the system evolves coherently during this period. Only during the final imaging period of $5\,\mu$s and during the initial preparation of hopping partners, where the EIT fields are on, the system evolves classically. For comparison we have on the same system performed the measurements shown in fig. 6.2 where we vary the exposure time to monitor the classical evolution. By comparing the field ionization signals of the Rydberg population we have made sure that the amount of hopping partners created during the short partner excitation pulse of $2\,\mu$s for the coherent evolution is the same as during the classical evolution. Thus the coherent hopping rate should be the same, which allows us to compare both datasets directly.

Fig. 6.7 shows the dynamics of the coherent evolution (red circles) as compared to the same experiment under permanent projection, i.e. classical dynamics (blue circles). We excite impurities in the state $50S$ and image using the state $48S$, i.e. the transport process is the same as discussed in Ch. 6.2. Namely the off-resonant coupling to the pair state $|48P, 49P\rangle$ leads to a production of $48P$ atoms which can undergo resonant exchange with $48S$ atoms. In the coherent case the time axis reflects the coherent evolution time between the excitation of hopping partners and imaging. In the classical case the time axis reflects the exposure time, i.e. the classical evolution time. Here we find σ_x^2 to grow linearly with time as discussed in Ch. 6.2. This data set is the same as already shown in fig. 6.2. In contrast, when the system evolves coherently, we find σ_x^2 to not grow significantly. This finding reflects an extreme slow-down of the transport dynamics and can at this stage not be distinguished from an Anderson type localization [Anderson, 1958], which one might expect due to the disordered arrangement of the Rydberg dressed atoms. However, as shown in [Robicheaux and Gill, 2014; Weimer, 2014], interactions with a $1/R^3$ dependence as the dipolar interaction studied here do in 3D geometries

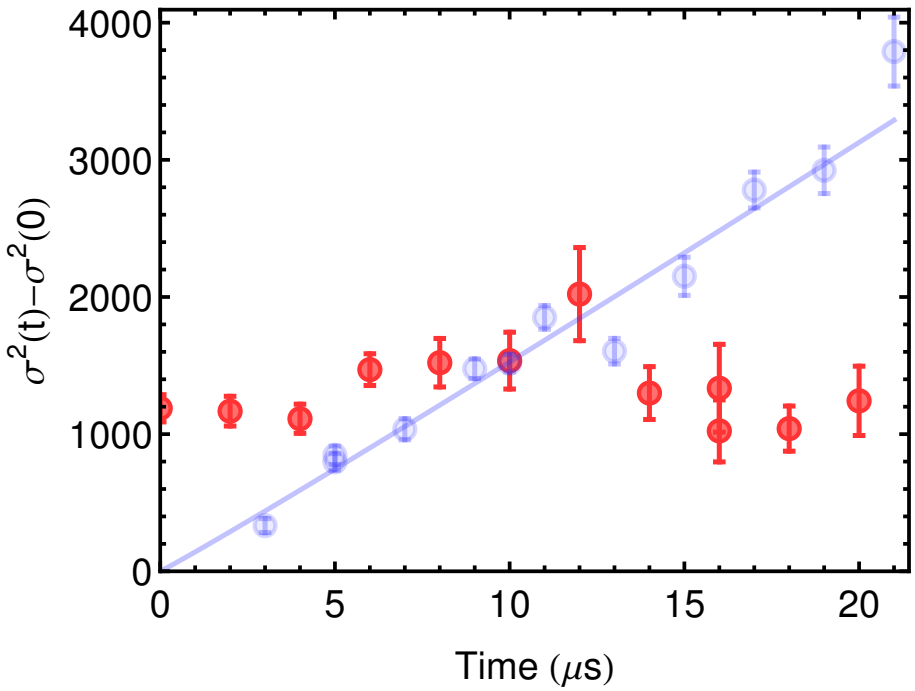

Figure 6.7: Transport dynamics under permanent projection (blue circles) and in the case of free coherent evolution (red circles). In the classical case (blue circles) the time axis reflects the exposure time of the interaction enhanced imaging (this dataset has been shown before in fig. 6.2). For the coherent evolution (red circles) the time axis specifies the time between the excitation of hopping partners and the time where we start to acquire an image (with a fixed exposure time of 5 μs). In this case we find that the size of the distribution of impurities does not increase significantly with time but is mainly determined by the classical expansion during the 5 μs imaging period. The size σ_x is extracted from averages over 100 repeats of the same experiment, the errorbars are obtained by resampling from these 100 repeats.

result in a a slow-down of the transport dynamics, but not in localization, except possibly for very large randomness [Robicheaux and Gill, 2014]. In contrast, in a 1D geometry localization is expected to be triggered even by small amounts of randomness [Robicheaux and Gill, 2014].

6.4.2 Engineering decoherence using a third Rydberg state

In the experiments described above several relevant processes were coupled together, making it hard to vary e.g. the degree of decoherence independent of the coherent dynamics and the image quality. In Ch. 6.3 we have seen that we can have some

control over the amount of dephasing by varying either the interaction strength C_3 or the EIT linewidth via the coupling Rabi frequency Ω_c. Ideally, however, the imaging, the coherent coupling and the degree of decoherence would have to be disentangled in future experiments in order to study their influence in a more controlled way. To this end different Rydberg states could be made use of for the different requirements: as mentioned in Ch. 6.3 the impurities should be in a Rydberg state nP in order to realize a clean and field-independent exchange process with hopping partners in the Rydberg state nS. The same state nS can be used for interaction enhanced imaging when the exposure time is chosen short enough such that the transport during imaging can be neglected. The missing part is thus a way to introduce controllable decoherence.

As we have seen the interaction enhanced imaging scheme itself is a suitable way to introduce decoherence of the many-body quantum state by causing conditional photon scattering. Thus we can set up an additional EIT scheme, but not with the aim to actually measure an absorption signal but to introduce conditional photon scattering in order to decohere the many-body quantum state. This additional EIT scheme would ideally not feature transport due to exchange interactions, therefore the Rydberg state $n'S$ for this additional EIT scheme would be chosen to couple less strongly to the impurity Rydberg state. Varying the probe Rabi frequency of this EIT scheme would allow to tune the dephasing rate independently. Following this approach the decoherence can be decoupled from the imaging process as well as from the coherent exchange rate. In order to preserve a clean image the excitation of impurities as well as the preparation of hopping partners and the controlled dephasing would have to be realized in a spatial direction different from the imaging axis. With the two Rydberg excitation lasers and the microwave source currently available at the experiment the three required Rydberg states nS, nP and $n'S$ can all be coupled to, allowing for the independent realization of the different mechanisms discussed above.

6.5 Prospects

While we have experimentally realized the two limiting cases characterized by strong decoherence and minimal decoherence by switching off the dressing laser fields, respectively, the transition between these two regimes still has to be realized. Interestingly, theoretical work in the context of energy transport in biological systems has predicted an optimum of the transport efficiency for dephasing rates which are

on the order of the coherent couplings [Plenio and Huelga, 2008; Rebentrost *et al.*, 2009b]. Using one of the schemes proposed before, these predictions can be tested in future experiments.

In the coherent regime the role of disorder in the system is of particular interest. While the distribution of probe Rydberg excitations is to a certain extent correlated due to the blockade, the distribution of ground state atoms in the experiments presented here was fully random. This could be changed in future experiments by loading the atoms into an optical lattice. As discussed in Ch. 6.3 the behavior in the coherent regime depends strongly on the degree of disorder, making the transition from ballistic expansion on a lattice to an extreme slow-down in a disordered system. Technically, these experiments should be performed using Rydberg P states as impurities in order to restrict the possible transport channels to exclusively $|nS, nP\rangle \leftrightarrow |nP, nS\rangle$. In order to avoid effects of the anisotropic interactions the experiments should be performed in low-dimensional systems combined with fields to align the dipoles.

Another interesting aspect of our particular system is the possibility to engineer non-Markovian couplings to the environment, i.e. couplings with a finite correlation time. In the context of energy transport the effect of non-Markovian dynamics has been investigated by e.g. [Rebentrost *et al.*, 2009a; Ishizaki and Fleming, 2009; Thorwart *et al.*, 2009; Chin *et al.*, 2010]. In our system this type of decoherence could be realized by slowing down the EIT dynamics. When detuning from the intermediate state with the EIT lasers the populations do not follow almost instantaneously as it is the case for resonant coupling. Instead the population redistribution between $|g\rangle$, $|e\rangle$ and $|s\rangle$ is slowed down, thereby providing the environmental degrees of freedom with some memory.

With the system discussed here and with the proposed improvements to it we have a model system at hand, to which we can map other systems which are of large interest in different communities. With the degree of control possible in cold atom systems, together with the particular properties of Rydberg states, it will be possible to test and possibly to extend the theoretical models which are currently on the market such as the Haken-Reineker-Strobl (HRS) model [Haken and Reineker, 1972; Haken and Strobl, 1973] which is extensively used to describe exciton transport in molecular aggregates.

Chapter 7

Dipolar exchange in microwave driven Rydberg systems

With the two-photon excitation scheme as described in Ch. 2.3.2 it is only possible to excite Rydberg S and D states due to selection rules. However, using an additional microwave photon allows for the excitation of e.g. Rydberg P states, which would benefit the realization of the energy transport experiments with direct S-P exchange. In this Chapter I will present spectroscopic data of microwave transitions between Rydberg states (Ch. 7.1). Sitting on the resonance and varying the microwave pulse duration we observe coherent Rabi oscillations of the population between S and P states (Ch. 7.2). In Ch. 7.3 we study the transition to the interacting regime where the Rabi oscillations are strongly damped.

7.1 Microwave coupling between Rydberg states

In our experiments the microwave radiation is obtained from a synthesizer (Anritsu MG3697C) with controlled power, frequency and pulse duration. It is tunable over a range from 500 MHz to 65 GHz. As we presently do not have an antenna which works for the range of frequencies required we simply use the output connector of a semi-rigid coaxial cable which is designed for frequencies up to 65 GHz, and which we point towards the atoms through a viewport of the vacuum chamber. The resulting polarization of the microwave field is unknown and the field distribution at the position of the atoms can only be measured by using the Rydberg atoms as a probe.

7.1.1 State sensitive detection

To detect the Rydberg nP state population we first apply a short laser pulse resonant with the nS to $5P$ transition in order to deexcite the nS atoms before we field ionize the remaining Rydberg nP atoms. The population of the nP is not affected by the deexcitation laser pulse. Fig. 7.1 shows the amount of detected Rydberg atoms as a function of the deexcitation pulse duration using the Rydberg states $48S$ and $48P$. The red curve is obtained from $48S$ state excitation and subsequent deexcitation, whereas for the blue curve part of the Rydberg atoms have been transferred to $48P$ using a resonant microwave pulse. These atoms can thus not be deexcited and the initial decay is only due to remaining $48S$ state atoms. For $t \geq 1\mu$s we obtain a contrast of typically $1:5-1:10$ which we use for detection of the nP state population. In other experiments we have obtained even better contrasts of up to $1:20$.

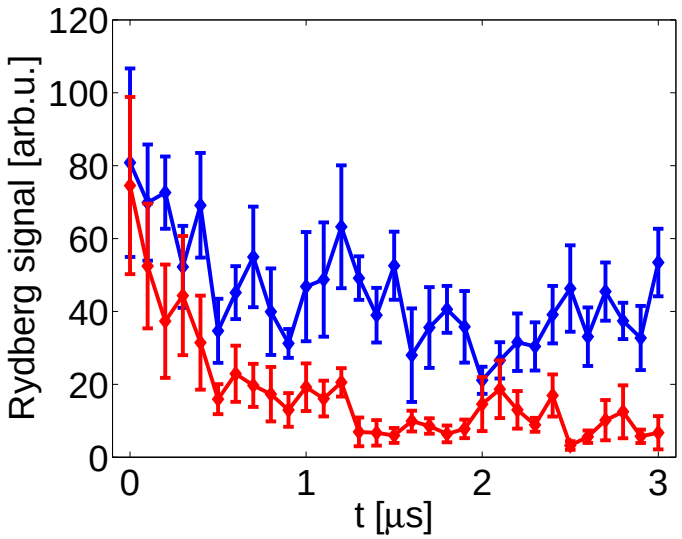

Figure 7.1: Deexcitation of $48S$ state atoms using a resonant 480 nm laser pulse. The red diamonds show data obtained after excitation of $48S$ atoms and subsequent deexcitation, while for the blue diamonds a microwave pulse was used to transfer part of the $48S$ atoms into the state $48P$ before deexcitation. The difference between the two curves provides the possibility to selectively detect $48P$ atoms.

7.1.2 Microwave spectroscopy

Fig. 7.2 shows a scan of the microwave frequency over a range covering the transitions from the state $48S_{1/2}$ to both $48P_{1/2}$ as well as $48P_{3/2}$ which is obtained by

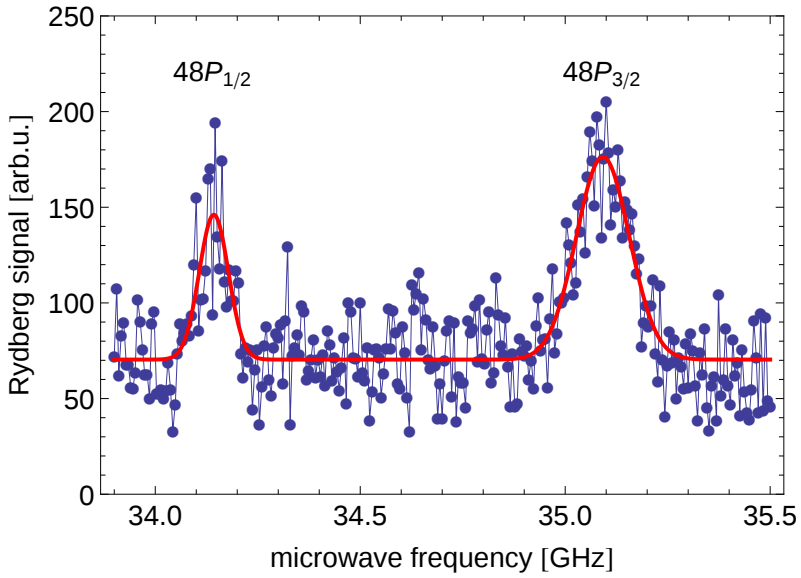

Figure 7.2: Microwave frequency scan around the transition $48S$ to $48P$. The spectrum is obtained using a three-photon scheme to excite Rydberg P states, followed by a depletion of the $48S$ state using a resonant deexcitation laser. Note that the resonances are broadened due to Rydberg interactions.

applying the above described deexcitation scheme. The measured resonance frequencies of (34.143±0.004) GHz ($48P_{1/2}$) and (35.092±0.004) GHz ($48P_{3/2}$) are close to calculated values based on the quantum defects as measured in [Li *et al.*, 2003] (34.145 GHz and 35.077 GHz, respectively). Due to the imperfect deexcitation the spectrum shows an offset caused by remaining $48S$ atoms. Note that the resonances shown in fig. 7.2 are broadened due to Rydberg interactions (see also [Park *et al.*, 2011]).

By working at low atomic densities and low microwave powers we can improve the spectral resolution since broadening due to Rydberg interactions as well as power broadening are reduced. Fig. 7.3 shows a finer scan around the transition from $48S_{1/2}$ to $48P_{3/2}$. The three peaks correspond to three Zeeman states of the $48P_{3/2}$ state which are accessible from the initially prepared state $|48S_{1/2}, m_j = +1/2\rangle$ as sketched in fig. 7.4. Namely we can drive transitions to the Zeeman states $|48P_{3/2}, m_j = +3/2\rangle$, $|48P_{3/2}, m_j = +1/2\rangle$ and $|48P_{3/2}, m_j = -1/2\rangle$. The fitted microwave resonance frequencies are (35.0698±0.0002) GHz, (35.07510±0.00010) GHz and (35.08027±0.00008) GHz. From the measured Zeeman splitting of 5.2 MHz and the Landé factors g_j ($g_j = 4/3$ for $48P_{3/2}$ and $g_j = 2$ for $48S_{1/2}$) we determine the magnetic field to be 3.7 G.

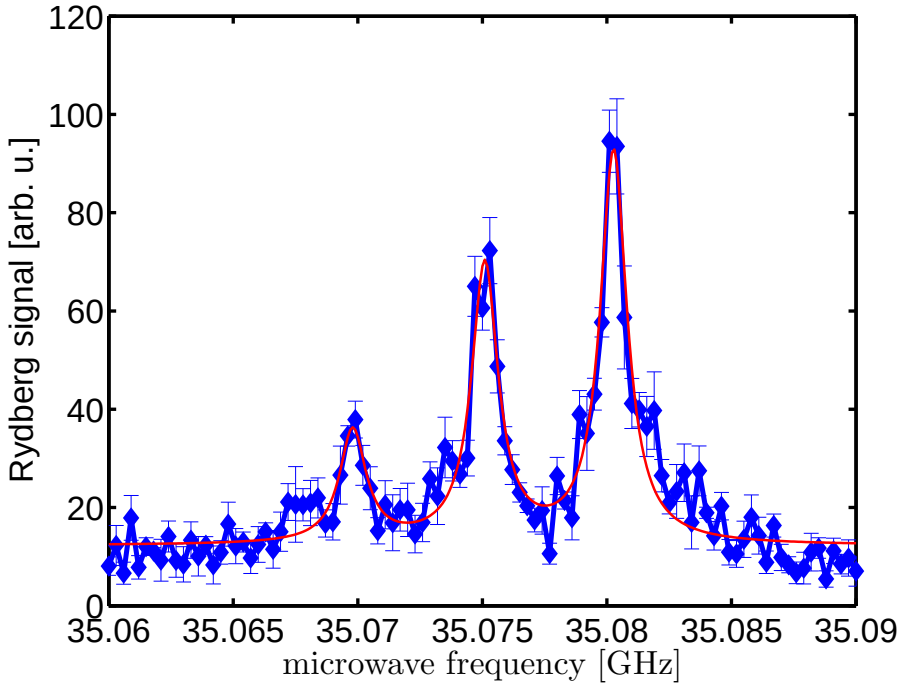

Figure 7.3: Microwave frequency scan around the transition $48S_{1/2}$ to $48P_{3/2}$. Due to the applied magnetic field of 3.7 G the three Zeeman transitions are clearly resolved. Starting from the state $|48S_{1/2}, m_j = +1/2\rangle$ we can drive the transitions as sketched in fig. 7.4 with our unpolarized microwave field. The fitted microwave frequencies are (35.0698±0.0002) GHz, (35.07510±0.00010) GHz and (35.08027±0.00008) GHz.

7.2 Observation of microwave Rabi oscillations

In a next step we tune the microwave frequency to be resonant with the transition $|48S_{1/2}, m_j = +1/2\rangle$ to $|48P_{3/2}, m_j = +3/2\rangle$, and after laser excitation of the state $|48S_{1/2}, m_j = +1/2\rangle$ we apply a microwave pulse of variable duration. To isolate a single transition we increase the magnetic field to 6.4 G. At low densities of Rydberg S atoms we observe Rabi oscillations of the populations between $|48S_{1/2}, m_j = +1/2\rangle$ and $|48P_{3/2}, m_j = +3/2\rangle$ with a high degree of coherence as shown in fig. 7.5. The slight damping is possibly due to residual interaction effects despite the low densities. Varying the output power of the microwave source results in different oscillation periods. We have also seen Rabi oscillations for the two other Zeeman transitions shown in fig. 7.3 and have determined the relative transition strengths, which are given by the Clebsch-Gordon coefficients and the strength of the microwave field in the different polarizations. We find that in our particular setting the Rabi frequency is the strongest on the σ_+ transition to the Zeeman state $m_j = +3/2$, while the Rabi

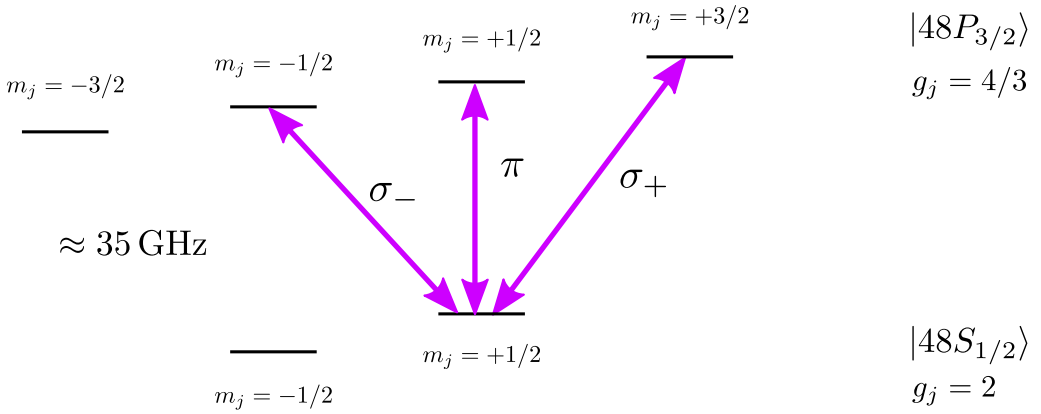

Figure 7.4: Relevant levels for the excitation of Rydberg $P_{3/2}$ state atoms. A microwave field at ≈ 35 GHz couples the states $48S_{1/2}$ and $48P_{3/2}$. In the experiments we initially prepare the atoms in the Rydberg state $|48S_{1/2}, m_j = +1/2\rangle$. Starting from here the three indicated transitions are possible due to selection rules. Since our microwave field contains contributions from different polarizations we drive all three transitions.

frequencies to $m_j = +1/2$ (π transition) and $m_j = -1/2$ (σ_- transition) are reduced by factors of 1.5 and 5, respectively.

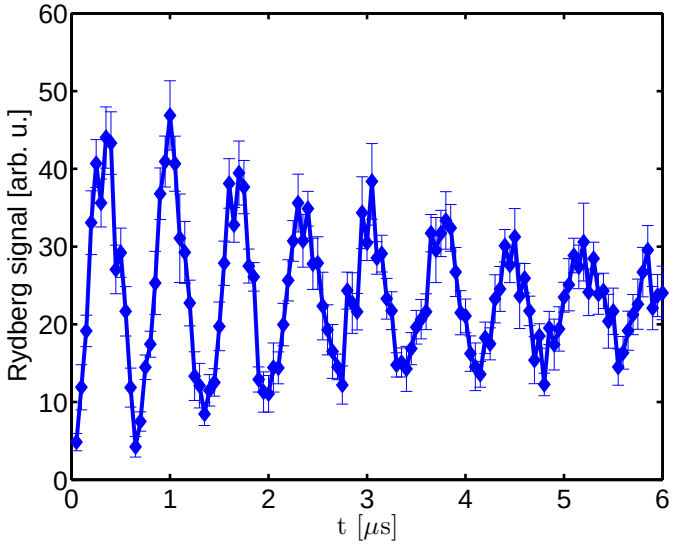

Figure 7.5: Rabi oscillations between $|48S_{1/2}, m_j = +1/2\rangle$ and $|48P_{3/2}, m_j = +3/2\rangle$ at low initial S state population. The estimated Rabi frequency is 1.48 MHz.

When working with higher Rabi frequencies and smaller magnetic fields we find beating effects in the oscillations which are due to off-resonant coupling to the other

Zeeman states. To avoid this one could use a designated microwave antenna which emits radiation of a well-defined polarization and can thus only couple to a single Zeeman state. Here instead we apply a magnetic field of 6.4 G to better isolate the different transitions, and work at a Rabi frequency of 1.48 MHz where the coupling to the other Zeeman states is small.

7.3 Coherent population transfer between Rydberg states

At high Rydberg densities we expect the dipolar interactions between S and P states to modify the Rabi oscillations. Due to the exchange interaction between various atoms with random interparticle distances the total population oscillation should damp out. A similar effect has been found by investigating the retrieval probability of dark-state polaritons [Maxwell *et al.*, 2013] where instead of a damping in the Rabi oscillations the vanishing photon retrieval probability reflected the interaction induced dephasing. As discussed in [Maxwell *et al.*, 2013] the transition from strong damping to coherent Rabi oscillations is determined by the relation between the microwave Rabi frequency and the exchange rate with the nearest S-state neighbor, which is at high densities given by the S-S blockade radius. Dipolar energy exchange has also been seen as line broadening in very early work on ultracold Rydberg gases [Mourachko *et al.*, 1998; Anderson *et al.*, 1998]. In other work reporting on damped microwave oscillations between Rydberg states this damping was due to electric field inhomogeneities, not due to interparticle effects [Hogan *et al.*, 2012].

Fig. 7.6 shows Rabi oscillations for the states $|48S_{1/2}, m_j = +1/2\rangle$ and $|48P_{3/2}, m_j = +3/2\rangle$ for different densities of ground state atoms. For the smallest densities we find a high degree of coherence with only a minimal damping, while for high densities the oscillations become strongly damped. In an independent measurement we found that the damping is less pronounced for higher microwave Rabi couplings where the exchange rate is smaller as compared to the coherent driving.

To estimate the initial Rydberg S state density n_S we follow two independent approaches presented in the next paragraphs. The first one is based on the measured ground state atom density which, together with the parameters of the laser excitation, allows to calculate the Rydberg density. The second approach uses the number of detected Rydberg atoms and the size of the excitation volume for estimating the Rydberg density.

We excite the $48S$ atoms using an EIT configuration with $\Omega_p = 2\pi \times 1.2\,\mathrm{MHz}$

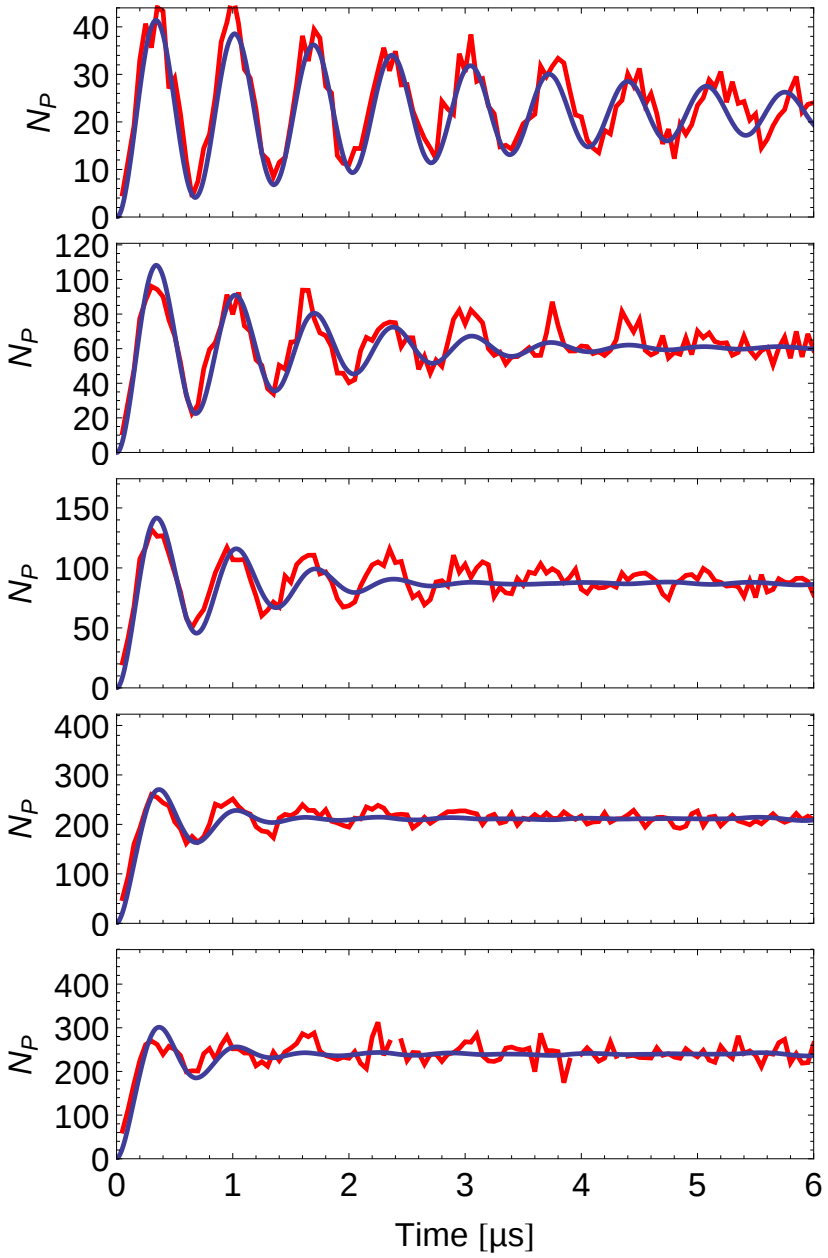

Figure 7.6: Interaction induced dephasing of Rabi oscillations. The measured Rydberg P state population N_P (red curve) is plotted vs. time with different initial Rydberg S state densities n_S. From top to bottom n_S increases, resulting in an increasing absolute population N_P and a damping of the oscillations. The blue curves show simulations of the time evolution in a system comprised of 11 atoms where the product $n_S \cdot C_3$ is a fit parameter.

and $\Omega_{c,\mathrm{peak}} = 2\pi \times 5.2\,\mathrm{MHz}$, resulting in a Rydberg fraction of $\approx \Omega_p^2/\Omega_c^2 \approx 0.05$ at the center of the excitation volume. For each measurement we determine the peak ground state density. To account for the Gaussian distribution of the coupling laser intensity and the atomic density we use average densities which are $(1.3 \times 10^7,\ 9.3 \times 10^8,\ 1.0 \times 10^9,\ 2.5 \times 10^9,\ 3.2 \times 10^9)\,\mathrm{cm}^{-3}$. From these and the Rydberg fraction we determine the Rydberg densities to be $(6.7 \times 10^5,\ 4.9 \times 10^7,\ 5.2 \times 10^7,\ 1.3 \times 10^8,\ 1.7 \times 10^8)\,\mathrm{cm}^{-3}$.

The number of Rydberg atoms is measured using the field ionization signal. The excitation volume can be determined from the spot size of the coupling laser which we measure to be $53\,\mu\mathrm{m} \times 15\,\mu\mathrm{m}$ (Gaussian σ), and the length of the cloud along the excitation beams, which is $92\,\mu\mathrm{m}$. The resulting Rydberg densities of $(1.3 \times 10^7,\ 6.5 \times 10^7,\ 5.0 \times 10^7,\ 1.2 \times 10^8,\ 1.4 \times 10^8)\,\mathrm{cm}^{-3}$ agree within 20% with the values obtained using the first approach (neglecting the first value where the ground state density could not be determined precisely).

We model our experimental data by solving numerically for the time evolution of up to 11 two-level atoms with Rydberg states S and P interacting via dipolar exchange. The background atoms remaining in the ground state are not included in the simulations. The Hamiltonian in a spin language reads

$$H = \frac{\Delta}{2} \sum_i^N S_z^{(i)} + \frac{\Omega}{2} \sum_i^N S_x^{(i)} + \sum_{i,j \neq i}^N \frac{C_3}{|R_i - R_j|^3} S_+^{(i)} S_-^{(j)} \tag{7.1}$$

where $S_x^{(i)}$ and $S_z^{(i)}$ are the Pauli spin matrices and $S_\pm^{(i)} = 1/2(S_x^{(i)} \pm i S_y^{(i)})$ the rising and lowering operators of site i. Δ is the detuning and Ω the coupling strength of the microwave field. R_i is the position of the ith atom. The initial state is with all atoms in the S state with positions randomly distributed in a box with periodic boundary conditions. The interactions between S state atoms are only indirectly included in the construction of the initial spatial distribution of S Rydberg atoms by excluding positions within the blockade radius of another atom. However, for the parameters discussed here the blockade of S state atoms plays only a minor role. Solving numerically for the time evolution at different Rydberg S atom densities we can reproduce our experimental data by fitting one parameter $U = n_S \cdot C_3$ where n_S is the Rydberg S state density and C_3 the dipolar interaction coefficient. $n_S \cdot C_3$ defines the typical timescale of a single coherent exchange, thus determining the damping time of the oscillations. The results of the simulations are shown in fig. 7.6 and agree very well with the experimental data. The fitted value of $n_S \cdot C_3$ as compared to the measured equilibrium Rydberg signal exhibits a linear dependence as shown in fig. 7.7, indicating that the Rydberg S state densities are still so small that

interaction effects between S state atoms do not result in a saturation of Rydberg population. This is supported by comparing the *measured* Rydberg signal at long times (reflecting 50% of the initial S state population) to the corresponding ground state atom density, where we also find a linear increase.

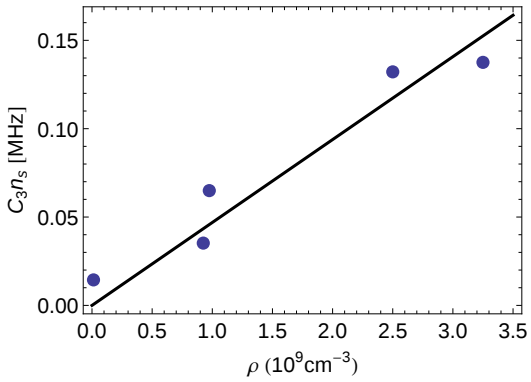

Figure 7.7: The linear increase of the fitted product $C_3 \cdot n_S$ with the average ground state density ρ indicates that interactions between Rydberg S state atoms do not play a major role.

The expected dipolar interaction strength between the states $48S$ and $48P$ is given by C_3/R^3, where $C_3 = 2\pi \times 5.2\,\mathrm{GHz}\ \mu\mathrm{m}^3$ based on the radial matrix element of the transition (see e.g. [Walker and Saffman, 2008]). This number, however, does not capture the angular dependence of the interaction potential. To account for the experimental details we introduce an effective interaction strength $C_3^{(\mathrm{eff})}$ which can be smaller than the value specified above, depending on the Clebsch-Gordan coefficients as discussed in [Park *et al.*, 2011]. In order to determine the effective interaction strength experimentally we use the product $n_S \cdot C_3^{(\mathrm{eff})}$ as obtained from fitting the damped Rabi oscillations, as well as the Rydberg S state density n_S which we estimate independently as described above. We find $C_3^{(\mathrm{eff})} = 2\pi \times (1 \pm 0.1)\,\mathrm{GHz}\ \mu\mathrm{m}^{-3}$ where the uncertainty is due to the uncertainty of the Rydberg density n_S.

Both the transport experiments, where the effective interaction strength was inferred from a diffusion coefficient (Ch. 6.3), as well as the damping of the Rabi oscillations described here, indicate that $C_3^{(\mathrm{eff})}$ is significantly smaller than its maximum value $C_3 = 2\pi \times 5.2\,\mathrm{GHz}\ \mu\mathrm{m}^3$ as calculated when neglecting the angular dependence.

Comparing the two experimentally obtained numbers directly we find approximately a factor of 2 difference ($C_3^{(\mathrm{eff})} = 2\pi \times 0.53\,\mathrm{GHz}\ \mu\mathrm{m}^{-3}$ from the transport experiments). However, since the experimental conditions as well as the involved

states were slightly different, we do not expect these values to perfectly agree. There are two main differences between the two experiments: the microwave Rabi oscillations were carried out at a magnetic field of 6.4 G due to which the involved levels $|48S_{1/2}, m_F = +1/2\rangle$ and $|48P_{3/2}, m_F = +3/2\rangle$ were well isolated. In contrast the transport experiments were carried out without a quantization field and the initial population was distributed over the two Zeeman states of $|48S_{1/2}\rangle$. As a consequence energy exchange can occur with four different Zeeman states being involved, where the overall dynamics results from averaging over the different transitions. The second difference is that the P state initially populated in the fission process prior to transport is $|48P_{1/2}\rangle$, while the microwave oscillations involved $|48P_{3/2}\rangle$.

For future transport experiments we will use microwave state preparation. In this case the damped microwave Rabi oscillations can be used to calibrate the interaction strength such that it is not a free parameter in the theoretical description of the transport process, thereby allowing to test the predictions of the effective operator model for e.g. the diffusion coefficient (eq. 6.19) independently.

To summarize we have investigated microwave Rabi oscillations in the interacting regime, where coherent dipolar exchange leads to a damping in the oscillations due to the large system size. When modeling our experimental data we find very good agreement, with the product of the dipolar interaction strength and Rydberg density being the only free parameter. This indicates that the experiment can be described by purely coherent dynamics, with dephasings originating from the random positions of the atoms. From the product $n_S \cdot C_3^{(\mathrm{eff})}$ and calibrating the Rydberg state density independently, we are able to extract an effective interaction strength $C_3^{(\mathrm{eff})} = 2\pi \times (1 \pm 0.1)\,\mathrm{GHz}\ \mu\mathrm{m}^3$ for the states $|48S_{1/2}, m_F = +1/2\rangle$ and $|48P_{3/2}, m_F = +3/2\rangle$ for our particular system. The control and understanding of the microwave coupling between Rydberg states is a prerequisite for the investigation of energy transport involving Rydberg P states as discussed in Ch. 6.3 and 6.4.

7.4 Prospects

At low densities we have observed clean two-level Rabi oscillations between states nS and nP. These can in the future serve as a sensitive probe for studying the effects of measurement induced decoherence as proposed in Ch. 6.4.2. The experiment we have in mind is to apply an EIT scheme of which the involved Rydberg state $n'S$ is shifted due to the presence of an atom in state nP. The resulting photon scattering constitutes a measurement and thus introduces decoherence. The degree

of decoherence is given by the scattering rate, which depends on the one hand on the number of atoms in the vicinity of an atom in state nP, i.e. on the atomic density. In addition it can be controlled via the single-atom scattering rate, i.e. via the probe Rabi frequency Ω_p of the EIT scheme. Measuring the damping rate of the microwave Rabi oscillations can therefore be a valuable tool to measure and control the degree of decoherence, essential for future transport experiments.

Chapter 8

Conclusion and Outlook

In this thesis we have studied the laser excitation and subsequent evolution of Rydberg interacting atoms in an ultracold atomic gas. The questions we address include: what types of correlations emerge when strong interatomic interactions compete with the driving laser fields? what is the nature of the excitation process that leads to the formation of Rydberg aggregates? and finally how do Rydberg excitations evolve under the influence of strong dipolar interactions with the surrounding atoms? To investigate these questions we established full counting statistics as a method to characterize atomic correlations, and we demonstrated a new imaging technique which makes it possible to sensitively detect Rydberg atoms embedded within an ultracold atomic gas with high spatial and temporal resolution. An interesting common theme of the presented studies is the role of decoherence, which determines the nature of the aggregate formation and crucially affects the character of the dipolar energy transport dynamics.

The experimental apparatus we used for our studies has been constructed during this thesis. It allows for fast loading of ^{87}Rubidium atoms into an optical dipole trap and the possibility to reach the Bose-Einstein-condensation transition in less than 5 s. In addition it features an elaborate electrode structure for electric field compensation as well as field ionization detection of Rydberg atoms.

Our first experiments focused on the excitation of Rydberg atoms using two coherent laser fields. Investigating coherent population trapping in interacting Rydberg systems we have found suppression of the dark state resonance due to these interactions. Following up on this finding we have investigated the optical response of atoms under conditions of electromagnetically induced transparency (EIT) and the associated emergence of dark-state polaritons (DSPs) involving interacting Rydberg states. The strong interactions tend to break the EIT condition, and we were able

to map out the transition from a nearly transparent medium to a strongly absorbing one as the effects of interactions were increased. Complementary to our measurements of the optical response we could measure the "matter-like" part of the DSPs using field ionization detection of the Rydberg population. In the strongly interacting regime we found that the counting statistics become significantly sub-Poissonian indicating the emergence of correlations in the coupled atom-light system.

Next we turned to a detailed study of the Rydberg excitation process using detuned laser fields. Here we observed the formation of Rydberg aggregates, i.e. correlated structures comprised of a few Rydberg excitations. Using the full counting statistics (FCS) of the Rydberg atom number distribution we have established a way to determine the typical aggregate size from the statistical moments. In particular the presence of aggregates results in *enhanced* number fluctuations, in contrast to the suppressed number fluctuations typically attributed to the Rydberg blockade effect. For our experimental settings and using an excitation frequency which is blue detuned by $\approx 20\,\mathrm{MHz}$, we concluded that the aggregates are typically comprised of three atoms. By comparing with rate estimates and many-body simulations we conclude that the aggregate formation is strongly affected by decoherence leading to sequential excitation of individual atoms around an initial off-resonantly excited grain. At the time of this study the precise origin of decoherence was not known, but it seems likely to be dephasing due to the residual motion of the atoms during excitation, which has important implications for the formation of spatially ordered states of Rydberg atoms. While a surprising amount of information can be learned from the FCS, future studies will benefit from the spatial resolution possible with direct imaging methods.

With the application of imaging spatial correlations in mind, we have developed a minimally destructive optical imaging technique which is based on Rydberg state EIT and exploits the surrounding bath of atoms as an amplifier. We have demonstrated this technique experimentally and were able to detect as few as six Rydberg atoms in a single shot image. Besides single shot sensitivity our scheme features state selectivity and excellent spatial and temporal resolution.

Using this imaging scheme we have observed dipolar energy transport due to exchange interactions between different Rydberg states. This transport involves dipolar exchange interactions between a Rydberg impurity and the surrounding optically dressed atoms.

Investigating the observed energy transport dynamics more carefully we found that it can be described by classical hopping due to the effect of decoherence introduced via the continuous optical measurement. As a consequence we observe

diffusive dynamics, with a measured diffusion exponent of 1.04 ± 0.08. Using the Rydberg states $48S_{1/2}$ and $50S_{1/2}$ for probe and impurities, respectively, we expect the direct *ss*-exchange should be strongly suppressed, however transport can still occur due to *sp*-exchange involving the intermediate state $48P_{1/2}$. To better understand the transport dynamics and to quantify the influence of the coherent coupling as well as the decoherence, we set up an effective spin model based on the adiabatic elimination of states. This procedure allows us to find analytic expressions for different coupling constants and to model the dynamics of the energy transport numerically for systems as large as $\gtrsim$100 atoms. In the regime of strong dephasing we find an emergent length scale for excitation hopping determined by the Rydberg blockade radius, and we derive analytic expressions for the diffusion coefficient for different dimensionalities. Our model predicts faster transport than we observed, which can be reconciled by assuming that the effective interaction strength is smaller than the naive estimate using the maximum dipole moment of the states involved. By comparing the measured diffusion coefficient with the theoretical model we infer an effective dipolar interaction strength $C_3^{(\mathrm{eff})} = 2\pi \times 0.53\,\mathrm{GHz}\ \mu\mathrm{m}^3$, which is approximately a factor of 10 smaller than the naive estimate.

There is a natural interest in exploring the transition from classical (diffusive) to coherent dynamics. For this reason we performed an additional experiment in which we allow the system to evolve without the imaging fields, i.e. without continuous projection of the quantum state. In this case we observed an extreme slow-down of the dynamics, which is consistent with the absence of transport. Having realized the limiting cases of purely coherent evolution and classical transport, we elaborate on different approaches which would allow for tuning the degree of decoherence, and on the possibilities of using our system for quantum simulations of biological systems.

As a step towards the further investigation of energy transport we have performed microwave spectroscopy of the transitions between Rydberg $48S_{1/2}$ and $48P_{3/2}$ states. We drive microwave Rabi oscillations between these states and find damping of these oscillations at high densities due to the dipolar exchange process. The damping rate provides an independent estimate of the effective dipolar interaction strength, which is also found to be smaller than the naive estimate, namely we extract $C_3^{(\mathrm{eff})} = 2\pi \times (1 \pm 0.1)\,\mathrm{GHz}\ \mu\mathrm{m}^3$. Finally, we discuss a scheme to study the effects of measurement-induced-decoherence based on coupling microwave driven dipoles to an auxiliary probe atom coupled via EIT.

The experiments presented here open up a variety of interesting questions to be investigated concerning the influence of decoherence and disorder on dipolar energy transport dynamics, as well as on the excitation of correlated or even crystalline

states. For example, reducing the ratio between dephasing rate and coherent coupling will make it possible to reach the regime of coherent aggregate formation. The experimental distinction of the two formation mechanisms based on counting statistics would largely benefit from a better detection efficiency. The interaction enhanced imaging scheme presented here in principle allows for detection efficiencies close to 100%. With improved spatial resolution the excitation dynamics and the structure of the aggregates could even be directly imaged. Also the investigation of crystalline structures [Pohl *et al.*, 2010; Schauß *et al.*, 2014] and quantum phase transitions in laser driven Rydberg systems [Weimer *et al.*, 2008], will benefit from spatially resolved imaging with single atom sensitivity.

Single atom resolution using our interaction enhanced imaging scheme requires further optimization of the experimental parameters, in particular the choice of the involved Rydberg states. For this purpose one should choose Rydberg states for impurity and probing for which energy exchange is strongly suppressed to prevent motion during the imaging exposure. In addition, states with a larger principal quantum number n would reduce the experimental requirements on optical resolution, and the signal of an individual impurity would be less sensitive to atom shot noise. Also the investigation of transport dynamics would benefit from the possibility to spatially resolve single impurities, since this would allow access to the position of individual impurities for investigating the statistical probabilities to find them at certain positions [Mülken *et al.*, 2007].

Another future goal will be the precise engineering of decoherence in Rydberg systems. For example, the lifetime of a Rydberg state can be artificially reduced by coupling it to a short-lived intermediate state, similar to the deexcitation scheme used for state selective detection discussed in Ch. 7. Varying the power of the deexcitation laser thus allows to control the single atom decoherence. This scheme will be valuable, for example, for the further investigation of the role of decoherence on the aggregate formation process.

Future studies of energy transport involving two different Rydberg states may exploit a third "probe" Rydberg state to introduce controlled decoherence. This would make it possible to separate the exchange coupling from the decoherence processes, thus allowing for improved studies of the role of decoherence on dipolar energy transport. Together with the control of disorder in our system, this could be used to model key processes in biological systems such as energy transport in photosynthetic light harvesting complexes (LHCs). An intriguing aspect of energy transport in LHCs is its surprisingly high efficiency, which is in some cases close to 100% [Blankenship, 2008]. Signs of quantum coherence in LHCs has been found

a few years ago (see e.g. [Engel *et al.*, 2007; Lee *et al.*, 2007; Collini *et al.*, 2010; Sarovar *et al.*, 2010]). On the other hand, recent theoretical work has shown that in disordered systems energy transport can be made most efficient by introducing a finite amount of dephasing [Plenio and Huelga, 2008; Chin *et al.*, 2010; Rebentrost *et al.*, 2009b; Zimboras *et al.*, 2013]. Investigating the influence of dephasing on the energy transport dynamics in Rydberg systems in a controlled way and studying the quantum-classical crossover can thus possibly help to answer some of the open questions regarding coherence and decoherence in photosynthetic LHCs.

Bibliography

[Abel *et al.*, 2009] Abel, R. P., Mohapatra, A. K., Bason, M. G., Pritchard, J. D., Weatherill, K. J., Raitzsch, U., and Adams, C. S. (2009). *Laser frequency stabilization to excited state transitions using electromagnetically induced transparency in a cascade system*. Applied Physics Letters **94**, 071107.

[Amthor, 2008] Amthor, T. (2008). *Interaction-Induced Dynamics in Ultracold Rydberg Gases – Mechanical Effects and Coherent Processes*. PhD thesis Universität Freiburg.

[Amthor *et al.*, 2007a] Amthor, T., Reetz-Lamour, M., Giese, C., and Weidemüller, M. (2007a). *Modeling many-particle mechanical effects of an interacting Rydberg gas*. Phys. Rev. A **76**, 054702.

[Amthor *et al.*, 2009] Amthor, T., Reetz-Lamour, M., and Weidemüller, M. (2009). *Cold Atoms and Molecules* chapter Frozen Rydberg Gases, , pp. 147–178. Wiley-VCH.

[Amthor *et al.*, 2007b] Amthor, T., Reetz-Lamour, M., Westermann, S., Denskat, J., and Weidemüller, M. (2007b). *Mechanical Effect of van der Waals Interactions Observed in Real Time in an Ultracold Rydberg Gas*. Phys. Rev. Lett. **98**, 023004.

[Anderson, 1958] Anderson, P. W. (1958). *Absence of Diffusion in Certain Random Lattices*. Phys. Rev. **109**, 1492.

[Anderson *et al.*, 2002] Anderson, W. R., Robinson, M. P., Martin, J. D. D., and Gallagher, T. F. (2002). *Dephasing of resonant energy transfer in a cold Rydberg gas*. Phys. Rev. A **65**, 063404.

[Anderson *et al.*, 1998] Anderson, W. R., Veale, J. R., and Gallagher, T. F. (1998). *Resonant Dipole-Dipole Energy Transfer in a Nearly Frozen Rydberg Gas*. Phys. Rev. Lett. **80**, 249.

[Argus, 2013] Argus, M. (2013). *Electric Field Optimization of a Rydberg Atom Experiment*. Bachelor thesis, Universität Heidelberg.

[Arimondo, 1996] Arimondo, E. (1996). *Coherent Population Trapping in Laser Spectroscopy*. Prog. in Optics **35**, 259.

[Ates *et al.*, 2007] Ates, C., Pohl, T., Pattard, T., and Rost, J. M. (2007). *Antiblockade in Rydberg Excitation of an Ultracold Lattice Gas*. Phys. Rev. Lett. **98**, 023002.

[Ates *et al.*, 2011] Ates, C., Sevinçli, S., and Pohl, T. (2011). *Electromagnetically induced transparency in strongly interacting Rydberg gases*. Phys. Rev. A **83**, 041802.

[Baur *et al.*, 2014] Baur, S., Tiarks, D., Rempe, G., and Dürr, S. (2014). *Single-Photon Switch Based on Rydberg Blockade*. Phys. Rev. Lett. **112**, 073901.

[Bendkowsky *et al.*, 2009] Bendkowsky, V., Butscher, B., Nipper, J., Shaffer, J. P., Löw, R., and Pfau, T. (2009). *Observation of ultralong-range Rydberg molecules*. Nature **458**, 1005 .

[Bergmann *et al.*, 1998] Bergmann, K., Theuer, H., and Shore, B. W. (1998). *Coherent population transfer among quantum states of atoms and molecules*. Rev. Mod. Phys. **70**, 1003.

[Beterov *et al.*, 2009] Beterov, I. I., Ryabtsev, I. I., Tretyakov, D. B., and Entin, V. M. (2009). *Quasiclassical calculations of blackbody-radiation-induced depopulation rates and effective lifetimes of Rydberg nS, nP, and nD alkali-metal atoms with* $n \leq 80$. Phys. Rev. A **79**, 052504.

[Blankenship, 2008] Blankenship, R. E. (2008). *Molecular mechanisms of photosynthesis*. John Wiley & Sons.

[Boisseau *et al.*, 2002] Boisseau, C., Simbotin, I., and Côté, R. (2002). *Macrodimers: Ultralong Range Rydberg Molecules*. Phys. Rev. Lett. **88**, 133004.

[Breuer and Petruccione, 2002] Breuer, H.-P. and Petruccione, F. (2002). *The theory of open quantum systems*. Oxford university press.

[Brion *et al.*, 2007] Brion, E., Pedersen, L. H., and Mølmer, K. (2007). *Adiabatic elimination in a lambda system*. Journal of Physics A: Mathematical and Theoretical **40**, 1033.

[Busche, 2011] Busche, H. (2011). *Efficient loading of a magneto-optical trap for experiments with dense ultracold Rydberg gases.* Diploma thesis, Universität Heidelberg.

[Chin *et al.*, 2010] Chin, A. W., Datta, A., Caruso, F., Huelga, S. F., and Plenio, M. B. (2010). *Noise-assisted energy transfer in quantum networks and light-harvesting complexes.* New Journal of Physics **12**, 065002.

[Clegg, 2009] Clegg, R. M. (2009). *Forster resonance energy transfer – FRET what it is, why do it, and how it's done.* FRET and FLIM Techniques **1**, 1.

[Collini *et al.*, 2010] Collini, E., Wong, C. Y., Wilk, K. E., Curmi, P. M., Brumer, P., and Scholes, G. D. (2010). *Coherently wired light-harvesting in photosynthetic marine algae at ambient temperature.* Nature **463**, 644.

[Comparat and Pillet, 2010] Comparat, D. and Pillet, P. (2010). *Dipole blockade in a cold Rydberg atomic sample.* J. Opt. Soc. Am. B **27**, A208.

[Dalibard *et al.*, 1992] Dalibard, J., Castin, Y., and Mølmer, K. (1992). *Wave-function approach to dissipative processes in quantum optics.* Phys. Rev. Lett. **68**, 580.

[Dieckmann *et al.*, 1998] Dieckmann, K., Spreeuw, R. J. C., Weidemüller, M., and Walraven, J. T. M. (1998). *Two-dimensional magneto-optical trap as a source of slow atoms.* Phys. Rev. A **58**, 3891.

[Diehl *et al.*, 2008] Diehl, S., Micheli, A., Kantian, A., Kraus, B., Büchler, H., and Zoller, P. (2008). *Quantum states and phases in driven open quantum systems with cold atoms.* Nature Physics **4**, 878.

[Dudin and Kuzmich, 2012] Dudin, Y. O. and Kuzmich, A. (2012). *Strongly Interacting Rydberg Excitations of a Cold Atomic Gas.* Science **336**, 887.

[Efron, 1979] Efron, B. (1979). *Bootstrap Methods: Another Look at the Jackknife.* The Annals of Statistics **7**, 1.

[Engel *et al.*, 2007] Engel, G. S., Calhoun, T. R., Read, E. L., Ahn, T.-K., Man**c**al, T., Cheng, Y.-C., Blankenship, R. E., and Fleming, G. R. (2007). *Evidence for wavelike energy transfer through quantum coherence in photosynthetic systems.* Nature **446**, 782.

[Faber, 2011] Faber, A. (2011). *All-optical formation of a Rubidium Bose-Einstein condensate for experiments on interacting Rydberg atoms.* Diploma thesis, Universität Heidelberg.

[Firstenberg *et al.*, 2013] Firstenberg, O., Peyronel, T., Liang, Q., Gorshkov, A., Lukin, M. D., and Vuletic, V. (2013). *Attractive photons in a quantum nonlinear medium.* Nature **502**, 71.

[Fleischhauer *et al.*, 2005] Fleischhauer, M., Imamoglu, A., and Marangos, J. P. (2005). *Electromagnetically induced transparency: Optics in coherent media.* Rev. Mod. Phys. **77**, 633.

[Fleischhauer and Lukin, 2000] Fleischhauer, M. and Lukin, M. D. (2000). *Dark-State Polaritons in Electromagnetically Induced Transparency.* Phys. Rev. Lett. **84**, 5094.

[Fleischhauer and Lukin, 2002] Fleischhauer, M. and Lukin, M. D. (2002). *Quantum memory for photons: Dark-state polaritons.* Phys. Rev. A **65**, 022314.

[Gaëtan *et al.*, 2009] Gaëtan, A., Miroshnychenko, Y., Wilk, T., Chotia, A., Viteau, M., Comparat, D., Pillet, P., Browaeys, A., Grangier, P., et al. (2009). *Observation of collective excitation of two individual atoms in the Rydberg blockade regime.* Nature Physics **5**, 115.

[Gaj *et al.*, 2014] Gaj, A., Krupp, A. T., Balewski, J. B., Löw, R., Hofferberth, S., and Pfau, T. (2014). *Ultracold atom-electron interaction: from two to many-body physics.* arXiv preprint arXiv:1404.5761.

[Gallagher, 1994] Gallagher, T. (1994). *Rydberg atoms.* Cambridge University Press.

[Gardiner and Zoller, 2004] Gardiner, C. and Zoller, P. (2004). *Quantum noise: a handbook of Markovian and non-Markovian quantum stochastic methods with applications to quantum optics* Vol. 56. Springer.

[Gärttner *et al.*, 2013] Gärttner, M., Heeg, K. P., Gasenzer, T., and Evers, J. (2013). *Dynamic formation of Rydberg aggregates at off-resonant excitation.* Phys. Rev. A **88**, 043410.

[Gärttner *et al.*, 2014] Gärttner, M., Whitlock, S., Schönleber, D. W., and Evers, J. (2014). *Semi-analytical model for nonlinear light propagation in strongly interacting Rydberg gases.* arXiv preprint arXiv:1402.4674.

[Gorniaczyk *et al.*, 2014] Gorniaczyk, H., Tresp, C., Schmidt, J., Fedder, H., and Hofferberth, S. (2014). *Single Photon Transistor Mediated by Inter-State Rydberg Interaction.* arXiv preprint arXiv:1404.2876.

[Gorshkov *et al.*, 2013] Gorshkov, A. V., Nath, R., and Pohl, T. (2013). *Dissipative Many-Body Quantum Optics in Rydberg Media.* Phys. Rev. Lett. **110**, 153601.

[Gorshkov *et al.*, 2011] Gorshkov, A. V., Otterbach, J., Fleischhauer, M., Pohl, T., and Lukin, M. D. (2011). *Photon-Photon Interactions via Rydberg Blockade.* Phys. Rev. Lett. **107**, 133602.

[Götz *et al.*, 2012] Götz, S., Höltkemeier, B., Hofmann, C. S., Litsch, D., DePaola, B. D., and Weidemüller, M. (2012). *Versatile cold atom target apparatus.* Review of Scientific Instruments **83**, .

[Greene *et al.*, 2000] Greene, C. H., Dickinson, A. S., and Sadeghpour, H. R. (2000). *Creation of Polar and Nonpolar Ultra-Long-Range Rydberg Molecules.* Phys. Rev. Lett. **85**, 2458.

[Grynberg and Cagnac, 1977] Grynberg, G. and Cagnac, B. (1977). *Doppler-free multiphotonic spectroscopy.* Rep. Prog. Phys. **40**, 791.

[Günter, 2013] Günter, G. (2013). *Interfacing Rydberg atoms with light and observing their interaction driven dynamics.* PhD thesis Universität Heidelberg.

[Günter *et al.*, 2012] Günter, G., Robert-de-Saint-Vincent, M., Schempp, H., Hofmann, C. S., Whitlock, S., and Weidemüller, M. (2012). *Interaction Enhanced Imaging of Individual Rydberg Atoms in Dense Gases.* Phys. Rev. Lett. **108**, 013002.

[Günter *et al.*, 2013] Günter, G., Schempp, H., Robert-de Saint-Vincent, M., Gavryusev, V., Helmrich, S., Hofmann, C. S., Whitlock, S., and Weidemüller, M. (2013). *Observing the Dynamics of Dipole-Mediated Energy Transport by Interaction-Enhanced Imaging.* Science **342**, 954.

[Haken and Reineker, 1972] Haken, H. and Reineker, P. (1972). *The coupled coherent and incoherent motion of excitons and its influence on the line shape of optical absorption.* Zeitschrift für Physik **249**, 253.

[Haken and Strobl, 1973] Haken, H. and Strobl, G. (1973). *An exactly solvable model for coherent and incoherent exciton motion.* Zeitschrift für Physik **262**, 135.

[Heeg *et al.*, 2012] Heeg, K. P., Gärttner, M., and Evers, J. (2012). *Hybrid model for Rydberg gases including exact two-body correlations.* Phys. Rev. A **86**, 063421.

[Helmrich, 2013] Helmrich, S. (2013). *Improving optical resolution by noise correlation analysis.* Master thesis, Universität Heidelberg.

[Hofmann, 2013] Hofmann, C. (2013). *Emergence of correlations in strongly interacting ultracold Rydberg gases.* PhD thesis Universität Heidelberg.

[Hofmann *et al.*, 2014] Hofmann, C., Günter, G., Schempp, H., Robert-de Saint-Vincent, M., Whitlock, S., and Weidemüller, M. (2014). *Combined ion and optical detection of Rydberg atoms in dense ultracold atomic gases.* in preparation.

[Hofmann *et al.*, 2013a] Hofmann, C. S., Günter, G., Schempp, H., Müller, N. M. L., Faber, A., Busche, H., Robert-de-Saint-Vincent, M., Whitlock, S., and Weidemüller, M. (2013a). *An experimental approach for investigating many-body phenomena in Rydberg-interacting quantum systems.* Frontiers of Physics.

[Hofmann *et al.*, 2013b] Hofmann, C. S., Günter, G., Schempp, H., Robert-de-Saint-Vincent, M., Gärttner, M., Evers, J., Whitlock, S., and Weidemüller, M. (2013b). *Sub-Poissonian Statistics of Rydberg-Interacting Dark-State Polaritons.* Phys. Rev. Lett. **110**, 203601.

[Hogan *et al.*, 2012] Hogan, S., Agner, J., Merkt, F., Thiele, T., Filipp, S., and Wallraff, A. (2012). *Driving Rydberg-Rydberg transitions from a coplanar microwave waveguide.* Phys. Rev. Lett. **108**, 063004.

[Höltkemeier, 2011] Höltkemeier, B. (2011). *2D-MOT as a source of a cold atom target.* Diploma thesis, Universität Heidelberg.

[Honer *et al.*, 2011] Honer, J., Löw, R., Weimer, H., Pfau, T., and Büchler, H. P. (2011). *Artificial Atoms Can Do More Than Atoms: Deterministic Single Photon Subtraction from Arbitrary Light Fields.* Phys. Rev. Lett. **107**, 093601.

[Höning *et al.*, 2013] Höning, M., Muth, D., Petrosyan, D., and Fleischhauer, M. (2013). *Steady-state crystallization of Rydberg excitations in an optically driven lattice gas.* Phys. Rev. A **87**, 023401.

[Isenhower *et al.*, 2010] Isenhower, L., Urban, E., Zhang, X. L., Gill, A. T., Henage, T., Johnson, T. A., Walker, T. G., and Saffman, M. (2010). *Demonstration of a Neutral Atom Controlled-NOT Quantum Gate.* Phys. Rev. Lett. **104**, 010503.

[Ishizaki and Fleming, 2009] Ishizaki, A. and Fleming, G. R. (2009). *Theoretical examination of quantum coherence in a photosynthetic system at physiological temperature*. Proceedings of the National Academy of Sciences **106**, 17255.

[Jaksch *et al.*, 2000] Jaksch, D., Cirac, J. I., Zoller, P., Rolston, S. L., Côté, R., and Lukin, M. D. (2000). *Fast Quantum Gates for Neutral Atoms*. Phys. Rev. Lett. **85**, 2208.

[Killian, 2007] Killian, T. C. (2007). *Ultracold Neutral Plasmas*. Science **316**, 705.

[Lan and Jorgenson, 2001] Lan, K. and Jorgenson, J. (2001). *A hybrid of exponential and gaussian functions as a simple model of asymmetric chromatographic peaks*. Journal of Chromatography A **915**, 1.

[Lee *et al.*, 2007] Lee, H., Cheng, Y.-C., and Fleming, G. R. (2007). *Coherence dynamics in photosynthesis: protein protection of excitonic coherence*. Science **316**, 1462.

[Lee *et al.*, 2011] Lee, T. E., Häffner, H., and Cross, M. C. (2011). *Antiferromagnetic phase transition in a nonequilibrium lattice of Rydberg atoms*. Phys. Rev. A **84**, 031402.

[Lee *et al.*, 2012] Lee, T. E., Häffner, H., and Cross, M. C. (2012). *Collective Quantum Jumps of Rydberg Atoms*. Phys. Rev. Lett. **108**, 023602.

[Lesanovsky and Garrahan, 2014] Lesanovsky, I. and Garrahan, J. P. (2014). *Out-of-equilibrium structures in strongly interacting Rydberg gases with dissipation*. arXiv preprint arXiv:1402.2126.

[Li *et al.*, 2003] Li, W., Mourachko, I., Noel, M. W., and Gallagher, T. F. (2003). *Millimeter-wave spectroscopy of cold Rb Rydberg atoms in a magneto-optical trap: Quantum defects of the ns, np, and nd series*. Phys. Rev. A **67**, 052502.

[Lochead *et al.*, 2013] Lochead, G., Boddy, D., Sadler, D. P., Adams, C. S., and Jones, M. P. A. (2013). *Number-resolved imaging of excited-state atoms using a scanning autoionization microscope*. Phys. Rev. A **87**, 053409.

[Löw *et al.*, 2012] Löw, R., Weimer, H., Nipper, J., Balewski, J. B., Butscher, B., Büchler, H. P., and Pfau, T. (2012). *An experimental and theoretical guide to strongly interacting Rydberg gases*. J. Phys. B **45**, 113001.

[Lukin *et al.*, 2001] Lukin, M. D., Fleischhauer, M., Cote, R., Duan, L. M., Jaksch, D., Cirac, J. I., and Zoller, P. (2001). *Dipole Blockade and Quantum Information Processing in Mesoscopic Atomic Ensembles.* Phys. Rev. Lett. **87**, 037901.

[Malossi *et al.*, 2013] Malossi, N., Valado, M., Scotto, S., Huillery, P., Pillet, P., Ciampini, D., Arimondo, E., and Morsch, O. (2013). *Full counting statistics and phase diagram of a dissipative Rydberg gas.* arXiv preprint arXiv:1308.1854.

[Maxwell *et al.*, 2013] Maxwell, D., Szwer, D. J., Paredes-Barato, D., Busche, H., Pritchard, J. D., Gauguet, A., Weatherill, K. J., Jones, M. P. A., and Adams, C. S. (2013). *Storage and Control of Optical Photons Using Rydberg Polaritons.* Phys. Rev. Lett. **110**, 103001.

[McQuillen *et al.*, 2013] McQuillen, P., Zhang, X., Strickler, T., Dunning, F. B., and Killian, T. C. (2013). *Imaging the evolution of an ultracold strontium Rydberg gas.* Phys. Rev. A **87**, 013407.

[Mohapatra *et al.*, 2007] Mohapatra, A. K., Jackson, T. R., and Adams, C. S. (2007). *Coherent Optical Detection of Highly Excited Rydberg States Using Electromagnetically Induced Transparency.* Physical Review Letters **98**, 113003.

[Møller *et al.*, 2008] Møller, D., Madsen, L. B., and Mølmer, K. (2008). *Quantum Gates and Multiparticle Entanglement by Rydberg Excitation Blockade and Adiabatic Passage.* Phys. Rev. Lett. **100**, 170504.

[Mølmer *et al.*, 1993] Mølmer, K., Castin, Y., and Dalibard, J. (1993). *Monte Carlo wave-function method in quantum optics.* J. Opt. Soc. Am. B **10**.

[Mourachko *et al.*, 1998] Mourachko, I., Comparat, D., de Tomasi, F., Fioretti, A., Nosbaum, P., Akulin, V. M., and Pillet, P. (1998). *Many-Body Effects in a Frozen Rydberg Gas.* Phys. Rev. Lett. **80**, 253.

[Mülken *et al.*, 2007] Mülken, O., Blumen, A., Amthor, T., Giese, C., Reetz-Lamour, M., and Weidemüller, M. (2007). *Survival Probabilities in Coherent Exciton Transfer with Trapping.* Phys. Rev. Lett. **99**, 090601.

[Müller, 2010] Müller, N. L. M. (2010). *Excitation and Detection of Rydberg atoms in an Ultracold Gas.* Diploma thesis, Universiät Heidelberg.

[Nazarov and Blanter, 2009] Nazarov, Y. and Blanter, Y. (2009). *Quantum Transport: Introduction to Nanoscience.* Cambridge University Press.

[Ni *et al.*, 2008] Ni, K.-K., Ospelkaus, S., De Miranda, M., Pe'er, A., Neyenhuis, B., Zirbel, J., Kotochigova, S., Julienne, P., Jin, D., and Ye, J. (2008). *A high phase-space-density gas of polar molecules.* Science **322**, 231.

[Olmos *et al.*, 2011] Olmos, B., Li, W., Hofferberth, S., and Lesanovsky, I. (2011). *Amplifying single impurities immersed in a gas of ultracold atoms.* Phys. Rev. A **84**, 041607.

[O'Sullivan and Stoicheff, 1985] O'Sullivan, M. S. and Stoicheff, B. P. (1985). *Scalar polarizabilities and avoided crossings of high Rydberg states in Rb.* Phys. Rev. A **31**, 2718.

[Otterbach *et al.*, 2013] Otterbach, J., Moos, M., Muth, D., and Fleischhauer, M. (2013). *Wigner Crystallization of Single Photons in Cold Rydberg Ensembles.* Phys. Rev. Lett. **111**, 113001.

[Overstreet *et al.*, 2009] Overstreet, K. R., Schwettmann, A., Tallant, J., Booth, D., and Shaffer, J. P. (2009). *Observation of electric-field-induced Cs Rydberg atom macrodimers.* Nature Physics **5**, 581.

[Paredes-Barato and Adams, 2014] Paredes-Barato, D. and Adams, C. S. (2014). *All-Optical Quantum Information Processing Using Rydberg Gates.* Phys. Rev. Lett. **112**, 040501.

[Park *et al.*, 2011] Park, H., Tanner, P. J., Claessens, B. J., Shuman, E. S., and Gallagher, T. F. (2011). *Dipole-dipole broadening of Rb ns – np microwave transitions.* Phys. Rev. A **84**, 022704.

[Petrosyan *et al.*, 2013] Petrosyan, D., Höning, M., and Fleischhauer, M. (2013). *Spatial correlations of Rydberg excitations in optically driven atomic ensembles.* Phys. Rev. A **87**, 053414.

[Peyronel *et al.*, 2012] Peyronel, T., Firstenberg, O., Liang, Q.-Y., Hofferberth, S., Gorshkov, A. V., Pohl, T., Lukin, M. D., and Vuletić, V. (2012). *Quantum nonlinear optics with single photons enabled by strongly interacting atoms.* Nature **488**, 57.

[Phillips *et al.*, 2001] Phillips, D. F., Fleischhauer, A., Mair, A., Walsworth, R. L., and Lukin, M. D. (2001). *Storage of Light in Atomic Vapor.* Phys. Rev. Lett. **86**, 783.

[Plenio and Huelga, 2008] Plenio, M. B. and Huelga, S. F. (2008). *Dephasing-assisted transport: quantum networks and biomolecules.* New Journal of Physics **10**, 113019.

[Pohl *et al.*, 2010] Pohl, T., Demler, E., and Lukin, M. D. (2010). *Dynamical Crystallization in the Dipole Blockade of Ultracold Atoms.* Phys. Rev. Lett. **104**, 043002.

[Pritchard, 2011] Pritchard, J. D. (2011). *Cooperative Optical Non-linearity in a blockaded Rydberg Ensemble.* PhD thesis Durham.

[Pritchard *et al.*, 2012a] Pritchard, J. D., Adams, C. S., and Mølmer, K. (2012a). *Correlated Photon Emission from Multiatom Rydberg Dark States.* Phys. Rev. Lett. **108**, 043601.

[Pritchard *et al.*, 2010] Pritchard, J. D., Maxwell, D., Gauguet, A., Weatherill, K. J., Jones, M. P. A., and Adams, C. S. (2010). *Cooperative Atom-Light Interaction in a Blockaded Rydberg Ensemble.* Phys. Rev. Lett. **105**, 193603.

[Pritchard *et al.*, 2012b] Pritchard, J. D., Weatherill, K. J., and Adams, C. S. (2012b). *Nonlinear optics using cold Rydberg atoms.* Annual Review of Cold Atoms and Molecules **1**, 301.

[Rebentrost *et al.*, 2009a] Rebentrost, P., Chakraborty, R., and Aspuru-Guzik, A. (2009a). *Non-Markovian quantum jumps in excitonic energy transfer.* The Journal of Chemical Physics **131**, 184102.

[Rebentrost *et al.*, 2009b] Rebentrost, P., Mohseni, M., Kassal, I., Lloyd, S., and Aspuru-Guzik, A. (2009b). *Environment-assisted quantum transport.* New Journal of Physics **11**, 033003.

[Reinhard *et al.*, 2008a] Reinhard, A., Younge, K. C., Liebisch, T. C., Knuffman, B., Berman, P. R., and Raithel, G. (2008a). *Double-Resonance Spectroscopy of Interacting Rydberg-Atom Systems.* Physical Review Letters **100**, 233201.

[Reinhard *et al.*, 2008b] Reinhard, A., Younge, K. C., and Raithel, G. (2008b). *Effect of Förster resonances on the excitation statistics of many-body Rydberg systems.* Phys. Rev. A **78**, 060702.

[Reiter and Sørensen, 2012] Reiter, F. and Sørensen, A. S. (2012). *Effective operator formalism for open quantum systems.* Phys. Rev. A **85**, 032111.

[Robert-de-Saint-Vincent *et al.*, 2013] Robert-de-Saint-Vincent, M., Hofmann, C. S., Schempp, H., Günter, G., Whitlock, S., and Weidemüller, M. (2013). *Spontaneous Avalanche Ionization of a Strongly Blockaded Rydberg Gas.* Phys. Rev. Lett. **110**, 045004.

[Robicheaux and Gill, 2014] Robicheaux, F. and Gill, N. (2014). *The effect of random positions for dipole hopping through a Rydberg gas.* arXiv preprint arXiv:1401.4776.

[Saffman *et al.*, 2010] Saffman, M., Walker, T. G., and Mølmer, K. (2010). *Quantum information with Rydberg atoms.* Rev. Mod. Phys. **82**, 2313.

[Sarovar *et al.*, 2010] Sarovar, M., Ishizaki, A., Fleming, G. R., and Whaley, K. B. (2010). *Quantum entanglement in photosynthetic light-harvesting complexes.* Nature Physics **6**, 462.

[Schauß *et al.*, 2012] Schauß, P., Cheneau, M., Endres, M., Fukuhara, T., Hild, S., Omran, A., Pohl, T., Gross, C., Kuhr, S., and Bloch, I. (2012). *Observation of spatially ordered structures in a two-dimensional Rydberg gas.* Nature **491**, 87.

[Schauß *et al.*, 2014] Schauß, P., Zeiher, J., Fukuhara, T., Hild, S., Cheneau, M., Macrì, T., Pohl, T., Bloch, I., and Gross, C. (2014). *Dynamical crystallization in a low-dimensional Rydberg gas.* arXiv preprint arXiv:1404.0980.

[Schempp *et al.*, 2010] Schempp, H., Günter, G., Hofmann, C. S., Giese, C., Saliba, S. D., DePaola, B. D., Amthor, T., Weidemüller, M., Sevinçli, S., and Pohl, T. (2010). *Coherent Population Trapping with Controlled Interparticle Interactions.* Phys. Rev. Lett. **104**, 173602.

[Schempp *et al.*, 2014] Schempp, H., Günter, G., Robert-de Saint-Vincent, M., Hofmann, C. S., Breyel, D., Komnik, A., Schönleber, D. W., Gärttner, M., Evers, J., Whitlock, S., and Weidemüller, M. (2014). *Full Counting Statistics of Laser Excited Rydberg Aggregates in a One-Dimensional Geometry.* Phys. Rev. Lett. **112**, 013002.

[Schnorrberger *et al.*, 2009] Schnorrberger, U., Thompson, J. D., Trotzky, S., Pugatch, R., Davidson, N., Kuhr, S., and Bloch, I. (2009). *Electromagnetically Induced Transparency and Light Storage in an Atomic Mott Insulator.* Phys. Rev. Lett. **103**, 033003.

[Schönleber *et al.*, 2014] Schönleber, D. W., Gärttner, M., and Evers, J. (2014). *Coherent versus incoherent excitation dynamics in dissipative many-body Rydberg systems.* arXiv **1401.7260**.

[Schwarzkopf *et al.*, 2013] Schwarzkopf, A., Anderson, D. A., Thaicharoen, N., and Raithel, G. (2013). *Spatial correlations between Rydberg atoms in an optical dipole trap.* Phys. Rev. A **88**, 061406.

[Schwarzkopf *et al.*, 2011] Schwarzkopf, A., Sapiro, R. E., and Raithel, G. (2011). *Imaging Spatial Correlations of Rydberg Excitations in Cold Atom Clouds.* Phys. Rev. Lett. **107**, 103001.

[Scully and Zubairy, 1997] Scully, M. O. and Zubairy, M. S. (1997). *Quantum optics.* Cambridge University Press.

[Sevinçli *et al.*, 2011a] Sevinçli, S., Ates, C., Pohl, T., Schempp, H., Hofmann, C. S., Günter, G., Amthor, T., Weidemüller, M., Pritchard, J. D., Maxwell, D., Gauguet, A., Weatherill, K. J., Jones, M. P. A., and Adams, C. S. (2011a). *Quantum interference in interacting three-level Rydberg gases: coherent population trapping and electromagnetically induced transparency.* J. Phys. B **44**, 184018.

[Sevinçli *et al.*, 2011b] Sevinçli, S., Henkel, N., Ates, C., and Pohl, T. (2011b). *Nonlocal Nonlinear Optics in Cold Rydberg Gases.* Phys. Rev. Lett. **107**, 153001.

[Singer *et al.*, 2004] Singer, K., Reetz-Lamour, M., Amthor, T., Marcassa, L. G., and Weidemüller, M. (2004). *Suppression of Excitation and Spectral Broadening Induced by Interactions in a Cold Gas of Rydberg Atoms.* Phys. Rev. Lett. **93**, 163001.

[Singer *et al.*, 2005] Singer, K., Stanojevic, J., Weidemüller, M., and Côté, R. (2005). *Long-range interactions between alkali Rydberg atom pairs correlated to the ns-ns, np-np and nd-nd asymptotes.* J. Phys. B **38**, S295.

[Steck, 2001] Steck, D. A. (2001). *Rubidium 87 D line data.* available online http://steck.us/alkalidata.

[Tauschinsky *et al.*, 2010] Tauschinsky, A., Thijssen, R. M. T., Whitlock, S., van Linden van den Heuvell, H. B., and Spreeuw, R. J. C. (2010). *Spatially resolved excitation of Rydberg atoms and surface effects on an atom chip.* Phys. Rev. A **81**, 063411.

[Thorwart *et al.*, 2009] Thorwart, M., Eckel, J., Reina, J. H., Nalbach, P., and Weiss, S. (2009). *Enhanced quantum entanglement in the non-Markovian dynamics of biomolecular excitons.* Chemical Physics Letters **478**, 234.

[Tiarks *et al.*, 2014] Tiarks, D., Baur, S., Schneider, K., Dürr, S., and Rempe, G. (2014). *Single-Photon Transistor Using a Förster-Resonance.* arXiv preprint arXiv:1404.3061.

[Tong *et al.*, 2004] Tong, D., Farooqi, S. M., Stanojevic, J., Krishnan, S., Zhang, Y. P., Côté, R., Eyler, E. E., and Gould, P. L. (2004). *Local Blockade of Rydberg Excitation in an Ultracold Gas.* Phys. Rev. Lett. **93**, 063001.

[Urban *et al.*, 2009] Urban, E., Johnson, T., Henage, T., Isenhower, L., Yavuz, D., Walker, T., and Saffman, M. (2009). *Observation of Rydberg blockade between two atoms.* Nature Physics **5**, 110.

[van Ditzhuijzen *et al.*, 2008] van Ditzhuijzen, C. S. E., Koenderink, A. F., Hernández, J. V., Robicheaux, F., Noordam, L. D., and van den Heuvell, H. B. v. L. (2008). *Spatially Resolved Observation of Dipole-Dipole Interaction between Rydberg Atoms.* Phys. Rev. Lett. **100**, 243201.

[Viteau *et al.*, 2011] Viteau, M., Bason, M. G., Radogostowicz, J., Malossi, N., Ciampini, D., Morsch, O., and Arimondo, E. (2011). *Rydberg Excitations in Bose-Einstein Condensates in Quasi-One-Dimensional Potentials and Optical Lattices.* Phys. Rev. Lett. **107**, 060402.

[Viteau *et al.*, 2012] Viteau, M., Huillery, P., Bason, M. G., Malossi, N., Ciampini, D., Morsch, O., Arimondo, E., Comparat, D., and Pillet, P. (2012). *Cooperative Excitation and Many-Body Interactions in a Cold Rydberg Gas.* Phys. Rev. Lett. **109**, 053002.

[Vogt *et al.*, 2006] Vogt, T., Viteau, M., Zhao, J., Chotia, A., Comparat, D., and Pillet, P. (2006). *Dipole blockade at Förster resonances in high resolution laser excitation of Rydberg states of cesium atoms.* Physical review letters **97**, 083003.

[Walker and Saffman, 2008] Walker, T. G. and Saffman, M. (2008). *Consequences of Zeeman degeneracy for the van der Waals blockade between Rydberg atoms.* Physical Review A **77**, 032723.

[Weimer, 2014] Weimer, H. (2014). private communication.

[Weimer *et al.*, 2008] Weimer, H., Löw, R., Pfau, T., and Büchler, H. P. (2008). *Quantum Critical Behavior in Strongly Interacting Rydberg Gases.* Phys. Rev. Lett. **101**, 250601.

[Weise, 2009] Weise, T. (2009). *Global Optimization Algorithms, Theory and Application.* http://it-weise.de. 2nd Edition.

[Westermann *et al.*, 2006] Westermann, S., Amthor, T., de Oliveira, A. L., Deiglmayr, J., Reetz-Lamour, M., and Weidemüller, M. (2006). *Dynamics of resonant energy transfer in a cold Rydberg gas.* The European Physical Journal D - Atomic, Molecular, Optical and Plasma Physics **40**, 37.

[Wilk *et al.*, 2010] Wilk, T., Gaëtan, A., Evellin, C., Wolters, J., Miroshnychenko, Y., Grangier, P., and Browaeys, A. (2010). *Entanglement of Two Individual Neutral Atoms Using Rydberg Blockade.* Phys. Rev. Lett. **104**, 010502.

[Williams, 2007] Williams, J. G. (2007). *Organic Light-Emitting Devices: Synthesis, Properties and Applications.* Platinum Metals Review **51**, 85.

[Zimboras *et al.*, 2013] Zimboras, Z., Faccin, M., Kadar, Z., Whitfield, J., Lanyon, B., and Biamonte, J. (2013). *Quantum Transport Enhancement by Time-Reversal Symmetry Breaking.* Scientific Reports **3**, 2361.

Danksagung

Diese Arbeit wäre nicht möglich gewesen ohne die Hilfe und Unterstützung vieler Menschen, denen ich an dieser Stelle herzlich dafür danken möchte.
Zunächst möchte ich mich herzlich bei meinem Betreuer **Matthias Weidemüller** für sein Vertrauen und seine Großzügigkeit bedanken. Die Zeit in deiner Arbeitsgruppe war für mich sehr wertvoll. Durch die vielen Freiheiten in der Gestaltung der Arbeit habe ich viel gelernt, ebenso aber natürlich in unseren zahlreichen Diskussionen.
Selim Jochim danke ich für die Übernahme der Zweitkorrektur dieser Arbeit und für fruchtbaren Austausch auch mit den Mitgliedern seiner Arbeitsgruppe.
I very much appreciate to have worked with **Shannon Whitlock**, who is at the same time an exceptionally gifted teacher and a fantastic colleague. Your never ending ideas, your insistence when it comes to problem solving and your skills to repair T****** lasers with a hammer are really impressive and I am gratefull to have learned some of these things from you. And I am looking forward to some more midfield battles at the kicker table.
Martin Robert-de-Saint-Vincent, thanks for your happy mood, your optimism, your back-of-an-envelop-calculations, your physical insights. It was a great pleasure to work with you!
Georg Günter danke ich für die ausgezeichnete Zusammenarbeit im Labor und unzählige Theoriediskussionen, bei denen der Knoten im Hirn zwar nicht immer, aber doch in den meisten Fällen aufgelöst werden konnte. Für die sehr schöne Zeit, nicht nur im Oldie-Büro, und das Gießen der Pflanzen möchte ich dir ebenfalls herzlich danken. Insbesondere aber auch für die Projekte Bach, Beethoven und Brahms, die mir unheimlich viel Freude bereitet haben.
Christoph Hofmann danke ich für die sorgfältige Planung des besten Experiments der Welt! Ob Beschischtung, Sackgewinde oder M14, mit dir waren selbst eher trockene Themen ein Vergnügen. Danke auch für die gemeinsame Vorliebe für Balkan Beats und die Farbe lila. Deine Fröhlichkeit und dein lokaler Zungenschlag waren

immer eine große Bereicherung.
Bei **Thomas Amthor** möchte ich mich für die durchweg angenehme Zusammenarbeit und die wertvolle Unterstützung im ersten Jahr bedanken, insbesondere beim Verdauen der CPT-Experimente.
Thanks to the new PhD students **Vladislav Gavryusev** and **Miguel Ferreira Cao** for their support in the lab. I wish you good luck with the experiment!
Eine ganze Reihe von Diplom-, Master- und Bachelorstudenten haben unser Experiment in den letzten Jahren bereichert. **Nele Müller** danke ich für die tolle Zusammenarbeit am Detektor und die schöne Anfangszeit. Herzlichen Dank an **Hannes Busche** für die 2D-MOT, **Aline Faber** für die Dipolfalle, **Henning Labuhn** für die Cavity und **Max Argus** fürs Optimieren. **Stephan Helmrich** schließlich danke ich für das Auflösungsvermögen und das unfall- und ruckfreie Bewegen enormer Metallplatten.
Thanks to **Maria Martinez Valado** and **Giulia Faraoni** for joining us and contributing to the experiment!
Den anderen Mitgliedern der Arbeitsgruppe, nämlich den Mixtures um **Marc Repp, Rico Pires, Juris Ulmanis** und **Eva Kuhnle** sowie den Motrims um **Bastian Höltkemeier** gilt meine großer Dank für die tolle Zusammenarbeit und angenehme Atmosphäre.
Sehr wertvoll waren unsere regelmäßigen und ergiebigen Diskussionen mit **Martin Gärttner, Kilian Heeg, David Schönleber** und **Jörg Evers** sowie **David Breyel** und **Andreas Komnik**. Ebenfalls für erhellende Diskussionen möchte ich mich bei **Hendrik Weimer, Igor Lesanovsky, Thomas Pohl** und **Rick van Bijnen** bedanken.
Diese Arbeit wäre nicht möglich gewesen ohne die Mitarbeiter der Mechanischen Werkstatt und Elektronikwerkstatt. Hier gilt mein besonderer Dank **Herrn Ziegler, Dominic Litsch, Simon Rabenecker, Jessica Riedinger und Jürgen Gerhäuser**. Ich möchte mich außerdem bei der Kohlmeise bedanken, dass sie nicht durch den Dipolfallenstrahl geflogen ist, und gleichzeitig meine Betroffenheit darüber ausdrücken, dass sie dennoch den Januar 2013 im Philosophenweg 12 nicht überlebt hat.
Meiner Familie möchte ich für ihre große Unterstützung danken. **Henning**, du bist das allerwichtigste für mich, und deine Unterstützung und dein Verständis waren unverzichtbar. Ich freue mich riesig auf alles weitere!